

Modelling cancer mechanics across multiple length scales: from basic understanding to applications

Submitted in partial fulfillment of the requirements
of the degree of

Doctor of Philosophy

by

Abhishek Mukherjee

Supervisors:

**IIT Bombay: Prof. Shamik Sen, Prof. Ramesh Singh and Prof. Abhishek
Gupta**

Monash University: Prof. Wenyi Yan



*The course of study for this award was developed jointly by
Monash University, Australia and the Indian Institute of Technology Bombay, India
and was given academic recognition by each of them.
The programme was administrated by The IITB-Monash Research Academy*

Dedicated to my parents, for their unconditional love and support.

Declaration

I declare that this written submission represents my ideas in my own words and where others ideas or words have been included, I have adequately cited and referenced the original sources. I also declare that I have adhered to all principles of academic honesty and integrity and have not misrepresented or fabricated or falsified any idea/data/fact/source in my submission. I understand that any violation of the above will be cause for disciplinary action by the Institute and can also evoke penal action from the sources which have thus not been properly cited or from whom proper permission has not been taken when needed.

Date: 23 November 2020

Abhishek Mukherjee

Acknowledgments

I am extremely grateful to my supervisors Prof. Shamik Sen, Prof. Wenyi Yan, Prof. Ramesh Singh and Prof. Abhishek Gupta for giving me the opportunity to work on the projects that constitute this thesis. Although the projects were completely new to me, their constant encouragement, support and attention to academic rigour helped me gain the required technical expertise and address those. Over the course of the past five years, I feel I have evolved not only as a researcher, but also as a person under their guidance.

I shall remain indebted to Prof. Sen for being a mentor and guide to me and for supporting me during the toughest times of my PhD. His faith in me was invaluable and I cannot thank him enough. I thank him also for introducing me to the fascinating world of biophysics and mechanobiology. Discussion sessions with him on various topics have always been enriching experiences for me. I am grateful for Prof. Yan's support throughout my PhD and especially during my one-year stay in Monash University. Discussions with him were crucial in getting the cell migration model in this study to work. I am thankful to Prof. Singh and Prof. Gupta for being patient with me during the early years of my PhD. Discussions with them were always thought provoking and they moulded my approach towards meticulously solving a scientific problem. I am grateful to all my supervisors for always providing all possible resources and support required to effectively pursue this field of research and for my own self-improvement. I also wish to thank my research progress committee members Prof. Mandar Inamdar and Prof. Jing Fu for their helpful comments and suggestions regarding my research work.

My heartfelt thanks go to the IITB-Monash Research Academy for helping me gain valuable international and multicultural exposure. I believe this has had a great impact on my research and made me a better person. I would like to thank all the staff, especially Jayasree Ma'am, Laya Ma'am and Murali Sir as they were our pillars of support and were always ready to help us with anything we required. I thank them also for smoothening the various administrative procedures and paperwork which are usually a headache for students. I would like to thank the staff at the Dept. of Mechanical Engineering at IIT Bombay and the Mechanical and

Aerospace Engineering at Monash University for their help with paperwork and resources.

The journey towards a PhD is usually very tough and tends to be a bit lonely sometimes. Friends and colleagues help relieve the stress and loneliness with discussions over several cups of tea. I have been fortunate enough to have made some great friends over the course of my PhD, especially my batchmates Dr. Supriya Patibanda, Bhavesh Kamaliya, Dr. Laxman Malla, Dr. Vivek Garg and Sagar Agnihotri. They have always readily extended their help and support. I thank Siddharth Gupta for his friendship. I enjoyed the camaraderie and our trips together. I thank everybody in the Machine Tools Lab for their help, especially Chaitanya Vundru, Dr. Nilanjan Banerjee, Dr. Meinam Annebushan Singh and Vishnu Narayanan. I learnt a lot from them through numerous technical and non-technical discussions over massive amounts of tea and shared lunches over the years. I would also like to thank everybody in the Cellular Biophysics Lab for always being friendly and helpful, especially Amlan Barai who patiently explained several biological concepts over breakfast and dinner and performed the experiments used to validate our simulation results. I thank everybody in Prof. Yan's lab at Monash University for their friendship. They made my stay in Melbourne pleasant and enjoyable. I thank my childhood friends Sourav Mukherjee and Maj. Dr. Indranuj Roy for our bond of friendship that I always cherish.

I would like to extend my sincere gratitude to all my teachers over the years who have influenced me and made me into who I am. My deepest respect and gratitude are reserved for my parents for their numerous sacrifices, constant encouragement, love and support. I would not have had the courage to pursue and stick to my PhD had it not been for their encouragement. I dedicate this thesis to them. Finally, I would like to thank my best friend and spouse Moumita for her extreme patience and understanding even when I was unreasonable. This PhD journey has been possible because of her love and support.

Abstract

Large nuclear deformations during cell migration through confined spaces have been associated with nuclear membrane rupture and DNA damage. However, the associated stresses remain unclear. Here, using a quasi-static plane strain finite element model, we map evolution of nuclear shape and stresses during confined migration of a cell through a deformable matrix. Plastic deformation of the nucleus observed for a cell with stiff nucleus transiting through a stiffer matrix lowered nuclear stresses, but also led to kinking of the nuclear membrane, indicating the region of possible nuclear membrane rupture. In line with model predictions, transwell migration experiments with fibrosarcoma cells showed that while nuclear softening increased invasiveness, nuclear stiffening led to plastic deformation and higher levels of DNA damage. In addition to highlighting the advantage of nuclear softening during confined migration, our results suggest that plastic deformations of the nucleus during transit through stiff tissues may lead to bending-induced nuclear membrane disruption and subsequent DNA damage.

We then incorporated a glycocalyx assumed to be attached to the cell membrane as a continuum and modelled it as a Neo-Hookean hyperelastic material. Glycocalyx polymer chains collectively act as a polymer brush under external stresses. The glycopolymer thickness and density has been shown to strongly correlate with the metastatic potential of a cancer cell, pointing to the glycocalyx mechanically facilitating confined cell migration. Indeed, our results recorded in this thesis demonstrate that upon indentation, a thick glycocalyx acts as a shock absorber or cushion under large strains primarily by increasing the surface area of external force application. Cell spreading was also found to impact the mechanics of cellular glycocalyx apart from its thickness and density.

We then developed a tissue level model for efficient detection of tumor nodule embedded in healthy tissue. A physician palpates a tissue to detect an embedded nodule and to estimate its mechanical properties relative to the surrounding tissue based on the estimation of contact forces and apparent tissue stiffness. Utilizing a hyperelastic material model, we propose a general methodology to analyze the extent to which the stiffness, size and depth of a nodule embedded

in a tissue affect its detectability. Using dimensional analysis, we generate simple power-law relations to predict physical and material properties of tumor nodules embedded in healthy tissue during indentation. Our results indicate that indenter radius and indentation depth are critical parameters in nodule detection and a thin indenter and large indentation depth increase detection sensitivity of an embedded tumor nodule. Our results also show that anisotropic material properties of either a tissue or an embedded nodule render the embedded tumor nodule undetectable using indentation. We define palpation sensitivity maps that can be used to predict material and physical properties of tumor nodules in healthy tissues.

Contents

Abstract	i
List of Tables	ix
List of Figures	xi
List of Abbreviations	xxiii
List of Symbols	xxv
1 Introduction	1
1.1 Introduction to Cancer	1
1.2 The Extracellular Matrix (ECM) in Cancer	2
1.2.1 The ECM as a Mechanical Barrier to Invasion	3
1.2.2 Rheology of soft materials	4
1.2.3 Modeling the rheology of cells and tissues	6
1.3 Cancer Metastasis	8
1.4 Mechanisms of Invasion	10
1.4.1 Modes of cell migration	11
1.5 Nucleus as a Rate-Limiting Factor in Cell Migration	13

1.5.1	Biological Implications of Nuclear Rupture	15
1.6	The Cellular Glycocalyx	16
1.6.1	Formation of Glycocalyx	17
1.6.2	Glycocalyx in Cancer	18
1.7	Motivation	19
1.8	Hypothesis	19
1.9	Research Objectives	20
1.10	Thesis Outline	21
2	Modelling of confined cell migration	23
2.1	Introduction	23
2.2	Viscoelasticity of cell and extracellular matrix (ECM)	25
2.2.1	Viscoelasticity formulation in the time-domain	25
2.3	Plasticity of the nucleus	27
2.4	Cytoskeletal strain stiffening	27
2.5	Methods	28
2.5.1	Computational Methods	28
2.5.2	Experimental Methods	35
2.6	Results	36
2.6.1	Nuclear and tissue properties collectively dictate dynamics of confined migration	36

2.6.2	Degree of confinement and nuclear/tissue properties collectively dictate average cell speed	40
2.6.3	Plastic deformation of the nucleus and kink formation during pore entry	41
2.6.4	Nuclear plasticity and DNA damage: insights from experiments	48
2.6.5	Scaling relationships	54
2.7	Discussion	55
2.8	Conclusion	60
3	Mechanical modelling of the cellular glycocalyx	61
3.1	Introduction	61
3.2	Materials and Methods	62
3.2.1	Methodology	62
3.2.2	Physical description of the modelling problem	67
3.2.3	Finite Element Model	69
3.3	Results	72
3.3.1	Magnitude and localization of maximum stresses change in cell body and glycocalyx with increasing glycocalyx thickness during spherical indentation	72
3.3.2	Evolution of indentation loads during spherical indentation of cellular glycocalyx	72
3.3.3	Compression of cellular glycocalyx against ECM	73

3.3.4	ECM displacement due to compression of cellular glycocalyx against ECM	76
3.3.5	Mechanical implications of glycocalyx as a double brush	79
3.4	Discussion	80
3.5	Conclusion	82
4	Detection of tumor nodule embedded inside healthy tissue	83
4.1	Introduction	83
4.2	Materials and Methods	85
4.2.1	Physical description of the modelling problem	87
4.2.2	Numerical formulation	87
4.2.3	Loading and boundary conditions	88
4.2.4	Material model	89
4.2.5	Model validation	93
4.2.6	Dimensional analysis	94
4.3	Results and discussion	95
4.3.1	Detection of composite stiffness of tissue and nodule using Hertzian and finite element approach	96
4.3.2	Effect of non-dimensional parameters on indentation load	98
4.3.3	Effect of anisotropy on nodule detection	103
4.4	Palpation sensitivity chart	106

4.5	Conclusion	109
5	Summary and Conclusions	111
5.1	Contributions	113
5.2	Scope for future research	114
	List of Publications	115
	References	117

List of Tables

2.1	Comparison with other FE-based cell migration models	30
2.2	Material parameters	33
3.1	Material parameters	67
3.2	Stiffness dependence of Glycocalyx on L and N	68
4.1	Material parameters used in the model	92
4.2	Difference between FE solution and Hertz solution for homogeneous tissue of $G_0 = 1$ kPa for varied tissue thickness	97
4.3	Difference between FE solution and Hayes' solution for homogeneous tissue of $G_0 = 1$ kPa for varied tissue thickness	97

List of Figures

1.1	Growth of a tumor over time. (A) Tumor growth in breast cancer. (B) Tumor growth in colon cancer.	2
1.2	Intracellular components of a representative cell. (a) A typical cell with organelles. (b) Essential filamentous constituents of a typical cell. Created with BioRender.	5
1.3	Schematics of common viscoelastic models. (A) Maxwell model, (B) Voigt model, (C) Standard Linear Solid (SLS) model, and (D) Generalized Maxwell model. k and η denote spring stiffness and damper viscosity respectively.	8
1.4	Schematic of the process of cancer metastasis. Created with BioRender.	10
1.5	Schematics of 2D and 3D migration. (A) Process of protrusion and retraction of focal adhesions (FAs) required by a cell to migrate on 2D substrates. (B) 3D migration of a cell through confinement in a fibrous matrix with the help of focal adhesions (FAs) attached to matrix fibers. Created with BioRender.	12
1.6	Glycocalyx stiffness increases with increased polymer density. Polymer density in glycocalyx attached to cell body increases either with increased polymerization and attachment of glycopolymers to cell membrane or by increased polymerization and attachment of sidechains to existing polymer backbone.	17
2.1	Model definition. (A) Schematic of the simulated problem. (B) Finite element model with mesh. Lateral and transverse boundaries of the tissue (1 and 2) are constrained in their perpendicular directions. (C) Dimensions of various parts of the modelled cell (only 1/4th of the cell is shown due to symmetry).	31
2.2	Model process flow.	31

2.3	Material parameters used in the model. (A) Viscoelastic properties of various materials in the model. (B) Temporal variation of input force. (C) Assumed dependence of cytoplasmic stiffness (E_c) with shear stress (σ_{shear}) encountered by the cell. E_c is increased in discrete steps as indicated by datapoints and a smooth curve is interpolated, i.e., the points are used to define a function between the two variables.	32
2.4	Interplay of nuclear and tissue stiffness on dynamics of pore entry for migration through homogeneous tissue. (A) Cellular deformation just after entry into pore for different extents of degree of confinement (D_0/ϕ). E_c was increased from an initial value of 1 Pa to a possible maximum of 1.1 Pa under shear-induced cytoskeletal stiffening and E_n was assumed to be 1 kPa. (B) Force (F_{entry}) and time (T_{entry}) required for a cell (with $E_n = 1$ kPa) to enter a pore of given size and their dependence on tissue stiffness ($E_T = E_1 = E_2$) and D_0/ϕ	38
2.5	Interplay of nuclear and tissue stiffness on dynamics of pore entry for interfacial migration. (A) Nuclear deformation for the case of cell entry through an interface between two dissimilar tissues. Dependence of (B) T_{entry} , and (C) F_{entry} on E_1/E_2 for $D_0/\phi = 1.67$ and $E_n = 1$ kPa.	39
2.6	Deformation of ECM after nucleus entry into pore. (A) Contour plots of vertical tissue displacement (u_y) at the time of nucleus entry into the pore, i.e., when the entire nucleus has just completed entering the pore. (B) Spatial dependence of u_y along the tissue length at the time of pore entry for different values of E_T and E_n and $D_0/\phi = 1.67$. Pore entry occurs at normalized tissue length = 0.	39
2.7	Cell migration speed through confinement. (A) Instantaneous cell velocity (v_x) calculated from the start of the simulation ($t = 0$ s) till the instant of pore entry. $D_0/\phi = 1.67$ for these three cases.	41

2.8 **Morphological changes in cell/nucleus during confined migration.** (A) Shapes of the cell and the nucleus at the time of pore entry for different combinations of E_T and E_n and $D_0/\phi = 1.67$. $x_{CN}(t)$ represents the distance between the leading edge of the cell and the front edge of the nucleus at time t . $x_N(t)$ represents the distance between the nucleus center and its front edge at time t . Dotted lines depict breaks in the cell profiles. (B) Temporal evolution of cytoplasmic stretch ($x_{CN}(t)/x_{CN}(0)$) and nuclear stretch ($x_N(t)/x_N(0)$) along the direction of migration for $D_0/\phi = 1.67$. (C) Dependence of nuclear circularity (D/L) on E_n/E_T for $D_0/\phi = 1.67$ and different values of E_n 42

2.9 **Quantification of intracellular and intranuclear stresses during confined migration.** The spatiotemporal evolution of stress distribution before and after entry of a $5\mu\text{m}$ nucleus into a $3\mu\text{m}$ pore, i.e., $D_0/\phi = 1.67$. Contours and colourbars indicate von Mises stresses (σ_{Mises}) developed in the cytoplasm and nucleus. 44

2.10 Nuclear plasticity during confined migration. (A) Spatial map of plastic strain ($\epsilon_{plastic}$) accumulated in the nucleus just after pore entry. The total strain (ϵ_{total}) in a body is defined as the sum of elastic ($\epsilon_{elastic}$) and plastic strain, i.e., $\epsilon_{total} = \epsilon_{elastic} + \epsilon_{plastic}$. $\epsilon_{elastic}$ is defined as the reversible strain in the body whereas, $\epsilon_{plastic}$ is irreversible. We use a strain hardening material property definition given by: $\sigma = a + b\epsilon_{plastic}^n$, where σ is the applied stress, $\sigma_{yield} = a$, and a , b and n are material properties. (B) Spatial distribution of von Mises stress in the nucleus along the vertical direction just after nuclear entry ($D_0/\phi = 1.67$). (C) Temporal evolution of hoop stresses ($\sigma_{\theta\theta}$) in the nuclear membrane from the start of simulation to the instant the nucleus completely enters the pore. The two cylindrical components of stresses, namely, radial (σ_{rr}) and hoop ($\sigma_{\theta\theta}$) stress in the nuclear membrane are depicted along with the region of nuclear membrane from which the curves are extracted ($D_0/\phi = 1.67$). Green-Black and Red-Blue curves correspond to two different combinations of E_T and E_n as shown. Green and Red dots in the representative snapshot of the nuclear membrane correspond to kinked mesh elements on the nuclear membrane at its interface with the nucleus for $E_n = 0.2$ kPa and $E_n = 2$ kPa respectively. Similarly, Black and Blue dots correspond to kinked mesh elements on the nuclear membrane at its interface with the cytoplasm. 46

2.11 Plastic deformation of nuclei in cells migrating through an interface and spatiotemporal evolution of plastic deformation. (A) E_1 and E_2 refer to the Young's moduli of tissues 1 and 2 on both sides of the interface. $D_0/\phi = 1.67$ for all the cases. Contours represent the spatial distribution of plastic strain ($\epsilon_{plastic}$). (B) Plastic strain accumulated in a cell as a function of time during constricted migration for $D_0/\phi = 1.67$. $E_n = E_T = 2$ kPa. Red arrows indicate the region where necking first occurs and plasticity is initiated. The colourbar indicates magnitude of plastic strain in the nucleus ($\epsilon_{plastic} = \epsilon_{total} - \epsilon_{elastic}$). . . 47

2.12 Experiment setup and mechanical characterization of cells. (A) Phase contrast images of HT-1080 fibrosarcoma cells treated with vehicle (DMSO), 1 μM blebbistatin (Blebb) or 10 μM RO-3306 (RO) for 12 hours. Scale bar = 30 μm . (B) Representative XZ plane images of DAPI stained nuclei of DMSO, Blebb and RO-treated cells. Scale bar = 5 μm . (C) Quantitative analysis of nuclear volume ($n = 20 - 50$ nuclei per condition across 2 independent experiments). Error bars represent $\pm\text{SEM}$. Statistical significance was determined by one-way ANOVA/Fisher Test; NS: $p > 0.05$. (D) Probing nuclear stiffness of cells with a stiff pyramidal probe. Cells were treated with DMSO, Blebb or RO for 12 hours prior to experiments. Nuclear stiffness values were estimated by fitting $\geq 2 \mu\text{m}$ of indentation data using Hertz model. (E) Quantification of nuclear stiffness of DMSO-treated, Blebb-treated and RO-treated cells ($n = 40 - 60$ nuclei per condition across 2 independent experiments). Error bars represent $\pm\text{SEM}$. Statistical significance was determined by one-way ANOVA/Fisher Test; * $p < 0.05$, *** $p < 0.001$. (F) Schematic of transwell migration assay through 3 μm pores; Cells were seeded in the upper chamber containing plain DMEM supplemented with DMSO or drugs. Lower chamber was labelled with DMEM containing 20% serum for creating a chemokine gradient. 49

2.13 Influence of nuclear stiffness on pore migration efficiency and nuclear plasticity. (A) Representative DAPI stained images of nuclei in upper chamber (referred to as TOP) and lower chamber (referred to as BOTTOM) at 8, 18 and 28 hrs after cell seeding; Scale bar = 100 μm . (B) Quantification of translocation efficiency of DMSO/Blebb/RO-treated cells at 3 different time-points ($n \geq 900$ nuclei per condition were counted in the upper chamber; experiment was repeated thrice). (C) Quantification of nuclear circularity of DMSO/Blebb/RO-treated cells at the top (8 hr time point) and at the bottom surface of the pores at 3 different time-points ($n > 80$ nuclei per condition; experiment was repeated twice). Error bars represent $\pm\text{SEM}$. Statistical significance was determined by one-way ANOVA/Fisher Test; *** $p < 0.001$, ** $p < 0.01$, NS: $p > 0.05$ 50

2.14 Plastic deformation of the nucleus increases susceptibility to damage. (A) Representative γ H2Ax-stained images of DMSO/Blebb/RO-treated cells in upper chamber (referred as TOP) and lower chamber (referred as BOTTOM) of transwell pores 28 hrs after cell seeding. Nuclei are outlined with white dotted lines; Scale Bar = 20 μ m. (B) Quantification of ratio of integrated γ H2Ax intensity between BOTTOM layer and TOP layer in DMSO/Blebb/RO-treated cells ($n = 40 - 120$ nuclei per condition; experiment was repeated twice). Error bars represent \pm SEM. Statistical significance was determined by Mann-Whitney test; *** $p < 0.001$, NS: $p > 0.05$. (C) Quantification of γ H2AX expression intensity normalized to DMSO condition at the TOP layer. 51

2.15 Plastic deformation of the nucleus increases susceptibility to damage. (A) Representative Lamin A/C (green) and DAPI (blue) stained images of DMSO/Blebb/RO-treated cells in Top and Bottom layer of transwell pores at 28 hrs after cell seeding. White arrows indicate nuclear blebs. Scale bar = 20 μ m. (C) Quantification of average number of blebs per nucleus in DMSO/Blebb/RO-treated cells in top and bottom layer of the transwell inserts ($n > 250$ nuclei per condition pooled from two independent experiments). Error bars represent \pm SEM. Statistical significance was determined by Mann-Whitney test; *** $p < 0.001$, NS: $p > 0.05$ 52

2.16 Scaling relationships. (A) Scaling relationship between F_{entry} (pN/ μ m) and T_{entry} (s) for $D_0/\phi = 1.67$. (B) Non-dimensional cellular force scaled with possible parameters affecting the cellular force generation during confined migration for $D_0/\phi = 1.67$. Scaling between nuclear circularity and (C) the coupled effect of tissue and nuclear stiffness, and (D) force required by a cell to enter a pore. All datapoints refer to the condition $D_0/\phi = 1.67$. E_1 and E_2 vary from 0.13 to 5 kPa. 55

2.17	Proposed model of nuclear damage. (A) Phase diagram depicting the zones of non-plastic and plastic nuclear deformation required for pore entry for different values of E_n , E_T and D_0/ϕ . (B) Proposed model of nuclear damage. Compressive forces imposed by the surrounding tissues cause initial nuclear membrane damage. This serves as the precursor to nuclear bleb formation.	57
3.1	Glycocalyx attached to plasma membrane of cells. (A) Schematic of an AFM probe indenting a glycocalyx brush. (B) Enzymatic removal of cell surface glycocalyx. MDA-MB-231 Cells were treated with 0 and 500 milliunit (mE) neuraminidase for 3 h and was fixed and stained with WGA-FITC to visualize surface glycan. Images are representative confocal maximum intensity images. (C) Glycocalyx mediates invasiveness of MDA-M-231 cells. Invasion was checked after encapsulating cells in 3D collagen gels using live cell imaging. Figure shows 12 h migration trajectories. (D) Quantification of the cell migration trajectories over 12 h ($n>120$ cells from 2 independent experiments, Statistical significance were determined using Mann-Whitney test, ***: $P<0.001$). 63	63
3.2	Variation of brush stiffness E with glycocalyx thickness L, density N and indentation depth δ. The units of L and N are μm and μm^{-2} respectively. The range of validity of the brush model by Dokukin et al. (2016) is also indicated by the dotted lines. The value of E taken in simulations corresponds to $h/L = 0.8$ (corresponding to a 20% indentation depth, or $\delta/L = 0.2$).	65
3.3	Variation of brush stiffness E with glycocalyx thickness L, density N at indentation depth $h/L = 0.8$ or $\delta/L = 0.2$. The units of L and N are μm and μm^{-2} respectively. The colorbar indicates the value of effective stiffness E , in Pa, calculated from the entropic brush model and the Hertz contact model. . . .	66
3.4	Model schematics used for simulations of spherical indentation of a cell with glycocalyx surrounding it. A rigid indenter of radius = $10 \mu m$ is displaced by 40% of initial glycocalyx thickness (L). The axis of symmetry, boundary conditions of the system and undeformed dimensions are shown. The axial and radial directions are denoted in the figure by Z and R respectively. . .	69

3.5	Model schematics used for simulations of glycocalyx compression due to cells sandwiched between a rigid plate and ECM. Two degrees of cell spreading area were studied, denoted by radii of $1 \mu\text{m}$ and $10 \mu\text{m}$ and the initial glycocalyx thickness was taken to be either $1 \mu\text{m}$ or $5 \mu\text{m}$. The rigid plate is displaced in the axial direction by $1 \mu\text{m}$. The axial and radial directions are denoted in the figure by Z and R respectively.	70
3.6	von Mises stress contours in cell body and cell glycocalyx for $N = \{100, 200, 500\} \mu\text{m}^{-2}$ and (A) $L = 1 \mu\text{m}$, (B) $L = 5 \mu\text{m}$, and (C) $L = 10 \mu\text{m}$. Maximum indentation depth δ/L is 0.4.	73
3.7	Variation of normal indentation load F with relative indentation depth h/L for $L = \{1, 5, 10\} \mu\text{m}$ and $N = \{100, 200, 500\} \mu\text{m}^{-2}$. Green dashed line and arrow mark the region beyond which the brush model is applicable. Maximum indentation depth δ/L is 0.4.	74
3.8	von Mises stress contours in cells along with the glycocalyx for $L = 1 \mu\text{m}$ and $N = \{1000, 10,000\} \mu\text{m}^{-2}$. Two combinations of E_{cell} and E_{ECM} are analyzed where $E_{cell} = 2 \text{ kPa}$ and $E_{ECM} = \{1, 5\} \text{ kPa}$ were used for the simulations. Colourbar depicts the von Mises stress.	75
3.9	von Mises stresses in the deformed cellular glycocalyx along the axis of symmetry for: (A-D) $L = \{1, 5\} \mu\text{m}$ and $N = \{100, 1000\} \mu\text{m}^{-2}$. Various combinations of $E_{cell} = \{0.5, 2\} \text{ kPa}$ and $E_{ECM} = \{1, 5\} \text{ kPa}$ were used for the simulations.	76
3.10	Normal contact forces between the cellular glycocalyx and ECM for: (A-D) $L = \{1, 5\} \mu\text{m}$ and $N = \{100, 1000\} \mu\text{m}^{-2}$. Various combinations of $E_{cell} = \{0.5, 2\} \text{ kPa}$ and $E_{ECM} = \{1, 5\} \text{ kPa}$ were used for the simulations.	77
3.11	ECM axial displacement along the axis of symmetry for: (A-D) $L = \{1, 5\} \mu\text{m}$ and $N = \{100, 1000\} \mu\text{m}^{-2}$. Various combinations of $E_{cell} = \{0.5, 2\} \text{ kPa}$ and $E_{ECM} = \{1, 5\} \text{ kPa}$ were used for the simulations.	78

3.12	ECM displacement due to a sandwiched cell for $L = \{1, 5\} \mu\text{m}$ and $N = 10,000 \mu\text{m}^{-2}$. (A) ECM displacement in +y-direction along the contact surface (longitudinal direction) of ECM and cell for a cell spread radius of $1 \mu\text{m}$. (B) ECM displacement in +y-direction along the contact surface (longitudinal direction) of ECM and cell for a cell spread radius of $10 \mu\text{m}$. Various combinations of $E_{cell} = \{0.5, 2\}$ kPa and $E_{ECM} = \{1, 5\}$ kPa were used for the simulations. Solid curves indicate $L = 1 \mu\text{m}$ and dashed curves indicate $L = 5 \mu\text{m}$	79
3.13	Mechanical implications of glycocalyx as a double brush. (A) Contact force between the glycocalyx and ECM, and (B) ECM vertical displacement u_y along its entire length, for $\{L_1, L_2\} = \{1, 5\} \mu\text{m}$ and $\{N_1, N_2\} = \{10,000, 1000\} \mu\text{m}^{-2}$. Dotted curves represent a cell spread radius of $10 \mu\text{m}$ and solid curves represent a cell spread radius of $1 \mu\text{m}$. Various combinations of $E_{cell} = \{0.5, 2\}$ kPa and $E_{ECM} = \{1, 5\}$ kPa were used for the simulations.	80
4.1	Flowchart of the modelling process.	86
4.2	A cross-sectional schematic of indentation of a soft tissue with an embedded nodule. The indenter of radius R is hemispherical and nodule of diameter D and depth d is spherical. The nodule is embedded in a tissue of finite thickness h . A prescribed indentation depth δ leads to the generation of an indentation load F	88
4.3	A representative finite element model depicting the axisymmetric setup where the indenter is displaced downwards (-y direction) along the axis of symmetry. Boundary conditions are also marked. Radial and axial directions are denoted by x-axis and y-axis respectively.	89
4.4	Model validation with experimental data of spherical indentation. The dependence of indentation load (F) on the ratio of indentation depth (δ) to indenter radius ratio (R) is shown. Data from our simulations are compared with experimental data from Zhang et al. (2014).	93

4.5 **Comparison of the computationally generated indentation load F_0 with analytical Hertzian solution F_H up to a maximum indentation depth $\delta = 2$ mm.** Homogeneous tissues (without nodule) of various thicknesses (h) are considered. 99

4.6 **Instantaneous tissue stiffness measured as a function of indentation load and depth.** (A) Relation of instantaneous tissue stiffness ($dF/d\delta$) with the indentation depth normalized by tissue thickness (δ/h). (B) Relation between $dF/d\delta$ and $\sqrt{R\delta}$, parameters of the Hertz model to determine composite tissue stiffness. Both plots are for $h = 10$ mm, $R = 3$ mm and $D = 5$ mm. 100

4.7 **Dependence of nodule detectability on nodule depth.** (a) Variation of F/R^2G_0 with d/R for $R = 3$ mm (dashed line) and 5 mm (dotted line). (b) Variation of F/R^2G_0 with d/R for $\delta/h = 0.05$ (dotted line) and 0.1 (dashed line). Both (a) and (b) refer to cases where $G_n/G_0 = 15$ and $D = 5$ mm. The power-law dependence is denoted beside the fitted curve. 101

4.8 **Dependence of nodule detectability on nodule diameter.** (a) Variation of F/R^2G_0 with D/R for $R = 3$ mm (dashed line) and 5 mm (dotted line), and (b) Variation of F/R^2G_0 with D/R for $\delta/h = 0.05$ (dotted line) and 0.1 (dashed line). G_n/G_0 and d in all cases were fixed at 15 and 0.5 mm respectively. The power-law dependence is denoted beside the fitted curve. 103

4.9 **Effect of anisotropy on nodule detection.** (A) A schematic of GOH material model. a_{01} and a_{02} denote two fiber families of same mechanical properties but separated by an angle 2γ embedded in a fibrous tissue. (B) Dependence of indentation load F on fiber orientation κ for isotropic nodule embedded in anisotropic tissue (blue circles) and for anisotropic nodule embedded in isotropic tissue (red squares). Both curves correspond to $d/R = 0.17$, $D/R = 1.67$ and $\delta/h = 0.1$. (C) Stress profiles in anisotropic tissue embedded with isotropic nodule under indenter from tissue surface to end of nodule. The change in von Mises stress profiles is shown for various degrees of fiber dispersion. (Inset) Stress profiles just under the indenter are magnified for clarity. All curves correspond to $d/R = 0.17$, $D/R = 1.67$ and $\delta/h = 0.1$. (D) Stress profiles in isotropic tissue embedded with anisotropic nodule under indenter from tissue surface to end of nodule. All curves correspond to $d/R = 0.17$, $D/R = 1.67$ and $\delta/h = 0.1$. (C, D) The change in von Mises stress profiles is shown for various degrees of fiber dispersion. (B-D) For anisotropic nodule embedded in isotropic tissue, initial $G_n = 24.6$ kPa, initial $G_0 = 10$ kPa, while for isotropic nodule in anisotropic tissue, initial $G_n = 250$ kPa, initial $G_0 = 24.6$ kPa. 105

4.10 **Palpation sensitivity chart for $\% \Delta F / F_0$ versus nodule diameter and depth relative to indenter radius for $G_n / G_0 = 5, 10$ and 15 for large indentation depths $\delta/h = 0.1$ and 0.2 .** Grayscale represents the value of $\% \Delta F / F_0$. The detectable and undetectable regimes and $\% \Delta F / F_0$ of contour lines $> 20\%$ (detection threshold) are indicated for all cases. 108

4.11 **Summary of the contributions of this study on embedded nodule detection.** 110

List of Abbreviations

CT	Computed Tomography
ECM	Extracellular Matrix
MMP	Matrix Metalloproteinase
ER	Endoplasmic reticulum
TFM	Traction Force Microscopy
AFM	Atomic Force Microscopy
SLS	Standard Linear Solid
FA	Focal Adhesion
2D	Two Dimensional
3D	Three Dimensional
EMT	Epithelial to Mesenchymal Transition
PDMS	Polydimethylsiloxane
LINC	Linker of the Nucleoskeleton and Cytoskeleton
DNA	Deoxyribonucleic Acid
PCM	Pericellular Matrix
HA	Hyaluronic Acid
BM	Basement Membrane
ABP	Actin Bundling Protein
FE	Finite Element
FEM	Finite Element Method
BC	Boundary Condition
PDE	Partial Differential Equation
DMEM	Dulbecco's Modified Eagle Media

FBS	Fetal Bovine Serum
PFA	Paraformaldehyde
DAPI	4',6-diamidino-2-phenylindole
γH2Ax	Gamma H2A histone family member X
BSA	Bovine Serum Albumin
PBS	Phosphate Buffer Solution
Blebb	Blebbistatin
CDK	Cyclin-dependent Kinase
DMSO	Dimethyl Sulfoxide
SEM	Standard Error of the Mean
ANOVA	Analysis of Variance
HGPS	Hutchinson Gilford Progeria Syndrome

List of Symbols

H^+	Hydrogen ion (proton)
OH^-	Hydroxide ion
$\gamma_{dev}(t)$	Deviatoric strain as a function of time
$\sigma_{dev}(t)$	Deviatoric stress as a function of time
G_0	Instantaneous shear modulus
$G_R(t)$	Time-dependent shear relaxation modulus
$g_R(t)$	Dimensionless time-dependent shear relaxation modulus
$\sigma_{vol}(t)$	Time-dependent volumetric stress
$p(t)$	Time-dependent hydrostatic pressure
K_0	Instantaneous bulk modulus
$K_R(t)$	Time-dependent bulk relaxation modulus
$k_R(t)$	Dimensionless time-dependent bulk relaxation modulus
E_0	Young's modulus
ν	Poisson's ratio
τ_i	Relaxation time; $i = 1, 2, \dots, N$
ϵ_{vol}	Volumetric strain
$[K$] Spring stiffness matrix
$\{u\}$	Displacement vector
$\{F\}$	Force vector
E_c	Young's modulus of cytoplasm
σ_{shear}	Shear stress
ρA	Density
F_p	Cell-generated protrusion force

Δt	Stable time increment
L_{min}	Smallest mesh dimension
c_d	Dilatational wave speed through element
N_t	No. of DAPI stained nuclei on top surface of transwell membrane per frame
N_b	No. of DAPI stained nuclei on top surface of transwell membrane per frame
ϕ	Undeformed pore size for cell migration
D_0	Undeformed diameter of nucleus
E_T	Young's modulus of tissue
E_n	Young's modulus of nucleus
E_1, E_2	Young's modulus of Tissue 1 and Tissue 2
T_{entry}	Time for pore entry of nucleus
F_{entry}	Maximum force required for pore entry of nucleus
v_x	Cell velocity along direction of migration
u_y	Vertical tissue displacement
$\langle v_x \rangle$	Mean cell speed in direction of migration
x_{CN}	Normalized distance between cell leading edge and nucleus proximal edge
D/L	Nuclear circularity
σ_{Mises}	von Mises stress
$\sigma_{\theta\theta}$	Hoop stress
σ_{rr}	Radial stress
$\epsilon_{plastic}$	Plastic strain
ϵ_{total}	Total strain
$\epsilon_{elastic}$	Elastic strain
τ_c	Relaxation time constant of cytoplasm
F_D	Flexural rigidity
D_c	Diffusion coefficient of water

σ_y	Yield stress
$F_{single\ brush}$	Force due to brush polymer chains of the same length
k_B	Boltzmann constant
T	Temperature
R_{probe}	Radius of indenter probe
R_{cell}	Radius of cell
N	Brush density
L	Brush thickness
F_{Hertz}	Hertz contact force
ν_{probe}	Poisson's ratio of indenter probe
$\nu_{glycocalyx}$	Poisson's ratio of glycocalyx
E_{probe}	Young's modulus of indenter probe
$E_{glycocalyx}$	Young's modulus of glycocalyx
h	Distance between indenter tip and cell body
$F_{double\ brush}$	Force due to brush polymer chains of two different lengths
Ψ	Strain energy function
C_1	Material constant for Neo-Hookean model
D_1	Material constant for Neo-Hookean model
I_1	1st invariant or trace of right Cauchy-Green deformation tensor
λ_i	Principal stretches; $i = 1, 2, 3$
J	Determinant of deformation gradient
E_{cell}	Young's modulus of cell
E_{ECM}	Young's modulus of ECM
G_n	Shear modulus of tumor nodule
G_0	Shear modulus of healthy tissue
d	Nodule depth

u_x	Displacement in x-direction
λ_m	Limiting stretch ratio
ϕ	Angle between mean directions of two families of fibers
λ_n	Stretch ratio of nodule
ν_n	Poisson's ratio of nodule
F_{Hayes}	Force predicted by the Hayes model
a	Radius of contact circle formed between indenter and substrate
ω	Factor used to introduce the effect of substrate thickness on F_{Hayes}
F_{FE}	Force predicted by finite element model
C, k_1, k_2	Material parameters of GOH model
σ_{11}	Uniaxial stress (normal stress) in loading direction
κ	Fiber dispersion index
ΔF	Difference in indentation load with and without embedded nodule

Chapter 1

Introduction

1.1 Introduction to Cancer

Cancer is one of the leading causes of death globally. A report by the National Institutes of Health (NIH) states that globally, an estimated 8.2 million people died of cancer in 2012 (NIH, 2018). Of these deaths, nearly 65% occurred in underdeveloped regions of the world including parts of Asia. A WHO report puts the same figure in 2018 as 9.6 million deaths and nearly 1 in 6 individuals globally getting affected by cancer (WHO, 2018). Research into cancer, its causation and therapeutics has been a hot topic for decades with some tangible results. In understanding cancer, one of the often neglected aspects is the mechanics that is involved in it. Understanding the mechanics of cancer and exploiting it for diagnostic and therapeutic purposes hold great promise both at the cellular and the tissue levels.

A major reason why cancers are so difficult to treat completely is that they proliferate and spread to various parts of the body. It is extremely difficult to specifically target the regions where cancer cells might be lodged in the body without harming the healthy cells as far as possible. Moreover, cancers tend not to reveal themselves until they reach a critical mass by when valuable time is already lost. Talmadge and Fidler (2010) note that the processes of tumor initiation, progression and metastasis are extremely slow and develop over several years (10-12 or even more) before they reach the size (≈ 1 cm and $\approx 10^9$ cells) when they can be detected by imaging technologies (Fig. 1.1). Cancers such as lung cancer are broadly classified into 6 categories based on preclinical stage: *IA*, *IB*, *II*, *IIIA*, *IIIB* and *IV*. The preclinical stage of cancer development is positively correlated to its detectability using diagnostic techniques such Computed Tomography (CT) with sensitivity for the first stage (*IA*) being as low as 8.83% (ten Haaf et al., 2015). It is therefore imperative that novel detection techniques be devised and

mechanics of cancer progression at the cell and tissue levels be studied to effectively counter cancer.

Cancer cells have a high propensity to migrate through confined environments, for instance, squeezing through layers of epithelial cells to access the bloodstream (intravasation) and extravasating out to form a secondary tumor at a distant location. Cancer cells have been shown to be softer than healthy cells (Suresh et al., 2005; Guck et al., 2005; Suresh, 2007; Cross et al., 2007) and they survive extreme deformations caused due to squeezing through tight spaces. Cancer cells differ from normal cells in that they differentiate more and can metastasize to other remote regions of the body. Similarly, immune cells have been reported to have lamin A-deficient nuclear lamina and therefore, can be easily deformed due to reduced structural integrity of nuclei (Rowat et al., 2013).

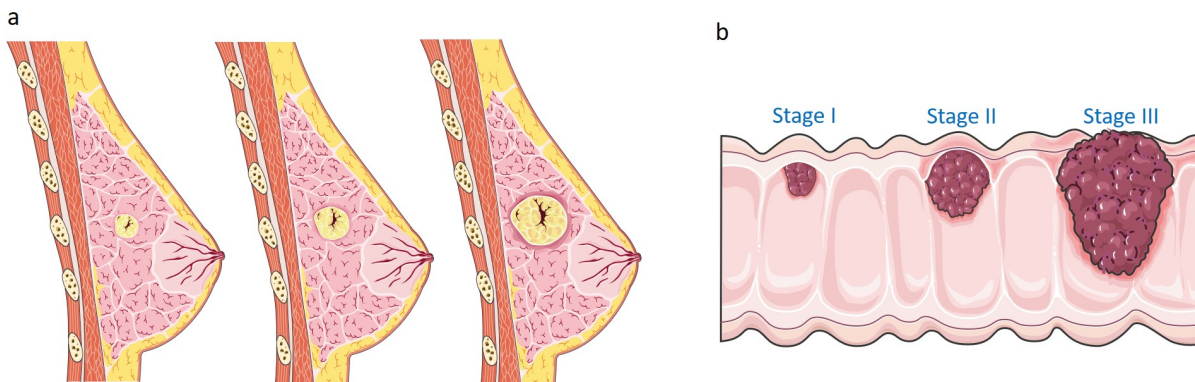


Figure 1.1: **Growth of a tumor over time.** (A) Tumor growth in breast cancer. (B) Tumor growth in colon cancer.

1.2 The Extracellular Matrix (ECM) in Cancer

Tissues primarily comprise of three components: cells, extracellular matrix (ECM) and blood vessels. The ECM serves as a scaffold and lends structure to cells and tissues and facilitates mechanotransduction (Frantz et al., 2010; Sapir and Tzlil, 2017). Cell cytoskeleton is linked to the ECM via integrin-based adhesions. The dynamic nature of cell-ECM coupling drives or modulates cell migration through this matrix (Schmidt and Friedl, 2010). The ECM might also lead to change in signalling pathways and modulation of micro and macroscopic properties of tissues. There exists a complex network of mechanotransduction and signalling pathways

between cells, ECM and tissue boundaries with the ECM often acting as a mediator.

The ECM is composed of complex sugars, proteins and water (Frantz et al., 2010). It remodels itself depending on pathological conditions such as cancer, wounds and aging. Proteins such as collagen, elastin and fibronectin are mainly associated with the ECM (Alberts et al., 2007). All these constituents result in the ECM being a heterogeneous matrix. Collagen fibrils, one of the most abundant proteins in ECM of tissues facilitate cell migration, adhesion and remodelling of tissues apart from imparting mechanical structure and strength (Rozario and DeSimone, 2010). Tissue compliance greatly correlates with collagen fibres orientation, stiffening and crosslinking (Frantz et al., 2010). Normal and healthy tissues are more compliant than tumors despite the fact that cancer cells are generally softer than healthy cells. This results from the fact that the ECM in tumor tissues is stiffer than in healthy tissues. The increased stiffness of tumors acts as a marker to detect embedded cancerous nodules in healthy tissues and indicates the stage of progression of cancer as can be evidenced by a nearly 10-fold increase of stiffness of mammary tissue due to increased collagen deposition and crosslinking (Handorf et al., 2015). Altered ECM dynamics such as excess production of ECM or greater deposition of various types of collagen might be an indicator of cancers (Huijbers et al., 2010; Frantz et al., 2010). In addition to biochemical changes like increased production of matrix metalloproteinases (MMPs) and growth factors such as CD44 by cancer cells, the collagen fibers in the ECM transition from a non-oriented fashion to highly oriented tracks that facilitate cell migration (Levental et al., 2009). This is accompanied by deregulation of ECM remodelling enzymes (Lu et al., 2012).

1.2.1 The ECM as a Mechanical Barrier to Invasion

The ECM with its constituent collagen fibers and protein macromolecules act as a barrier to cell migration in 3D. Directional collagen fibers may sometimes serve as tracks for adhesion-dependent migration of cells, but randomly aligned fibers may impede migration by inducing mechanical confinement. A feedback mechanism exists between cells and the ECM and therefore, any change in physical properties of the ECM leads to changes in cell signalling and properties as well (Samuel et al., 2011). Migrating cells can undergo either protease-independent or protease-dependent migration through subnuclear-sized confining matrices or

pores. If cells are unable to sufficiently squeeze through or adequately deform matrices, for instance in densely packed and stiff ECM, then they secrete matrix metalloproteinases (MMPs) to degrade the ECM (Kumar et al., 2016; Wisdom et al., 2018). Highly invasive cancer cells, such as MDA-MB-231 and HT1080 with softened and compliant nuclei were shown to readily deform under matrix-induced confinement after treatment by MMP inhibitors (Das et al., 2019). Cells transiting through highly plastic matrices were also shown to migrate in a protease-independent manner (Wisdom et al., 2018). Actin-rich invadopodia of cells can either be used to secrete MMPs to degrade ECM or mechanically push open pores in the ECM for effective cell migration (Friedl and Wolf, 2010; Kumar et al., 2016, 2018a; Wisdom et al., 2018).

1.2.2 Rheology of soft materials

Rheology is the study of mechanical deformation of objects or bodies and is generally used to describe the flow of materials under external forces. This deformation is intrinsically linked to the material properties of the system. Soft materials such as cells and tissues are highly complex and inhomogeneous, with a variety of internal structures that directly or indirectly influence the rheology of these materials. For instance, cells are composed of organelles such as nucleus, endoplasmic reticulum, mitochondria and cytoskeleton-forming protein filaments like actomyosin fibers and microtubules (Fig. 1.2a and b). These constituents render cellular rheology to be time and strain-rate dependent and transform dynamically in response to external forces and stresses. Therefore, rheological characteristics of such materials can only be approximately quantified at a somewhat coarse-grained level.

Cells continually remodel their cytoskeleton under application of stresses and therefore, rheological models should ideally capture this behaviour (Gardel et al., 2004a,b). Soft materials like cells and tissues can be considered to be elastic, hyperelastic or viscoelastic depending on the timescales and strains involved. For instance, a material can be modeled to be elastic if the strain and timescale of deformation are extremely small with respect to the dimensions of the substrate and relaxation timescales of the material respectively. If material deformation is large enough to be comparable to the dimensions but much lower than material relaxation timescales, then a hyperelastic model is more suited that takes large nonlinear deformations under consideration. However, cyclic and time-dependent strains are more appropriately modelled by vis-

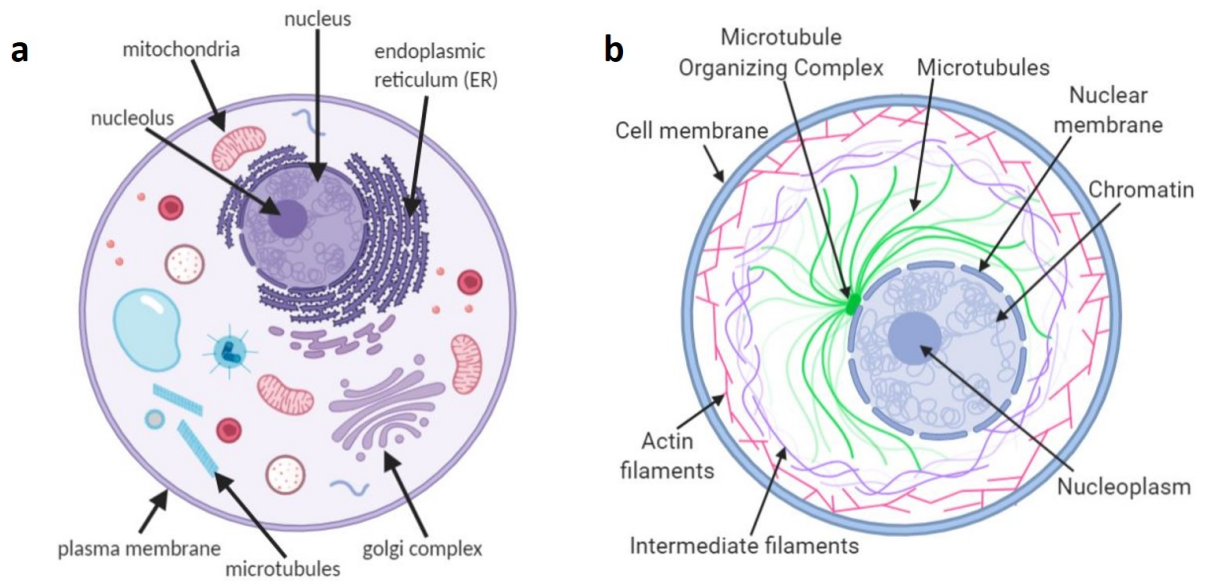


Figure 1.2: **Intracellular components of a representative cell.** (a) A typical cell with organelles. (b) Essential filamentous constituents of a typical cell. Created with BioRender.

coelastic models. This is because neither elastic nor hyperelastic models are time-dependent. Therefore, the physical phenomenon of, for example, phase lag between indentation load and substrate surface displacement can be modelled realistically by considering the substrate as a viscoelastic body.

Rheology of cells has been experimentally quantified using some common techniques:

1. Bulk rheology technique - A sample is placed between two parallel plates oscillating at a certain frequency. This technique is popularly used to quantify the viscoelastic properties of cells. This technique cannot be used at high frequencies (> 100 Hz) due to instrument inertia (Del Giudice et al., 2017). Another limitation is that very low viscosity fluids are difficult to be measured by this process.
2. Magnetic bead cytometry - A magnetic bead is tracked by laser under application of an external magnetic field (Hoffman et al., 2006). It gives a quantitative measurement of the local mechanical properties of cells. However, uncertainties related to bead attachment to the substrate lead to uncertainties in mechanical property quantification (Kasza et al., 2007).
3. Microfluidics - Cells are passed along with fluid through micron-sized channels to study their rheological properties under fluid-induced shear (Lange et al., 2015; Mietke et al.,

2015).

4. Atomic force microscopy (AFM) - A cell is indented by a cantilever tip and a quantification of the tip deflection gives the cell stiffness (Sen et al., 2005). This is a widely used method to extract mechanical properties of cells non-invasively. It has a distinct advantage over other methods listed here in that it is able to scan and generate entire cell profile for multiple cells. However, it is a very low throughput technique (≈ 10 cells/h).
5. Microrheology technique - The motion of beads embedded in cells is tracked over time. This is a more general method than magnetic bead cytometry. It involves multiple beads inserted in cells whose movement under the influence of thermal fluctuations is studied over time to determine elastic material properties of the cell. However, bead movement is not just influenced by thermal fluctuation, but also by cytoskeletal filament dynamics and motor proteins (Hoffman et al., 2006).

1.2.3 Modeling the rheology of cells and tissues

Elastic models

The simplest rheological model of cells and tissues is a linear elastic model. Linear elastic models have been used extensively in studies under small strains to quantify and model various mechanical characteristics of cells and tissues (Theret et al., 1988; Esteban-Manzanares et al., 2017). However, such models have limited applicability as most cells and tissues regularly undergo large nonlinear strains and therefore, a material model to incorporate large strain behaviour is needed.

Hyperelastic models

Nonlinear elastic or hyperelastic models are used to model systems that undergo large deformations beyond the small strain elastic limit. The stress increases nonlinearly with large strains for such materials like rubber and soft tissues. Hyperelastic models have often been used to model tissues (Zhang et al., 2014) and cells (Zhou et al., 2005; Cao et al., 2016). Some of the common hyperelastic models are as follows:

1. Mooney-Rivlin
2. Neo-Hookean
3. Ogden
4. Arruda-Boyce
5. Yeoh
6. Fung

Of these models, the Arruda-Boyce and Neo Hookean models are mechanistic models derived from theoretical considerations of the microstructure of the material, whereas, the others are phenomenological, which, though consistent with theory, were not derived from first principles. All hyperelastic models are described by a strain-energy density function that can be used to define the stress-strain behaviour of these models.

Viscoelastic models

Soft materials have time- and strain-rate dependent mechanical properties. Such time-dependent dynamic behaviour is better captured by viscoelastic models as opposed to rate-independent elastic and hyperelastic models (Guilak et al., 2000; Trickey et al., 2004; Desprat et al., 2005; Zhou et al., 2005; Han et al., 2012). A viscoelastic system is composed of a combination of elastic springs and viscous dampers. A spring is capable of undergoing instantaneous deformation on the application of a force. A damper, on the other hand, gradually deforms to reach a steady saturated state of deformation, provided that the force is applied for a sufficient amount of time. Therefore, viscoelastic materials behave as elastic if the time duration of deformation of the system is instantaneous or very short when compared to relaxation time constant of the material. Spring-damper models have classically been employed to model muscle contraction and extension and indentation of soft tissues apart from numerous other industrial applications. Such models can be broadly classified into three categories:

1. Maxwell model - spring and damper in series configuration,
2. Kelvin-Voigt or Voigt model - spring and damper in parallel configuration,

3. Standard Linear Solid (SLS) model - A spring in series with a Voigt configuration

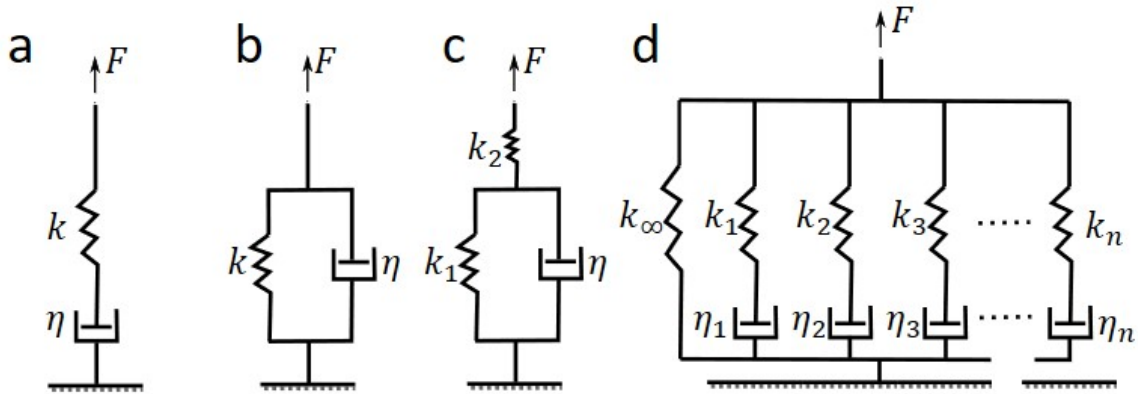


Figure 1.3: **Schematics of common viscoelastic models.** (A) Maxwell model, (B) Voigt model, (C) Standard Linear Solid (SLS) model, and (D) Generalized Maxwell model. k and η denote spring stiffness and damper viscosity respectively.

The schematics of these three models are as shown in Fig. 1.3. The Maxwell model (Fig. 1.3a) results in a linear creep strain upon sudden application of stress and a sudden elastic drop in strain upon stress removal. On the other hand, the Voigt model (Fig. 1.3b) results in a nonlinear creep strain that saturates with time and an inelastic recovery phase. Therefore, the Kelvin-Voigt model is better at modelling creep behaviour seen in cellular materials. The SLS model (Fig. 1.3c) is a combination of both the Maxwell and Voigt model and thus is capable of effectively modelling both creep and stress relaxation of a substrate. A generalized Maxwell model contains several Maxwell components in parallel (Fig. 1.3d). It may be used to model systems that have a set of relaxation times due to a set of material components. A generalized Voigt and a generalized SLS model are similar to a generalized Maxwell model.

1.3 Cancer Metastasis

Cancer metastasis refers to the process of cancer cells getting dislodged from a primary tumor mass, travelling through the vasculature and creating a new tumor mass at a distant location. Cancer metastasis can be attributed to $\sim 90\%$ of deaths due to cancer worldwide (Gupta and Massagué, 2006). Cancer cells generally migrate either in mesenchymal or amoeboidal mode (Zhu and Mogilner, 2016). Cells migrating in the mesenchymal mode are generally

elongated and spindle-shaped with focal adhesions, whereas, in the amoeboidal mode, cells are more rounded with minimal adhesion with ECM. Whereas mesenchymal migration utilizes MMP-based ECM degradation to clear space for the cell to migrate, amoeboidal migration does not use MMPs but requires larger pore sizes to migrate ($> 7 \mu m^2$) (Wolf et al., 2013). Confinement of cells has been shown to lead to changes in intracellular signalling (Hung et al., 2016). Cells interchangeably undergo mesenchymal and amoeboidal migration in confined conditions, undergoing mesenchymal to amoeboidal transition (MAT) or vice-versa (AMT) depending on which molecular mechanism is suppressed. Studies show that while the mesenchymal mode acts upon Rac-activated actin protrusion, the amoeboidal mode depends on Rho-activated myosin contractility (Sanz-Moreno et al., 2008). Metastatic cancer cells have been characterized by a distinct lack of polarity over healthy cells that results from weakened or minimal cell-cell and cell-ECM adhesions and amoeboid migration (Schmidt and Friedl, 2010; Lu et al., 2012).

Tumors are generally a genetically heterogeneous population of cells which contain some cells that have certain metastasis-favouring mutations (Gupta and Massagué, 2006). Highly metastatic cells have been found to have greater genetic mutability and DNA alterations. Cancerous tumors require greater supply of oxygen and nutrients and therefore, a new network of blood vessels and capillaries are formed around the tumor (Carmeliet and Jain, 2000). The cancer metastasis process in general is comprised of the following essential steps as shown in Fig. 1.4:

1. Dislodgement of a cancer cell due to loss of cell-cell adhesion in primary tumor
2. Simultaneous epithelial to mesenchymal transition of dislodged cancer cell
3. Migration of cancer cell through ECM mesh
4. Intravasation or entry of cancer cell in blood vessel by invading epithelial tissue lining of vessel wall
5. Transit of cancer cell via the bloodstream to a distant location
6. Attachment or adherence of cancer cell to the epithelial tissue lining of vessel wall
7. Extravasation or exit of cancer cell from blood vessel by invading through epithelial tissue lining and into ECM of target tissue

8. Formation of secondary tumor at target site

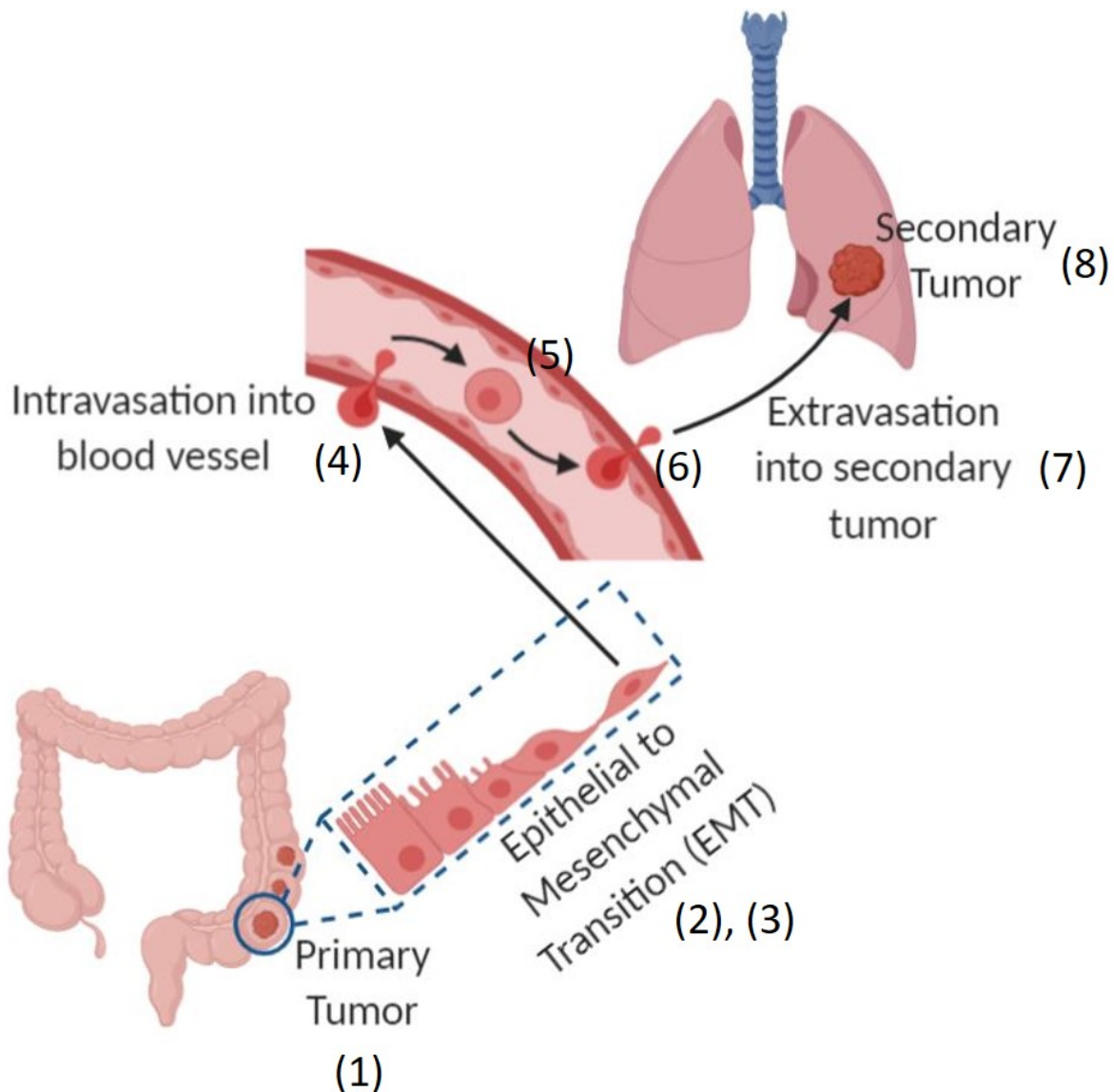


Figure 1.4: **Schematic of the process of cancer metastasis.** Created with BioRender.

1.4 Mechanisms of Invasion

There is a stark contrast between the mechanisms of cell migration in 2D and 3D. While in 2D, cells migrating on a substrate predominantly produce cyclic protrusions and retractions of an actin-rich lamellipodium while simultaneously generating focal adhesions (FAs), a cell migrating in 3D does not have a unique mechanism of migration (Fig. 1.5) (Yamada and Sixt,

2019). In fact, cells may use various mechanisms, sometimes multiple to migrate depending mainly on the degree and type of confinement, actomyosin contractility and focal adhesions. While focal adhesions are critical to migration on 2D substrates, mechanical confinement alone can sometimes be sufficient for cells to migrate in 3D (Paluch et al., 2016; Reversat et al., 2020). A comprehensive map of types of cell migration and conditions leading to these are summarized in Paul et al. (2017). Tissue invasion predominantly occurs in 3D through matrices or epithelial cell layers. Two modes of 3D migration become exceptionally important during invasion: mesenchymal mode and amoeboidal mode. While the former relies on degradation of the ECM by secreting enzymes such as MMPs and migrates with the aid of FAs, the latter does not require FAs and MMPs to migrate (Paul et al., 2017; Yamada and Sixt, 2019). The mode that a cell would use to invade a tissue depends on mechanical environmental factors such as stiffness and confinement and on molecular signalling mechanisms in the cell.

The cytoskeleton is a critical component in cell migration and invasion. Studies show that cancer cells generate actin-rich invadopodia during intravasation into blood vessels and extravasation out into tissues (Leong et al., 2014). Invadopodia are actin-rich protrusions that are stiff and are created by polymerization of parallel-oriented actin filaments. These structures are created by cells for two primary purposes: to release MMPs to degrade the local matrix and to mechanically separate endothelial cells or matrix fibers to make space for cell migration (Kumar et al., 2018a; Das et al., 2019). Microtubules impart structural stability to the cell and nucleus during confined migration and vimentin intermediate filaments have been recently found to facilitate fast amoeboid migration (Lavenus et al., 2020). Additionally, bundling of vimentin intermediate filaments are found to impede cancer cell invasion. Under ECM-induced confinement, vimentin intermediate filaments protect the nucleus from excessive DNA damage and rupture (Patteson et al., 2019). However, excessive confinement can lead to nuclear blebbing and rupture and hinder migration (Mistriotis et al., 2019).

1.4.1 Modes of cell migration

Classical models of cell migration in 2D comprise of the formation of protrusions in direction of motion, attachment of this protruded region to the substrate through focal adhesions and retraction of the cell rear, almost giving the effect of a cell travelling like a wave (Fig. 1.5a).

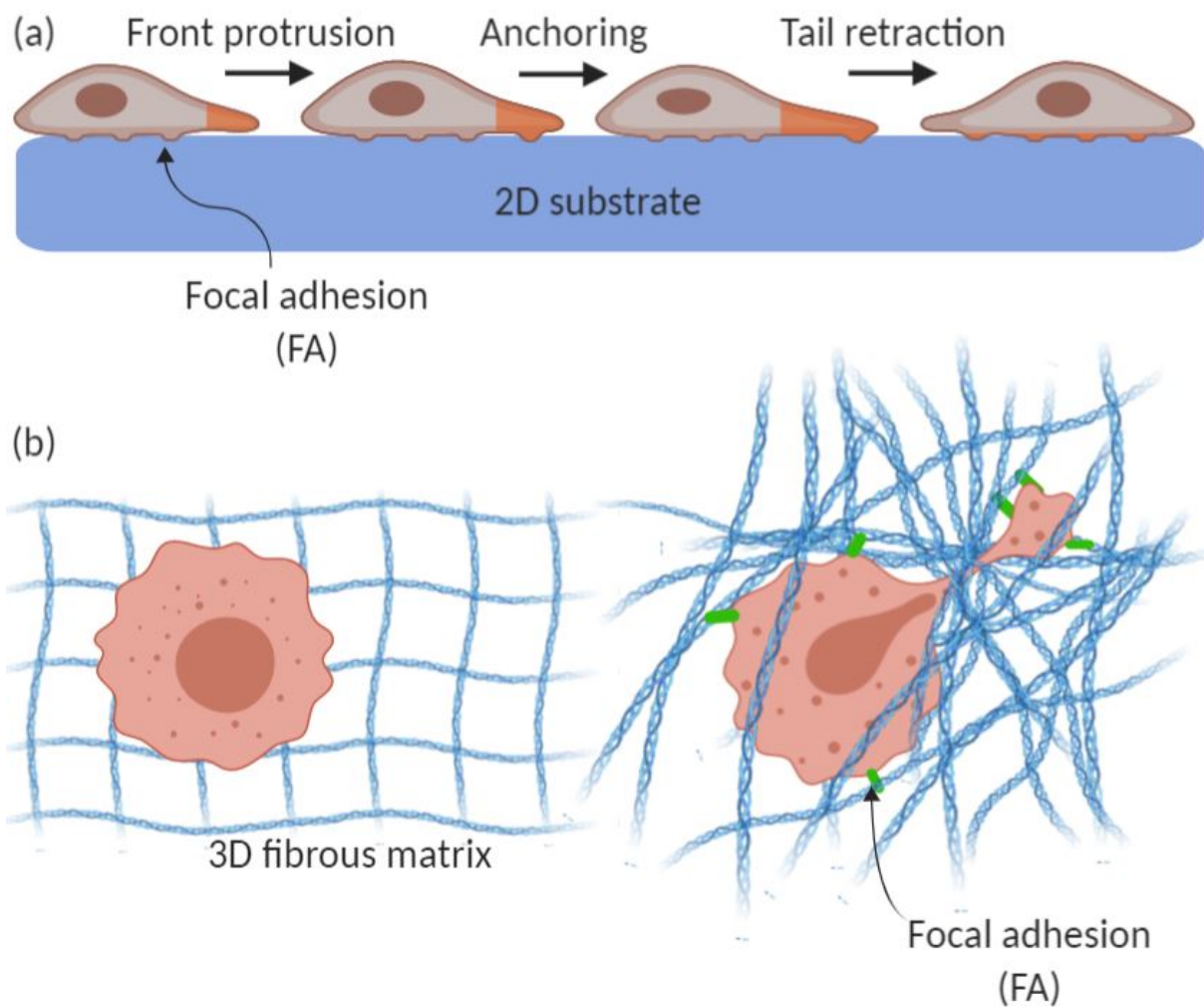


Figure 1.5: **Schematics of 2D and 3D migration.** (A) Process of protrusion and retraction of focal adhesions (FAs) required by a cell to migrate on 2D substrates. (B) 3D migration of a cell through confinement in a fibrous matrix with the help of focal adhesions (FAs) attached to matrix fibers. Created with BioRender.

These models were widely accepted even in 3D as microscopy techniques were not advanced enough to probe into cell migration in 3D matrices. The three major modes of cell migration currently known are: mesenchymal, amoeboidal and blebbing. In mesenchymal migration, cells migrate with the help of actin-rich protrusions in the direction of migration. The mesenchymal and amoeboidal modes are the two most commonly found modes of 3D migration.

Under certain conditions, it has been found that cells undergo a transition from one mode to the other in 3D. Mesenchymal mode involves migration with the help of formation of integrin-based focal adhesions on the substrate and actin-rich protrusions in the direction of migration (Fig. 1.6b). Amoeboidal mode involves rounded geometries where focal adhesions do not play

a pivotal role and cells migrate without attaching themselves to the extracellular matrix through integrin adhesions. Blebbing or lobopodial mode of cell migration is an intermediate between mesenchymal and amoeboidal modes. A cell migrates by forming blebs or rounded structures generated in the direction of migration by the asymmetric distribution of intracellular pressure. A cell is always in contact with its environment either through adhesions or friction or simply through confinement. Therefore, while focal adhesions are critical for cell motility and mechanosensation on 2D substrates or 3D fibrous matrices (Fig. 1.5b), in case of 3D non-fibrous matrices (such as through epithelial tissues), friction and confinement seem to suffice for cell movement (Paluch et al., 2016).

Several studies have been performed to understand the mechanics of cell migration by measuring degree of plasticity of the nucleus and the velocity of cells under various degrees of confinement ranging from low to extreme (Pajerowski et al., 2007; Lautscham et al., 2015). Such parameters can be systematically studied through microfluidic channels, as such channels can be manually fabricated to give the desired amount of confinement and geometry for the cells to pass through. Such microfluidic devices are fabricated using transparent polymers such as Polydimethylsiloxane (PDMS). This makes it feasible to image cell movement in 3D through microscopes or other imaging devices. These parameters would be difficult to accurately image in real time in randomly arranged 3D matrices and scaffolds such as hydrogels. When cells pass through 3D microfluidic channels, they do not form focal adhesions as they do in 2D. Thus, it has been hypothesized that cells push the channels laterally outward to propel themselves forward.

1.5 Nucleus as a Rate-Limiting Factor in Cell Migration

The nucleus is the stiffest organelle in a cell. It is stiffer than the cytoplasm and plasma membrane. The cytoplasm and plasma membrane can readily remodel themselves to squeeze through extremely small spaces, but the nucleus serves as the rate-limiting factor during cell migration through microfluidic channels or 3D matrices and scaffolds. The nucleus is intricately linked to the cytoplasm by the LINC (Linker of the Nucleoskeleton and Cytoskeleton) complex. This intricate linking ensures that forces are transmitted from the cytoskeleton to the nucleus. If

this LINC complex were to be absent or dysfunctional, then cell migration would be adversely affected, as the pulling forces generated by the cytoskeleton to pull the nucleus along with it would be absent (Graham et al., 2018). Therefore, a mechanical crosstalk exists between nuclear stiffness and contractility. Moreover, there is an increase in myosin motor density at the rear of the nucleus that is thought to help in squeezing the nucleus during 3D migration through confinement. Therefore, optimal movement of nucleus and cell requires a functional linkage between cytoplasm and nucleus and contractility and stiffening of actomyosin cytoskeleton.

The nuclear membrane that envelopes the nucleus is made up of two major proteins, Lamins A/C and B (McGregor et al., 2016). These, and Lamin A/C in particular, are responsible for maintaining the structural integrity of the nucleus and its membrane (Davidson and Lammerding, 2014). Deficiency of Lamin A/C has been associated with an increase in cell motility because the nucleus becomes softer and can squeeze through tight spaces easily (Harada et al., 2014; Denais et al., 2016; Yamada and Sixt, 2019). On the other hand, increase in nuclear stiffness caused by progerin (a mutant form of lamin A) suppresses cell migration (Booth-Gauthier et al., 2013). Additionally, the decrease in levels of Lamin B has been shown to lead to a decrease in cell migration in neurons (Coffinier et al., 2010). Here, it must also be noted that, although a decrease in lamin A/C levels leads to an increase in cell motility, several studies have shown that this may also lead to nuclear rupture and DNA damage (Raab et al., 2016; Xia et al., 2019). DNA damage in cell nuclei might even lead to tumorigenic tendencies in cells migrating through confinement (Irianto et al., 2017).

Nuclei are mechanotransducers of the cell, that is, they translate external mechanical stresses into chemical DNA signals that result in genetic changes (Navarro et al., 2016; Elosegui-Artola et al., 2017; Kirby and Lammerding, 2018). These genetic changes help the cell to react against external stresses and stimuli. A recent study (Renkawitz et al., 2019) has also demonstrated that nuclei might help a cell decide upon the path of least resistance in a confined environment that would result in the least possible DNA damage. Cell nuclei migrating under extreme confinement (through microfluidic channels and transwell pores) have been seen to form blebs and ultimately rupture to release DNA material into the cytoplasm (Raab et al., 2016; Xia et al., 2019; Mistriotis et al., 2019).

1.5.1 Biological Implications of Nuclear Rupture

Nuclear stiffness is regulated by lamins (A/C and B) and chromatin compaction (Lammerding et al., 2006; Davidson and Lammerding, 2014; Maurer and Lammerding, 2019; Stephens et al., 2019). During confined migration, the cell cytoskeleton including actomyosin, vimentin and microtubule filaments act to mechanically deform the nucleus (Stephens et al., 2017; Patteson et al., 2019). The LINC complex connecting the cytoskeleton to the nucleus helps in mechanotransduction and subsequent genetic changes in the cell (Swartz et al., 2014; Tajik et al., 2016; Irianto et al., 2017; Stephens et al., 2019).

Nuclear membrane blebbing has been generally found to precede nuclear rupture. Membrane blebs are formed due to increased intranuclear pressure under compression and lamins A/C (but not lamin B) are found to be localized in the blebs (Denais et al., 2016). When cells are compressed in confined environments, the pressure inside the nucleus becomes larger than that in the cytoplasm which is evidenced by increased nuclear membrane tension. Rupture occurs when intranuclear pressure become greater than the membrane tension of the bleb and greater than the cytoplasmic pressure. Here it must be noted that the cell nucleus has been shown to divide the cytoplasm into two compartments and regulate their intracellular pressures during 3D lobopodial migration (Petrie et al., 2014) thereby acting as a piston thereby separating the cell cytoplasm into two compartments. However, cytoplasmic pressures have not been found to increase drastically in other modes of 3D migration, such as mesenchymal or amoeboidal. Intranuclear pressure has also been found to increase due to water influx in the nucleus under confinement (Mistriotis et al., 2019). They propose that confinement activates RhoA signalling leading to an increase in myosin-dependent cortical contractility at the rear of the cell. Cellular confinement, nucleus acting as a piston and the increase in rear actomyosin contractility leads to a local cytoplasmic pressure gradient at the cell rear. This leads to a passive influx of cytoplasmic material into the nucleus through channels such as nuclear pore complexes (NPCs).

Nuclear damage and rupture have been shown to lead to changes in chromatin compaction and DNA damage. Such changes in DNA and chromatin fibers under mechanical stresses may also lead to tumorigenic tendencies in cells (Irianto et al., 2017). Nuclear membrane bleb rupture leads to the outflow of chromatin fibres into the cytoplasm. Unless the nuclear membrane rupture or damage is extreme or sustained over a long duration, it can be repaired using ESCR-

TIII machinery (Denais et al., 2016; Raab et al., 2016). However, if the membrane rupture is unrepaired, the accompanying DNA damage ultimately leads to cell death.

1.6 The Cellular Glycocalyx

A thick outer coat of sugars and proteins, beyond the cell membrane is generally found in most eukaryotic cells, called the glycocalyx. Cell adhesion and migration are modulated by the glycocalyx (also known as pericellular coat/matrix) with the former decreasing and the latter increasing with glycocalyx formation (Jones et al., 1995). This coat is such that long polymeric chains (sometimes made of $\approx 20,000$ monomeric units) act as randomly coiled springs beyond their persistence length (≈ 10 nm (Shurer et al., 2019)) and as rigid beams below it. The persistence length of such chains increases with increase in brush density N (Fig. 1.6). Such a coat has long been observed experimentally (Jones et al., 1995; Chang et al., 2016), but rarely modelled physically. Recent physical models developed shed light onto the possibility that this coat might be made of two classes of polymers, distinguished by their chain lengths (Iyer et al., 2009; Dokukin et al., 2016).

Experimental data and intensity mapping of the glycocalyx (or, pericellular matrix (PCM)) shows that it increases in thickness over time before saturating, indicating a diffusion-based growth or polymerization in the region (Chang et al., 2016). Significantly, the authors find that this swelling is not the result of polymerization of hyaluronic acid (HA), but rather due to the attachment of aggrecan molecules (forming sidechains) to the vacant sites in the HA polymeric chain. Attachment of aggrecan to HA leads to the stretching out of the HA polymer backbone due to steric hindrance thus forming a polymer brush around the cell. A thick glycocalyx can reduce cell receptor signalling and adhesion by creating large physical gaps between cell and ECM (Kuo et al., 2018). The glycocalyx also lends an effective stiffness to the cell against mechanical stresses due to its polymer brush-like architecture.

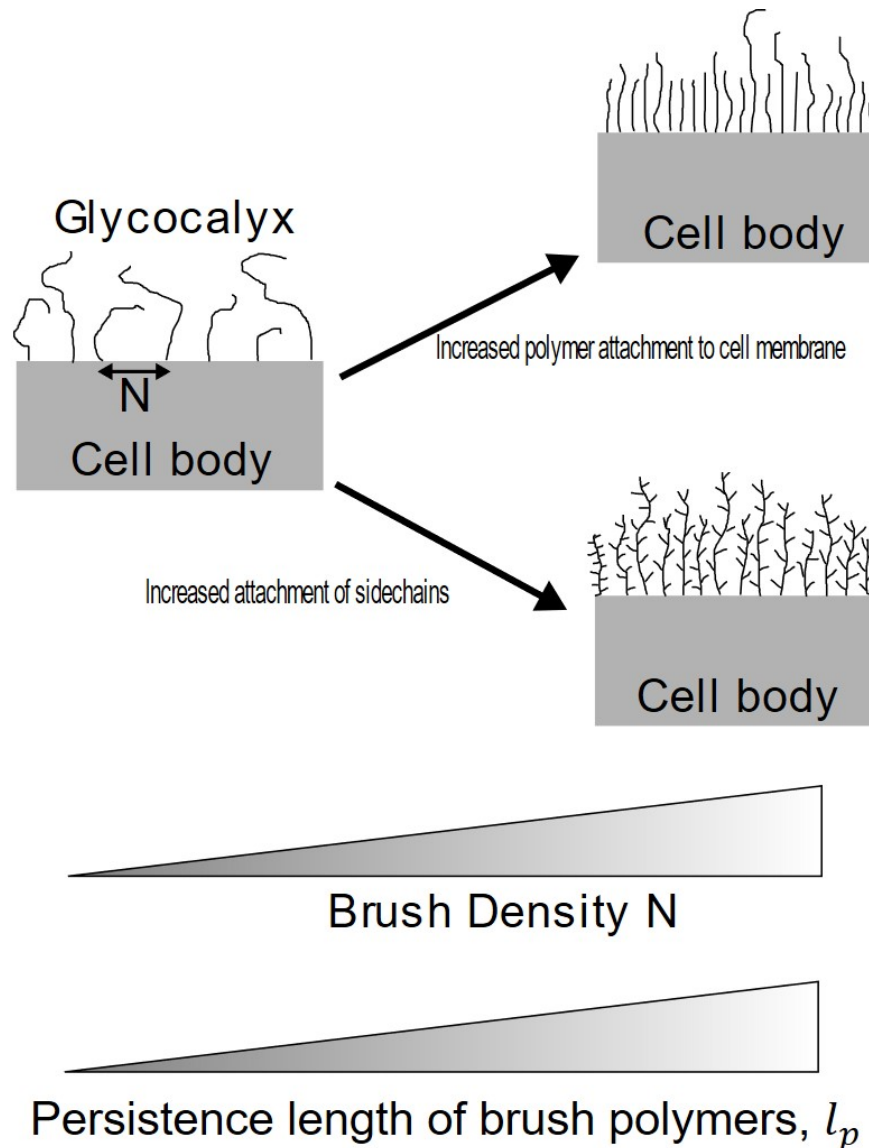


Figure 1.6: **Glycocalyx stiffness increases with increased polymer density.** Polymer density in glycocalyx attached to cell body increases either with increased polymerization and attachment of glycopolymers to cell membrane or by increased polymerization and attachment of sidechains to existing polymer backbone.

1.6.1 Formation of Glycocalyx

Glycocalyx is made of proteins and long-chain polysaccharides (large sugar molecules) (Shurer et al., 2019). Tumor cells have been found to secrete these polymers in large quantities and they are frequently found densely packed on surfaces of cancer cells (Turley et al., 2016). Cell surface receptors are embedded on the cell membrane amongst this dense network of polymer

brushes that cause steric hindrance to any molecule beyond a certain size (> 40 nm) (Chang et al., 2016; Kuo et al., 2018). This leads to alteration or regulation of receptor function by the glycocalyx polymers and might lead to developing characteristics of cancer cells by altering signalling (Paszek et al., 2014).

Glycocalyx consists of long chain linear HA or bottlebrush mucin polymers secreted by cells and attached onto the cell membrane. Synthesis of HA is effected by enzymes called synthases that regularly add HA monomers that are created in the cytoplasm on the plasma membrane by membrane receptors such as CD44 (Kuo et al., 2018). HA polymers are negatively charged and attract positively charged molecules such as protons (H^+). However, if negatively charged proteoglycans such as versicans attach themselves to the HA polymer as sidechains, the combined polymer gets stretched significantly due to the resultant electrostatic steric hindrance. Mucins are bottlebrush polymers that contain glycan (sugar molecules) sidechains along a central polymer backbone that is attached to the plasma membrane with transmembrane receptors. These sidechains also have a similar effect on increase of length of the negatively charged mucin polypeptides as HA polysaccharides with sidechains due to steric hindrance. Glycan sidechains attach to the $-OH^-$ group on the mucin polypeptide backbone and the attachment density determines the persistence length of the polymer.

1.6.2 Glycocalyx in Cancer

Some studies have suggested that the mechanical properties of the glycocalyx brush facilitates migration of cancer cells through confinement by manipulating the extracellular matrix and applying force on it (Kimata et al., 1983; Iyer et al., 2009; Chang et al., 2016; Shurer et al., 2019). The glycocalyx has also been linked to increased metastatic behaviour of cancer cells (Zhang et al., 1995). Studies also show that with the advancement of tumor stage the molecular weight of the attached glycoproteins increases, that is, they become bulky and contribute to the metastatic potential of such cells (Paszek et al., 2014). Cell signalling and invasion are altered by formation of glycocalyx. A bulky glycocalyx also serves to regulate cell-matrix adhesions via integrins and integrin clustering. Bulky and dense glycocalyx also lead to the rounding of cells and regulation of shape (Shurer et al., 2019). Cellular rounding and loss of adhesions are markers for metastasis of cancer cells and promote amoeboid migration through

confinement. Indeed, cancer cells have been shown to migrate without the requirement of adhesions, simply by pushing against the confinement walls laterally (Bergert et al., 2015) implying the mechanical as well as the chemical effects/benefits of glycocalyx in such cells.

1.7 Motivation

After developing a reasonable understanding of the available relevant literature, some lacunae/open issues have been identified for further research in this thesis. These are as follows:

- State-of-the-art experimental techniques are insufficient to quantify or visualize the intracellular or intranuclear stresses and forces.
- There is great scope of improving upon the current models of cell migration by simulating the physics involved as closely as possible.
- The mechanics underlying nuclear blebbing and rupture under confined migration and subsequent DNA damage are unclear.
- Although it is known that most of the cells in their natural environment have a thick brush-like coating of sugars, known as glycocalyx, it is unclear what its mechanical implications are.
- At the tissue scale, efficient methods of embedded tumor nodule detection for the training of surgical simulators are lacking. Accurate nodule detection is essential to treat cancers at an early stage.

1.8 Hypothesis

We hypothesize, based on our understanding of the literature and the existing open issues, that:

- Building finite element models, we can predict the intracellular stresses during cell migration in-vivo, and quantify the detectability of embedded tumours.

- Contrary to reports in the literature based mainly on micropipette aspiration implicating local increase in membrane tension for nuclear membrane rupture, we hypothesize that it occurs in-vivo under the influence of compressive stresses.
- The density and thickness of cellular glycocalyx, made up of long chain polymers, has been shown in literature to correlate with metastatic potential of cancer cells. We hypothesize that this glycocalyx layer acts as a shock absorber under external stresses and when metastatic cells migrate through confined microenvironments.

1.9 Research Objectives

In this thesis, the finite element method is used for the mechanical analysis of cell migration through confined environments, implication of glycocalyx associated with cell membrane of migrating cells and detection of material heterogeneity in the context of cancer nodules embedded in healthy tissues. Specifically, the objectives of this thesis are as follows:

1. Estimation of the evolution of intracellular and intranuclear forces and stresses during confined migration.
2. Estimation of nuclear strains and role of plasticity in confined migration.
3. Study of the mechanical implication of glycocalyx in confined migration.
4. Understanding why cancer or immune cells have greater proliferation or migration capabilities than healthy cells.
5. Prediction and creation of palpation sensitivity charts to help guide surgical simulators and robotic surgery applications to achieve greater accuracy at detecting embedded tumor nodules in healthy tissues.

These objectives are accomplished and implemented using computational methods and the results are compared with experiments. Items 1-4 are in the cellular context and item 5 is at the tissue level. Therefore, this thesis is dedicated to develop a better understanding of cancer through predictive mechanical models at the cellular and tissue levels.

1.10 Thesis Outline

This thesis is organized in the following chapters:

- ✓ Chapter-1 provides an in-depth introduction and literature review of concepts in cell migration and mechanics pertaining to cancer and links this to the mechanics of indentation and detection of material heterogeneities at the tissue level. It lays the basis for this thesis and highlights the reasons why this thesis was carried out.
- ✓ Chapter-2 describes the model used for understanding the mechanics of confined cell migration. It analyses the cellular stresses and forces involved in such migration and the implications on nuclear mechanics. It addresses an open issue of the physics of nuclear membrane blebbing and rupture during confined migration.
- ✓ Chapter-3 extends the model used in Chapter-2 to the context of glycocalyx-mediated cell-ECM mechanical interplay. It analyses the mechanical effect the glycocalyx has on cellular stresses and ECM deformation and explores why it might be necessary/beneficial in metastatic cancer cells under external stresses.
- ✓ Chapter-4 probes the mechanics of cancerous tumors at the tissue level. It explores the efficiency of palpation techniques using non-dimensional analysis to detect tumors embedded in healthy tissues.
- ✓ Chapter-5 summarizes the findings of this thesis and lays the foundation for possible future work.
- ✓ Chapter-6 enumerates the scientific contributions resulting from this work in the form of publications and conference abstracts.

This page was intentionally left blank.

Chapter 2

Modelling of confined cell migration

Note: This chapter has been modified from the following published article: Mukherjee A, Barai A, Singh R K, Yan W, Sen S, "Nuclear Plasticity Increases Susceptibility to Damage During Confined Migration", *PLoS Computational Biology*, 16(10): e1008300.

2.1 Introduction

Cells transit through a myriad of environments, ranging from 2D basement membranes (BM) to 3D collagen networks for morphogenesis, division and proliferation, wound healing and cancer invasion (Alexander et al., 2013). Cells sense their surrounding mechanical environment and transit through a pore that poses the least mechanical resistance, a process intrinsically linked to their chances of survival (Renkawitz et al., 2019). PDMS devices, widely used for studying confined migration, are significantly stiffer (\approx MPa) than soft tissues (\approx kPa) *in vivo*, thus failing to recapitulate the interplay of nucleus and tissue properties that likely dictates the dynamics of confined migration. The importance of nuclear properties, namely stiffness, in regulating the efficiency of confined migration, is well appreciated. While physical properties of the nucleus are dictated by expression of the intermediate filament protein Lamin (A/C and B) (Lammerding et al., 2006; Davidson and Lammerding, 2014; Maurer and Lammerding, 2019) and its phosphorylation (Das et al., 2019; Buxboim et al., 2014), nuclear deformation is mediated by the actomyosin and the microtubule cytoskeleton which are physically coupled to the nucleus via nesprins (Yeung et al., 2005; Roux et al., 2009). Additionally, localized cytoplasmic stiffening at sites of increased stress from the external environment (De et al., 2007; Zemel et al., 2010; Kim et al., 2017), might facilitate nuclear compression thereby aiding in confined migration.

Computational modeling of cell migration has primarily been achieved either by idealiz-

ing them as solid continuum spring/spring-dashpot models (Guilak et al., 1999; Zhou et al., 2005; Cao et al., 2016) or as liquid droplets bounded by deformable membranes (Liu et al., 2006; Moure and Gomez, 2017). These assumptions are reasonable in light of a cell being biphasic, exhibiting solid-like behaviour in certain situations and liquid-like character in others. However, both of these types of models have their limitations; whereas solid continuum models are unable to replicate similar levels of extreme cellular deformation that occurs in-vivo, liquid droplet models are unable to quantify intracellular stresses. Appropriate visualization of the evolution of stresses within cellular structures such as the actin cytoskeleton and nucleus is critical to complement experimental observations. The current state-of-the-art experimental procedures are unable to predict the stresses that the nucleus undergoes while migrating through 3D confined environments. Traction force microscopy that calculates the stress on the surface of a substrate by relating the deformation of that surface to the stress using Hooke's law is a critical tool for visualizing mechanical interaction between a cell and its environment (Aung et al., 2014), but is limited by its inability to quantify intracellular stresses.

Extreme nuclear deformations during migration through $3\ \mu\text{m}$ transwell pores have been shown to cause plastic deformation (Raab et al., 2016; Deviri et al., 2019) as well as nuclear membrane rupture (Denais et al., 2016; Le Berre et al., 2012; Xia et al., 2019). Whether or not nuclear plasticity and nuclear damage are inter-related remains unknown. Also, the extent to which tissue properties influence the plastic deformation of the nucleus has not been probed. For probing nuclear deformation and deformation-induced damage, here we have developed a plane strain finite element model to simulate confined cell migration through a tissue-mimetic environment where mechanical properties of the cell and nucleus have been considered. Studying the collective influence of nuclear and tissue stiffness on the dynamics of pore migration, our results predict the magnitude of cellular force required to squeeze through a constriction and the intracellular stresses sustained by the cell. Our results predict that stiff nuclei passing through stiffer tissues undergo plastic deformations leading to nuclear membrane bending, which may be the cause of nuclear rupture documented experimentally. We validate these predictions using experiments wherein nuclear stiffening led to plastic deformation of the nucleus and higher DNA damage. In addition to predicting a scaling relationship between the timescales and force-scales associated with pore entry, our results establish a direct link between nuclear plasticity and nuclear damage during constricted migration.

2.2 Viscoelasticity of cell and extracellular matrix (ECM)

Cell membrane (plasma membrane) and nuclear membrane are lipid bilayers that are dotted with various protein complexes and ion channels that allow for the transmigration of molecules. In a coarse-grained scenario, the cell membrane can be considered to be composed of a combination of a lipid bilayer, glycocalyx (polymer chains of glycolipids and glycoproteins (Shurer et al., 2019)) and the actin cytoskeleton meshwork attached to the lipid bilayer. This composite cell membrane behaves as a viscoelastic material that flows like a viscous liquid over short timescales but exhibits a solid-like elastic behaviour at sufficiently long timescales. This leads to the experimental observation of cells attaching themselves onto 2D substrates forming stable shapes (Desprat et al., 2005; Hoffman et al., 2006; Kasza et al., 2007). A similar argument can be extended for the choice of the nuclear membrane and nuclear lamina composite as a viscoelastic material due to the similarities in their intrinsic composition with cell membrane and cytoskeleton respectively.

Considering the cell as a closed system consisting of a fibrous mixture (actin cytoskeleton, actomyosin fibres, microtubules and intermediate filaments) and a solvent (cytosol) with no net transport of molecules through the cell membrane, we model it as viscoelastic solid as opposed to poroelastic that assumes a net flux of solvent molecules. The tissue(s) through which the cell migrates is/are also considered as viscoelastic solids because we consider them to be individually closed systems which if stressed, lead to solvent molecules in the vicinity of the stressed region to get displaced from their initial locations temporarily before returning to their original position after stress is relieved. These assumptions are consistent with several experimental studies have demonstrated the viscoelastic nature of cells and tissues.

2.2.1 Viscoelasticity formulation in the time-domain

To describe the constitutive relationship governing an isotropic viscoelastic material, we define the deviatoric and volumetric parts of the stress tensor. For the time-dependent deviatoric stress,

time-varying shear strain $\varepsilon_{dev}(t)$ and shear stress $\sigma_{dev}(t)$ are related as:

$$\sigma_{dev}(t) = G_0 \int_0^t g_R(t-s) \dot{\varepsilon}_{dev}(s) ds \quad (2.1)$$

where G_0 is the instantaneous shear modulus and $g_R(t) = G_R(t)/G_0$ is the dimensionless time-dependent shear relaxation modulus of the viscoelastic material. The time-dependent volumetric behaviour (σ_{vol}) of the material is defined as a change in hydrostatic pressure ($p(t)$) over time and is given by the equation:

$$\sigma_{vol}(t) = p(t) = -K_0 \int_0^t k_R(t-s) \dot{\varepsilon}_{vol}(s) ds \quad (2.2)$$

where K_0 is the instantaneous bulk modulus and $k_R(t) = K_R(t)/K_0$ is the dimensionless time-dependent bulk relaxation modulus of the viscoelastic material. The instantaneous moduli G_0 and K_0 are related to the Young's modulus E_0 and Poisson's ratio ν as $G_0 = E_0/2(1 + \nu)$ and $K_0 = E_0/3(1 - 2\nu)$ respectively. A viscoelastic material is defined by a Prony series expansion of the dimensionless relaxation modulus given by the equation:

$$g_R(t) = 1 - \sum_{i=1}^N g_i^P (1 - \exp^{-t/\tau_i^G}) \quad (2.3)$$

where N , g_i^P and τ_i^G , $i = 1, 2, \dots, N$, are material constants. The shear stress then is given by:

$$\sigma_{dev}(t) = G_0 \left(\varepsilon_{dev} - \sum_{i=1}^N \varepsilon_i \right) \quad (2.4)$$

where $\varepsilon_i = \frac{g_i^P}{\tau_i^G} \int_0^t \exp^{-s/\tau_i^G} \varepsilon_{dev}(t-s) ds$. A similar expression can be acquired for the volumetric response, as shown below:

$$\sigma_{vol}(t) = p(t) = -K_0 \left(\varepsilon_{vol} - \sum_{i=1}^N \varepsilon_i \right) \quad (2.5)$$

where, $\varepsilon_i = \frac{k_i^P}{\tau_i^K} \int_0^t \exp^{-s/\tau_i^K} \varepsilon_{vol}(t-s) ds$.

2.3 Plasticity of the nucleus

Previous studies have demonstrated that stressed nuclei undergo plastic deformation, i.e., they are irreversibly deformed under the application of stresses (Pajerowski et al., 2007; Tocco et al., 2018). Plastic deformation in non-fibrous biological materials arise due to irreversible dislocation or dislodgement of molecules from their unperturbed positions. In fibrous biological materials like collagen, plasticity under tensile strains is caused due to un-entanglement of fibers (Kim et al., 2017). Plasticity is generally quantified as a strain or stress regime that extends beyond a critical threshold elastic limit below which molecular dislocations are reversible. An elastic material is assumed to have a linear stress-strain curve within a threshold termed as the proportional limit, beyond which the slope of the curve changes and the relation may become nonlinear. Plastic deformation leads to energy dissipation and therefore, the onset of plasticity signifies a new stable energy state for the material from the previous metastable strained state. Plasticity induced nuclear damage and rupture due to extreme stresses originating under confinement, for instance, may lead to genetic perturbation (Raab et al., 2016; Xia et al., 2019).

2.4 Cytoskeletal strain stiffening

Actin bundling proteins (ABPs) get attached to actin filaments with increasing stresses in the cytoplasm (Gardel et al., 2004a,b). Moreover, actin filaments frequently bundle together in a direction perpendicular to the direction of application of external force. These mechanisms contribute to the eventual stiffening of actomyosin networks. Studies indicate that depending on the actin concentration and crosslinking density the stiffness of such crosslinked fibres can change drastically (Gardel et al., 2004a,b, 2008). In our model, using the ABAQUS/Explicit subroutine VUSDFLD, we implemented this experimental observation such that if the cytoplasmic shear stress increased beyond 20 kPa, the cytoplasmic shear stiffness was increased in discrete steps from 1.0001 Pa to 1.1 Pa, and the system re-equilibrated.

2.5 Methods

2.5.1 Computational Methods

For studying dynamics of confined cell migration, a plane strain finite element (FE) model of the system was created in ABAQUS/Explicit. FE models involve discretizing the system into smaller elements by meshing it (dividing the system into several discrete polygonal elements/parts). Numerical techniques (explicit central-difference time integration rule) are then used to arrive at an approximate solution to the equation of motion of the general form $[M]\{\ddot{u}\} = \{P\} - \{I\}$. This is a general equation for dynamic equilibrium with the lumped mass matrix $[M]$, acceleration vector $\{\ddot{u}\}$, and $\{P\}$ and $\{I\}$ denoting external and internal force vectors respectively. This equation is computed at each node of each polygonal element that the object is made of. Discontinuities resulting due to cellular organelles and granular structures at the nanoscale are homogenized and considered as a continuum at the microscale. The explicit dynamics procedure of ABAQUS involves performing a large number of small time increments. Where a stable time increment is denoted by Δt , accelerations at time t are used to advance velocity solutions to $t + \Delta t/2$ and displacement solutions to $t + \Delta t$. The accelerations at time t are calculated by solving the equation of motion for an increment number i as:

$$\ddot{u}_i = M^{-1}(P_i - I_i)$$

This can then be used in:

$$\dot{u}_{i+1/2} = \dot{u}_{i-1/2} + \frac{\Delta t_{i+1} + \Delta t_i}{2} \ddot{u}_i$$

$$u_{i+1} = u_i + \Delta t_{i+1} \dot{u}_{i+1/2}$$

A computational domain needs to be selected for numerical simulations in FEM so that boundary conditions (BCs) are applied to the PDEs that are solved as part of the problem. Since

our desired direction of cell migration is the $+x$ -direction in the Cartesian coordinate system as shown in Fig. 2.1B, we assume that the deformation or volume change of the cell perpendicular to the plane of migration (xy -plane) would be much lower than that in plane and hence can be neglected. This is complemented by our chosen material parameters of all system components where the Poisson's ratio (ν) is 0.3 indicating that all the materials are slightly compressible (Table 2.2), that is, a change in area in the xy -plane does not accompany a similar change in the yz - or xz -planes. This assumption finds credibility in experimental observations of cell migration through microchannels where the cell deforms or gets polarized in the direction of migration but the accompanying lateral deformation is negligible (Stroka et al., 2014; Thiam et al., 2016). This study models a situation where a cell migrates through a confined pore or channel. In such confined channels (in-vivo or microfluidic channels), the cell fills up the channel cross-section area and is therefore constrained in the directions perpendicular to the direction of migration. In this study, the cell migration is assumed to occur in the xy -plane and hence, strains occur in the xy -plane. Therefore, we consider no-strain boundary conditions in the xz - and yz - planes. However, stress is non-zero in these lateral directions as the cell pushes against the channel walls, and hence, we use a 2D plane strain and not a 2D plane stress condition.

In our formulation, entry of a $10\ \mu\text{m}$ diameter cell with a 5 or $6\ \mu\text{m}$ diameter (D_0) nucleus into a pore ($\phi = \{3, 5\}\ \mu\text{m}$ diameter) at the interface of two tissues was simulated with the system assumed to be in a quasi-static state for the entire duration of the simulation (Fig. 2.1A, B). This was verified by observing the kinetic energy of the entire system to be much lower than its internal energy. The internal energy of the system is the sum of the elastic strain energy of the system, the energy dissipated due to plastic deformation, and the energy dissipated due to viscoelastic deformation. Pore entry was mediated by active protrusive forces (F_p) generated by the cell at the cell front as shown in Fig. 2.1 and as proposed in experiments (Smith et al., 2007; Friedl and Wolf, 2010). Loads varying between 0 and $2.5\ \text{pN}$ were individually applied to ≈ 260 nodes in the region shown in Fig. 2.1. A comparison of the salient features of two other FE models (Cao et al., 2016; Zhu and Mogilner, 2016) with our model is presented in Table 2.1. Here, 'Y' denotes the presence of a feature whereas, 'N' denotes its absence. While this list is not exhaustive, it lists some of the mechanically and physically critical features that aid in cell migration in 3D matrices.

Table 2.1: **Comparison with other FE-based cell migration models**

Model Feature	Zhu and Mogilner (Zhu and Mogilner, 2016)	Cao et. al. (Cao et al., 2016)	Current Study
Consideration of cytoskeleton	Y	N	Y
Cytoskeletal stiffening	N	N	Y
Nuclear Plasticity	N	Y	Y
Viscoelastic cellular components	N	N	Y
Viscoelastic gel/tissue/ECM	N	N	Y

The cell is composed of the following components: cell membrane, cytoplasm, nuclear membrane and nucleus. All the components except the nucleus are approximated as Kelvin-Voigt viscoelastic elements (Fung, 1993) where stress (σ) developed in a system depends on the strain (ϵ) and strain rate ($\dot{\epsilon}$) and is given by the equation $\sigma = K\epsilon + \eta\dot{\epsilon}$. Here, K is an elasticity modulus that corresponds to spring or solid stiffness and η is viscosity of the constituent fluid. The viscoelastic character of each component in the system is represented in the form of normalized creep compliance (Fig. 2.3A). Creep is a characteristic feature of a viscoelastic material that defines the amount by which a system deforms under persistent stress. Compliance is the reciprocal of stiffness (Pa) and is a measure of the ease with which a body deforms under stress.

The nucleus is considered to be elastoplastic with its behaviour described by a strain hardening power law equation $\sigma_{yield} = a + b\epsilon_{plastic}^n$, similar to Ludwik's equation (Ludwik, 1909). The plastic strain is denoted by $\epsilon_{plastic}$. The coefficients a, b and the exponent n were estimated

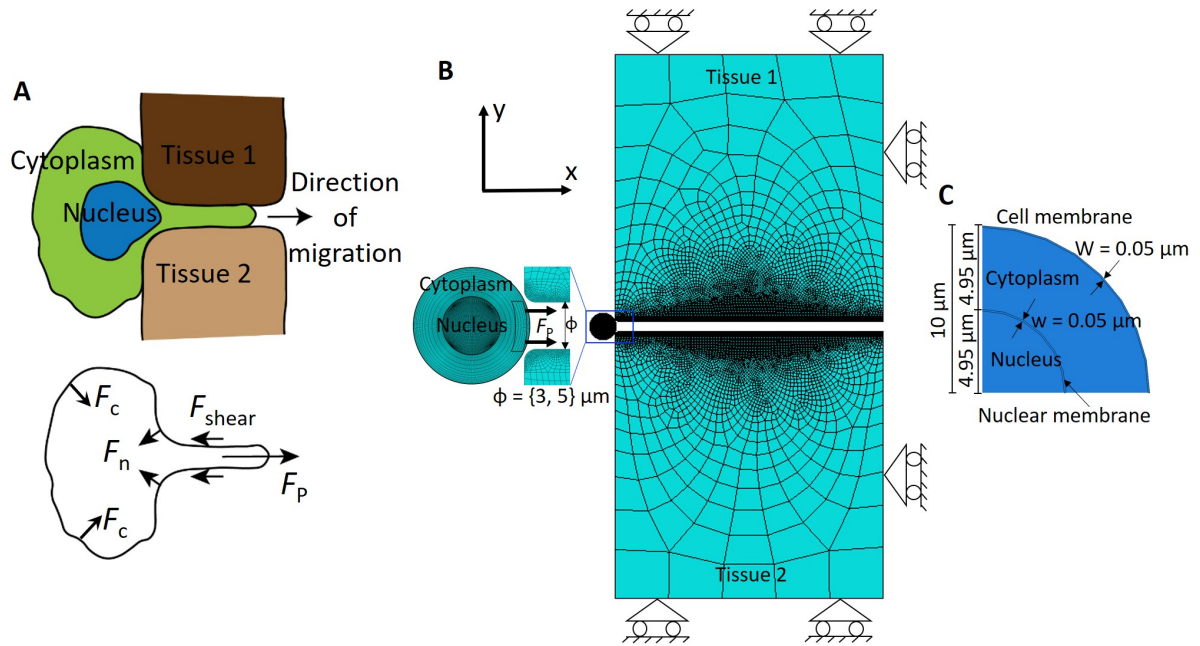


Figure 2.1: **Model definition.** (A) Schematic of the simulated problem. (B) Finite element model with mesh. Lateral and transverse boundaries of the tissue (1 and 2) are constrained in their perpendicular directions. (C) Dimensions of various parts of the modelled cell (only 1/4th of the cell is shown due to symmetry).

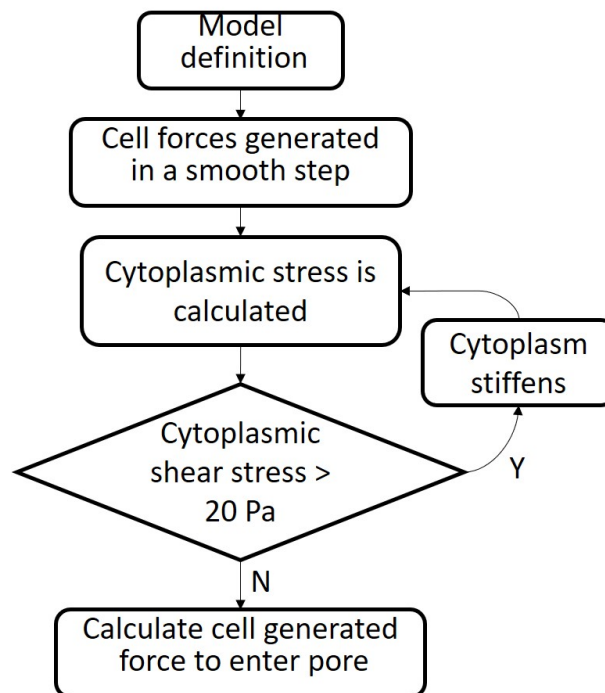


Figure 2.2: **Model process flow.**

to be equal to 41 Pa, 17 Pa and 2.89 respectively ($R^2 = 0.9981$), with data trend similar to those

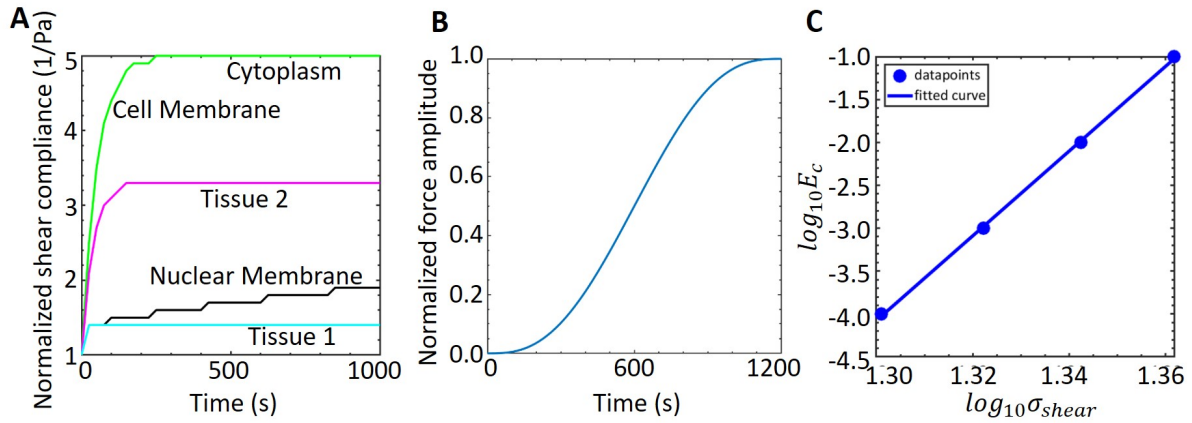


Figure 2.3: **Material parameters used in the model.** (A) Viscoelastic properties of various materials in the model. (B) Temporal variation of input force. (C) Assumed dependence of cytoplasmic stiffness (E_c) with shear stress (σ_{shear}) encountered by the cell. E_c is increased in discrete steps as indicated by datapoints and a smooth curve is interpolated, i.e., the points are used to define a function between the two variables.

reported by Pajeroski et al. (2007). The total strain in the system is the sum of both elastic and plastic strains ($\epsilon_{total} = \epsilon_{elastic} + \epsilon_{plastic}$). Yield stress (σ_{yield}) is defined as the stress at which a substance develops permanent plastic deformation. When there is no plastic strain in the nucleus (i.e., nucleus deforms elastically), $\sigma = a = \sigma_{yield}$. When $\sigma < \sigma_{yield}$, then $\sigma = E\epsilon_{elastic}$, where, $\epsilon_{elastic} < \sigma_{yield}/E$. Plastic strain $\epsilon_{plastic}$ is given by: $\epsilon_{plastic} \geq \sigma_{yield}/E$. In a strain hardening material, the yield stress increases with strain, thus implying that it becomes progressively difficult to strain the material.

The elastic properties of the nucleus arise from the lamin network below the nuclear membrane along with chromatin fibres. Plastic nature of nuclei have been reported in several studies demonstrating the irreversible change in shape of nuclei deformed under stress (Pajeroski et al., 2007; Stephens et al., 2017; Tocco et al., 2018). A recent study (Stephens et al., 2017) also demonstrated that nuclei stiffen progressively with strain, a phenomenon attributed to chromatin compaction at small strains and to Lamin A/C at large strains. Plastic deformation in non-fibrous biological materials arise due to irreversible dislocation or dislodgement of molecules from their unperturbed positions. In fibrous biological materials like collagen, plasticity under tensile strains is caused due to unentanglement of fibers (Kim et al., 2017). The tissues representing the two sides of the interface are also modelled to be viscoelastic. A Poisson's ratio of $\nu = 0.3$ which is a typical value considered for compressible biomaterials (Cao et al., 2016),

was chosen for the cellular components as well as the two tissues. This value also sits well with our assumption that the out-of-plane volume change is negligible compared to the in-plane deformation. All elastic material properties are listed in Table 2.2.

Table 2.2: **Material parameters**

Component	Density (ρ) (kg/m ³)	Young's Modulus (E) (kPa)	Poisson's ratio (ν)	Undeformed thickness (μ m)	Reference
Cell Membrane	1050	0.3	0.3	0.05	
Cytoplasm	1030	0.001	0.3	4.95	(Guo et al., 2013)
Nuclear Membrane	1800	0.2 - 5	0.3	0.05	(Dahl et al., 2005)
Nucleus	1800	0.2 - 5	0.3	9.9	(Dahl et al., 2005; Stephens et al., 2017)
Tissue 1, 2	1500	0.13 - 5	0.3	100	(George et al., 2018)

Cells are known to exert forces by actomyosin contraction resulting from myosin motors sliding on actin filaments (De et al., 2007; Zemel et al., 2010). During migration, cells regulate F-actin polymerization and generate protrusions (Stricker et al., 2010), leading to an increase in force generated. Crosslinking of actin filaments with proteins such as α -actinin, filamin and scruin stiffens these fibers and they bundle together to generate protrusive forces. Myosin II plays an important role in creation and regulation of stress fibers and force generation (Peterson et al., 2004; Stricker et al., 2010). To mimic these phenomena in our model, we assumed that the cell generates force (F_P) at the leading edge in the direction of motion (x-axis) in a smooth monotonic fashion (Fig. 2.3B). F_P was assumed to be generated in a dis-

tributed fashion at the cell front as shown in Fig. 2.3B such that the magnitude of the maximum force (≈ 6.4 nN) generated by the cell remained in the physiologically relevant range (Rabodzey et al., 2008; Neelam et al., 2015). Cytoskeletal stress stiffening was implemented in our model using the ABAQUS/Explicit subroutine VUSDFLD (see Supplementary Information and Figs. 2.2 and 2.3C). In each time increment, the model algorithm checks if the cytoplasmic shear stress increased beyond 20 kPa, the cytoplasmic shear stiffness was increased in discrete steps from 1.0001 Pa to 1.1 Pa, and the system re-equilibrated (Fig. S1e, Fig. S3) (Gardel et al., 2004a,b; Licup et al., 2015). This variation can be curve-fit as per the equation $\log_{10}(E - 1) = 49.41 \log_{10}\sigma_{shear} - 68.31$, where E and σ_{shear} represent cytoplasmic stiffness and shear stress, respectively. The simulation was stopped once the nucleus enters the pore completely.

An explicit formulation was implemented to successfully resolve large nonlinear deformations in meshes in the Lagrangian or material domain. In this energy-based formulation, the stable time increment (Δt) to solve the numerical problem depends on the stress wave velocity through the smallest element in the mesh ($\Delta t \approx L_{min}/c_d$), where L_{min} is the smallest element dimension in the mesh and c_d is the dilatational wave speed through the element. Mass scaling was used to ensure that Δt was of the order $O(-4)$. Frictionless hard contact was assumed at the cell-gel interface to simulate non-adherence of cell to the gel or channel walls. The cell surface was thus allowed to separate after contact with the gel surface. For the cases of $D_0/\phi = 1$ and 1.67, a total of 31183 bilinear plane strain CPE4R elements were used in the model, of which the two tissues were composed of 7469 and 7366 elements and the cell was composed of 16348 elements. For the case of $D_0/\phi = 1.2$, while the two tissues had the same number of elements as mentioned above, the cell was composed of 15870 elements, leading to a total of 30705 CPE4R elements in the model. A mesh sensitivity analysis was done on the nuclear membrane and the cell membrane to arrive at the optimal mesh element dimensions to minimize mesh distortion. The optimal minimum element dimension was found to be $0.005 \mu\text{m}$ and the maximum was $20 \mu\text{m}$. The mesh size was modulated so as to be fine in the regions that were expected to come in contact or that would undergo large deformation. The nuclear membrane as well as the cell membrane, $0.05 \mu\text{m}$ in thickness, had 10 elements in the through-thickness direction to mitigate the effects of excess artificial bending stiffness of the membranes. This value for the optimum number of elements was arrived at using mesh sensitivity analysis. Additionally, a distortion control algorithm in-built in ABAQUS was used to counter mesh distortions (prevent element

inversion and excessive distortion) when minimum to maximum dimension ratio of a mesh element decreased below 0.1. This was done to ensure that the kink in the nuclear membrane observed in our results is not a numerical artifact of the FEM simulation.

2.5.2 Experimental Methods

Cell culture and reagents:

HT-1080 fibrosarcoma cells obtained from National Center for Cell Science (NCCS) (Pune, India), were cultured in DMEM (high glucose, Invitrogen) containing 10% FBS (Hi-media). For nuclear stiffness experiments, cells were plated sparsely on glass coverslips coated with rat-tail collagen I (Cat # 3867, Sigma) at a coating density of $10 \mu\text{g}/\text{cm}^2$. Cells were incubated with DMSO (i.e., vehicle), $1 \mu\text{M}$ blebbistatin (Cat # B0560, Sigma) or $10 \mu\text{M}$ RO-3306 (Cat # ab141491, Abcam) for 12 hours prior to probing with AFM.

Atomic Force Microscopy (AFM) and Imaging:

For measuring nuclear stiffness, stiff tips (32 kHz, TR400PB, Asylum Research) with nominal stiffness of 120 pN/nm were used, with exact values of cantilever stiffness determined using thermal calibration method. Cells were indented towards the center right on top of the nucleus, and indentation data more than 2000 nm were fitted with Hertz model to obtain estimates of nuclear stiffness.

For transwell migration studies, 10^5 cells were seeded on the upper chamber of 24 well plate cell culture inserts containing $3 \mu\text{m}$ pores (Cat # 353096, Merck). The inserts were coated with rat-tail collagen I. For creating a gradient, the upper chambers were filled with plain DMEM supplemented with drugs and the lower chambers filled with DMEM containing 20% FBS. After 8, 18 and 28 hrs, cells were fixed with 4% PFA and then stained with DAPI for 45 minutes. After washing with PBS, membrane was cut and mounted on a glass slide using mounting media. Confocal z-stack images were acquired at 20x magnification using Scanning Probe Confocal Microscope (Zeiss, LSM 780) at identical exposure and gain settings. Images analysis and quantification was performed using Fiji-Image J software. Translocation efficiency

was calculated using the equation $\frac{N_b}{N_t+N_b} \times 100$ where N_t and N_b represent the number of DAPI-stained nuclei on the top and bottom surfaces of the membrane per frame.

For γ H2Ax and Lamin A/C staining, fixed cells were permeabilized with 0.1% Triton-X 100 for 8-10 mins, blocked with 2% bovine serum albumin (BSA) for 1 hr at room temperature, and then incubated with γ H2Ax rabbit monoclonal antibody (Cat # 9718S, CST) and anti-Lamin A/C mouse monoclonal antibody (Abcam, Cat # ab8984) overnight at 4° C. The following day, after washing with PBS, Alexa-Fluor 488 anti-rabbit IgG and Anti-Mouse Alexa fluor 555 was added for 2 hr at room temperature. Nuclei were stained with DAPI for 5 min at room temperature. Images were acquired at 40x magnification using Scanning Probe Confocal Microscope (Zeiss, LSM 780) at identical exposure and gain setting.

2.6 Results

2.6.1 Nuclear and tissue properties collectively dictate dynamics of confined migration

The nucleus which is the largest and stiffest organelle inside the cell, is physically connected to the cytoskeleton through the LINC complex McGregor et al. (2016). Consequently, compression of the cell during confined migration is associated with compression of the nucleus with the extent of cytoplasmic/nuclear deformations dictated by their mechanical properties in relation to that of the surrounding tissues. For studying dynamics of confined migration, a finite element model was developed wherein physical properties of cell membrane, cell cytoplasm, and nucleus were taken into account. Consistent with experiments, the cell membrane, cell cytoplasm and nuclear membrane were modeled as viscoelastic Kelvin-Voigt materials (Fig. 2.1-2.3; refer to Computational Methods section for details) Desprat et al. (2005); Hoffman et al. (2006); Kasza et al. (2007). A similar viscoelastic description was also used in modeling tissue behavior Chaudhuri (2017). Furthermore, consistent with stress-induced permanent deformation of the nucleus, an elastoplastic behavior was assumed for the nucleus Pajeroski et al. (2007); Tocco et al. (2018). Finally, cytoskeletal strain stiffening behavior observed with reconstituted

cytoskeletal networks was also accounted for Gardel et al. (2004a,b, 2008).

In our model, cell migration through pores in tissues was assumed to be frictionless and mediated by protrusive forces (F_p) exerted at the leading edge, with E_1 and E_2 representing the Young's moduli (stiffness) of Tissue 1 and Tissue 2, respectively (Fig. 2.1A, B). Simulation with $E_1 = E_2$ correspond to a situation wherein a cell squeezes through a pore in a given tissue/hydrogel. In comparison, $E_1 \neq E_2$ corresponds to a cell migrating at the interface of two distinct tissues/hydrogels (Rape and Kumar, 2014; George et al., 2018). To first probe the effect of nuclear size on migration efficiency, simulations were performed wherein dynamics of cell entry into a pore of given size (i.e., $\phi = \{3, 5\} \mu\text{m}$) was tracked for different sizes of nucleus (i.e., $D_0 = 5$ and $6 \mu\text{m}$) and for varying tissue stiffness (i.e., $E_T : (0.13 - 5) \text{ kPa}$) (Fig. 2.4A). In these simulations, nuclear stiffness was kept constant at $E_n = 1 \text{ kPa}$. For entry into a pore within the same tissue, i.e., $E_T = E_1 = E_2$, the time for pore entry (T_{entry}) as well as the maximum force required for pore entry (F_{entry}) remained unchanged irrespective of E_T when the nucleus was smaller or equal to the pore size (i.e., $D_0/\phi \leq 1$) (Fig. 2.4B). However, both these quantities increased with increase in E_T for $D_0/\phi > 1$, highlighting the role of the nucleus in regulating confined migration. When $E_1 \neq E_2$, T_{entry} and F_{entry} were comparable to values corresponding to the higher tissue stiffness (Fig. 2.5A-C).

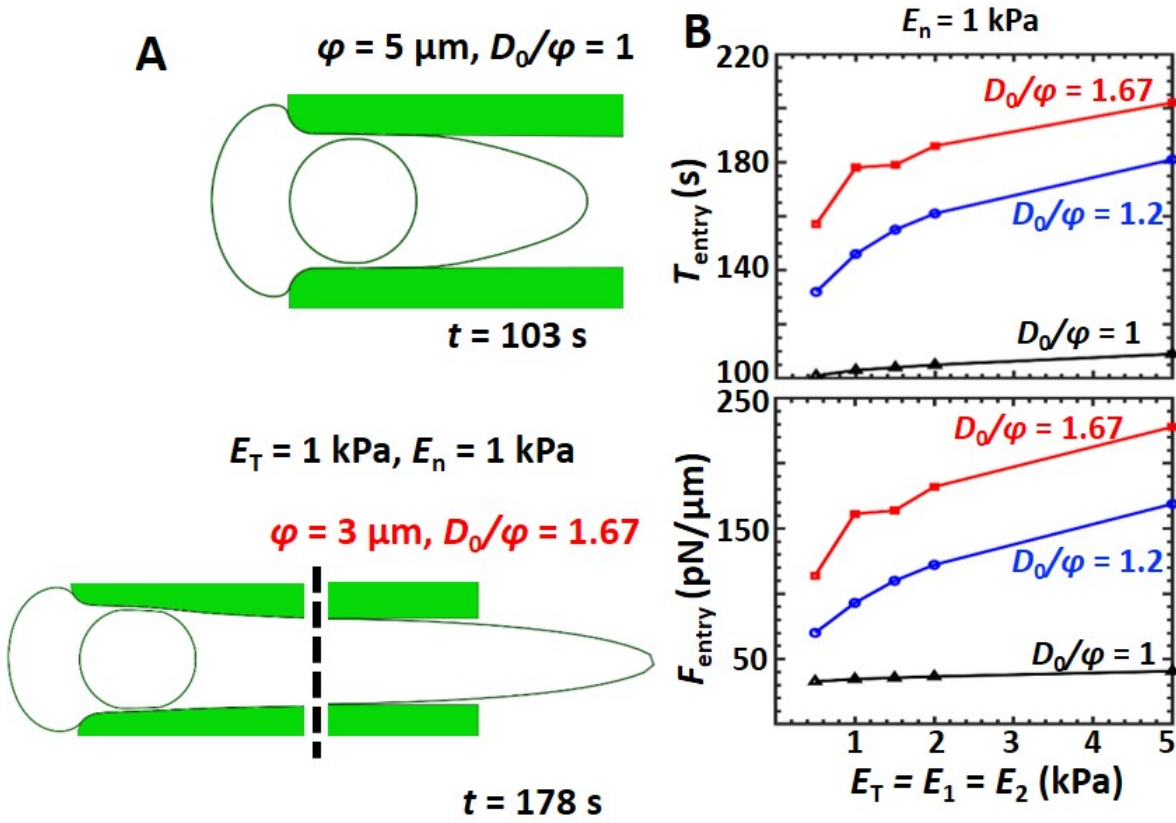


Figure 2.4: **Interplay of nuclear and tissue stiffness on dynamics of pore entry for migration through homogeneous tissue.** (A) Cellular deformation just after entry into pore for different extents of degree of confinement (D_0/ϕ). E_c was increased from an initial value of 1 Pa to a possible maximum of 1.1 Pa under shear-induced cytoskeletal stiffening and E_n was assumed to be 1 kPa. (B) Force (F_{entry}) and time (T_{entry}) required for a cell (with $E_n = 1 \text{ kPa}$) to enter a pore of given size and their dependence on tissue stiffness ($E_T = E_1 = E_2$) and D_0/ϕ .

Entry into small pores ($D_0/\phi = 1.67$) was mediated by widening of the pores as evident from the vertical displacement of the tissues in a E_n -dependent manner (Fig. 2.6A). While displacements far from the pore entry decayed to zero in most cases, for the case corresponding to $E_T = 2 \text{ kPa}, E_n = 1 \text{ kPa}$, vertical displacement of the tissue was non-zero even at distances far from the entry point. The maximum vertical tissue displacement exhibited a non-monotonic dependence on E_n/E_T with lowest displacement corresponding to $E_T = 2 \text{ kPa}, E_n = 1 \text{ kPa}$ where non-zero displacements were observed far from the entry point (Fig. 2.6B). Together, these results suggest that pore migration through deformable matrices is collectively dictated by nucleus and tissue properties with entry time-scales and force-scales strongly coupled to each other.

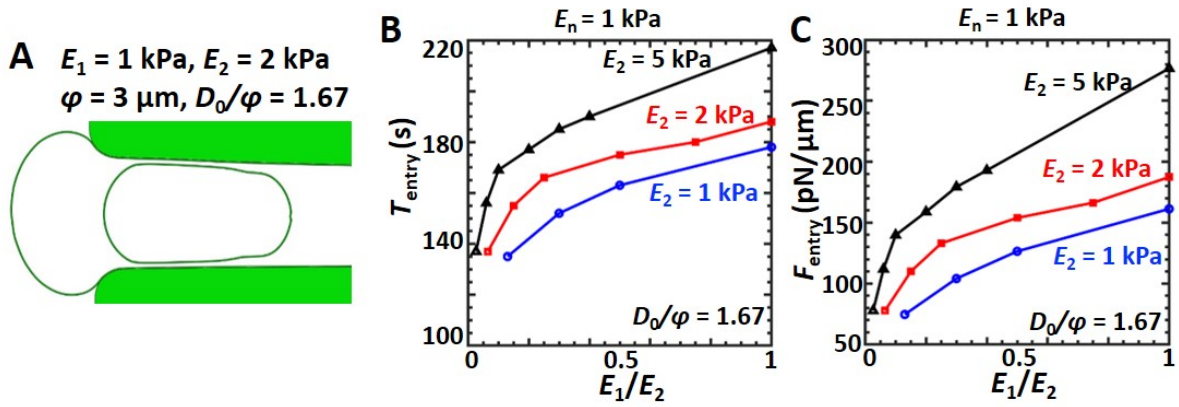


Figure 2.5: **Interplay of nuclear and tissue stiffness on dynamics of pore entry for interfacial migration.** (A) Nuclear deformation for the case of cell entry through an interface between two dissimilar tissues. Dependence of (B) T_{entry} , and (C) F_{entry} on E_1/E_2 for $D_0/\phi = 1.67$ and $E_n = 1 \text{ kPa}$.

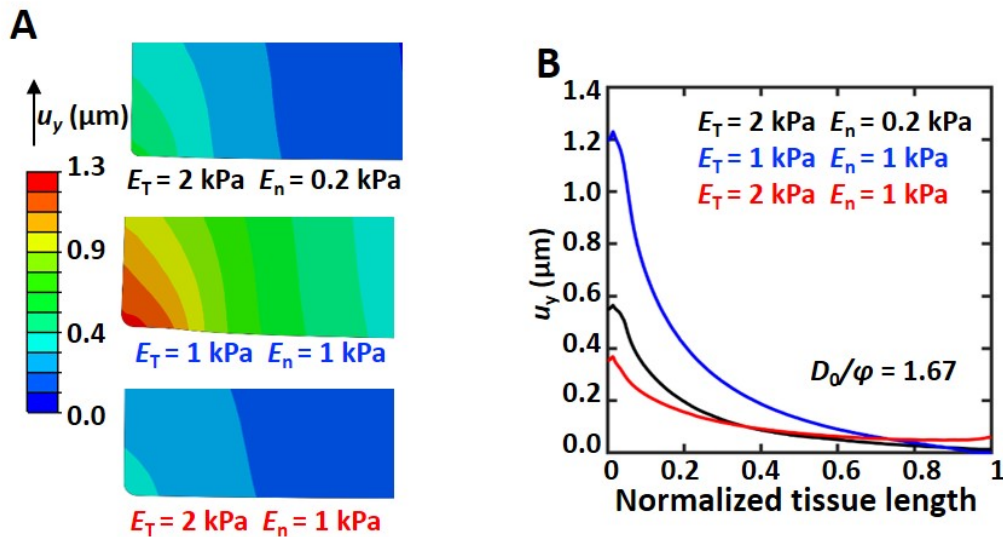


Figure 2.6: **Deformation of ECM after nucleus entry into pore.** (A) Contour plots of vertical tissue displacement (u_y) at the time of nucleus entry into the pore, i.e., when the entire nucleus has just completed entering the pore. (B) Spatial dependence of u_y along the tissue length at the time of pore entry for different values of E_T and E_n and $D_0/\phi = 1.67$. Pore entry occurs at normalized tissue length = 0.

2.6.2 Degree of confinement and nuclear/tissue properties collectively dictate average cell speed

To probe how nuclear/tissue properties and the extent of confinement influence cell motility, cell velocity (v_x) was tracked along the direction of migration, i.e., x -direction. v_x remained nearly zero for an extended duration, and shot up drastically towards the end (Fig. 2.7A). The normal force on the cell imposed by the ECM resists the rapid movement of the cell and cell stalls before entry into the pore. This normal resistive force imposed by the ECM depends on nucleus and ECM stiffness in our model. The cell enters the pore after a critical protrusive force $F_P (< F_{entry})$ is attained. From our model predictions, it was found that $\approx 40 - 45\%$ of the cell nucleus needs to enter the pore just before the drastic increase in instantaneous speed. The dependence of the average velocity $\langle v_x \rangle$ on E_n/E_T was dictated by D_0/ϕ and E_n (Fig. 2.7B). Sensitivity of $\langle v_x \rangle$ to E_n/E_T increased with E_n for all D_0/ϕ . However, for $D_0/\phi = 1.2$, $\langle v_x \rangle$ scaled positively with E_n/E_T and negatively with E_n . As per our expectations, $\langle v_x \rangle$ increases with decrease in D_0/ϕ as this implies that the cell has to overcome less mechanical resistance from the ECM to enter the pore. However, we find that although $\langle v_x \rangle$ has negligible sensitivity to E_n/E_T for $D_0/\phi = 1$ and $E_n = 0.2$ kPa, a monotonically increasing trend emerges for $E_n = \{2, 5\}$ kPa as E_T decreases from 5 kPa to 0.5 kPa. When instantaneous velocity was quantified in case of $D_0/\phi = 1$, some stalling behaviour of the cell was observed similar but for less time duration than Fig. 2.7A. This was due to the mechanical resistance of ECM on cell cytoplasm. Stalling was more pronounced for $E_n = E_T = 5$ kPa, as can be expected.

A few overlapping regions are also seen in Fig. 2.7B, especially for $D_0/\phi = \{1.2, 1.67\}$. This implies that mechanical resistance provided by the ECM on cells are probably at par with each other for these values of D_0/ϕ . Here, it should be noted that the observed non-monotonic behaviour for $D_0/\phi = 1.67$ is due to the choice of selection of timesteps that are output as a result of the simulations. For considerations of reasonable computational time, I chose to output the result at timestep differences of 1 second. This was motivated by the reason that in the highly confined migration cases ($D_0/\phi = 1.67$), the time taken by the cell to migrate is very long and a 1 second resolution seemed more prudent than guessing a suitable intermediate timestep.

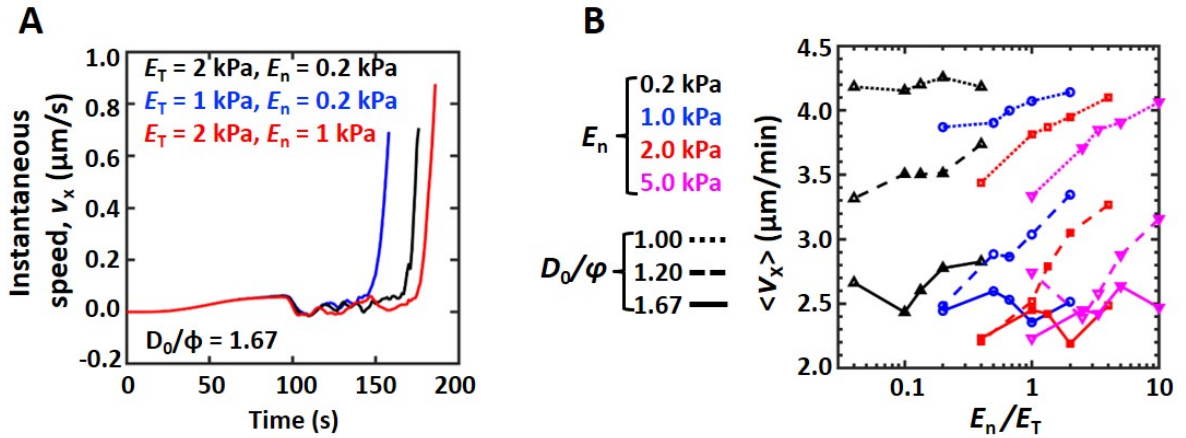


Figure 2.7: **Cell migration speed through confinement.** (A) Instantaneous cell velocity (v_x) calculated from the start of the simulation ($t = 0$ s) till the instant of pore entry. $D_0/\phi = 1.67$ for these three cases.

(B) The dependence of average cell velocity ($\langle v_x \rangle$) on E_n/E_T for different values of E_n and D_0/ϕ .

Tracking temporal evolution of the normalized distance between the leading edge of the cell and the proximal edge of the nucleus ($x_{CN}(t)$) revealed several-fold increase in x_{CN} over the initial undeformed distance $x_{CN}(0)$, indicative of cytoplasmic stretching in the direction of migration (Fig. 2.8A, B). In comparison, the extent of nuclear stretch ($x_N(t)/x_N(0)$) was much less. While the period of near zero velocity coincided with duration of cytoplasmic stretch with negligible nuclear deformation, the sudden increase in cell velocity ($t \approx (150 - 180)$ sec) corresponded to nuclear entry into the pore. Nuclear circularity (i.e., D/L) plotted as a function of E_n/E_T collapsed onto a master curve depending on the magnitude of E_n (Fig. 2.8C). Lowest D/L (≈ 0.36) was observed for $E_n = 1$ kPa and $E_T = 5$ kPa. Together, these results suggest that cell speed is dictated not only by nuclear/tissue properties, but also by the extent of confinement.

2.6.3 Plastic deformation of the nucleus and kink formation during pore entry

Alteration in nuclear circularity during pore entry is indicative of varying extents of nuclear stresses during and after entry (Fig. 2.9). Among the representative cases shown in Fig. 2.9,

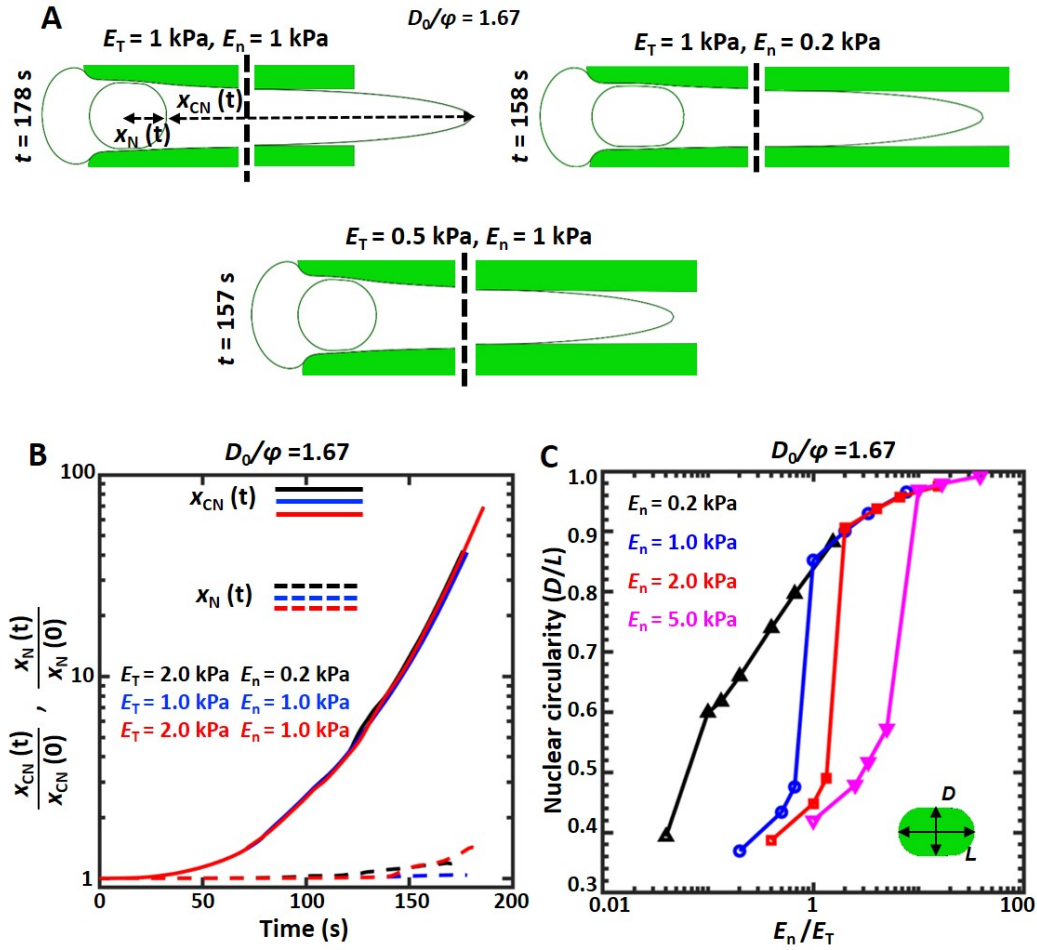


Figure 2.8: **Morphological changes in cell/nucleus during confined migration.** (A) Shapes of the cell and the nucleus at the time of pore entry for different combinations of E_T and E_n and $D_0/\phi = 1.67$. $x_{CN}(t)$ represents the distance between the leading edge of the cell and the front edge of the nucleus at time t . $x_N(t)$ represents the distance between the nucleus center and its front edge at time t . Dotted lines depict breaks in the cell profiles. (B) Temporal evolution of cytoplasmic stretch ($x_{CN}(t)/x_{CN}(0)$) and nuclear stretch ($x_N(t)/x_N(0)$) along the direction of migration for $D_0/\phi = 1.67$. (C) Dependence of nuclear circularity (D/L) on E_n/E_T for $D_0/\phi = 1.67$ and different values of E_n .

the highest stress in the nucleus was observed for the case of $E_n = 0.2 \text{ kPa}$, $E_T = 2 \text{ kPa}$, where $|E_T - E_n|$ is maximum. Surprisingly, when the nucleus was 5 times stiffer (i.e., $E_n = 1 \text{ kPa}$), stress in the nucleus was lower, and the nucleus was more elongated, raising the possibility of its plastic deformation. In our model, plastic deformation of the nucleus follows a strain hardening power law with the nuclear stress σ given by the expression $\sigma = a + b\epsilon_{plastic}^n$, with a , b and n representing material parameters acquired by fitting experimental data (see Methods). Indeed,

plastic deformation was observed for cases wherein the nucleus was stiff (i.e., $E_n \geq 1$ kPa) and the tissue stiffer (i.e., $E_T \geq E_n$) (Fig. 2.10A). For these cases, dramatic drop in nuclear circularity was observed, i.e., $D/L < 0.6$ (Fig. 2.8C). Plastic deformation was also observed for cells with stiff nuclei ($E_n = 5$ kPa) transiting through moderately stiff matrices ($E_n = 1 - 2$ kPa); however, localized kinking did not occur for these cases. Plastic nuclear deformation was found to be associated with reduced nuclear stresses (Fig. 2.10B).

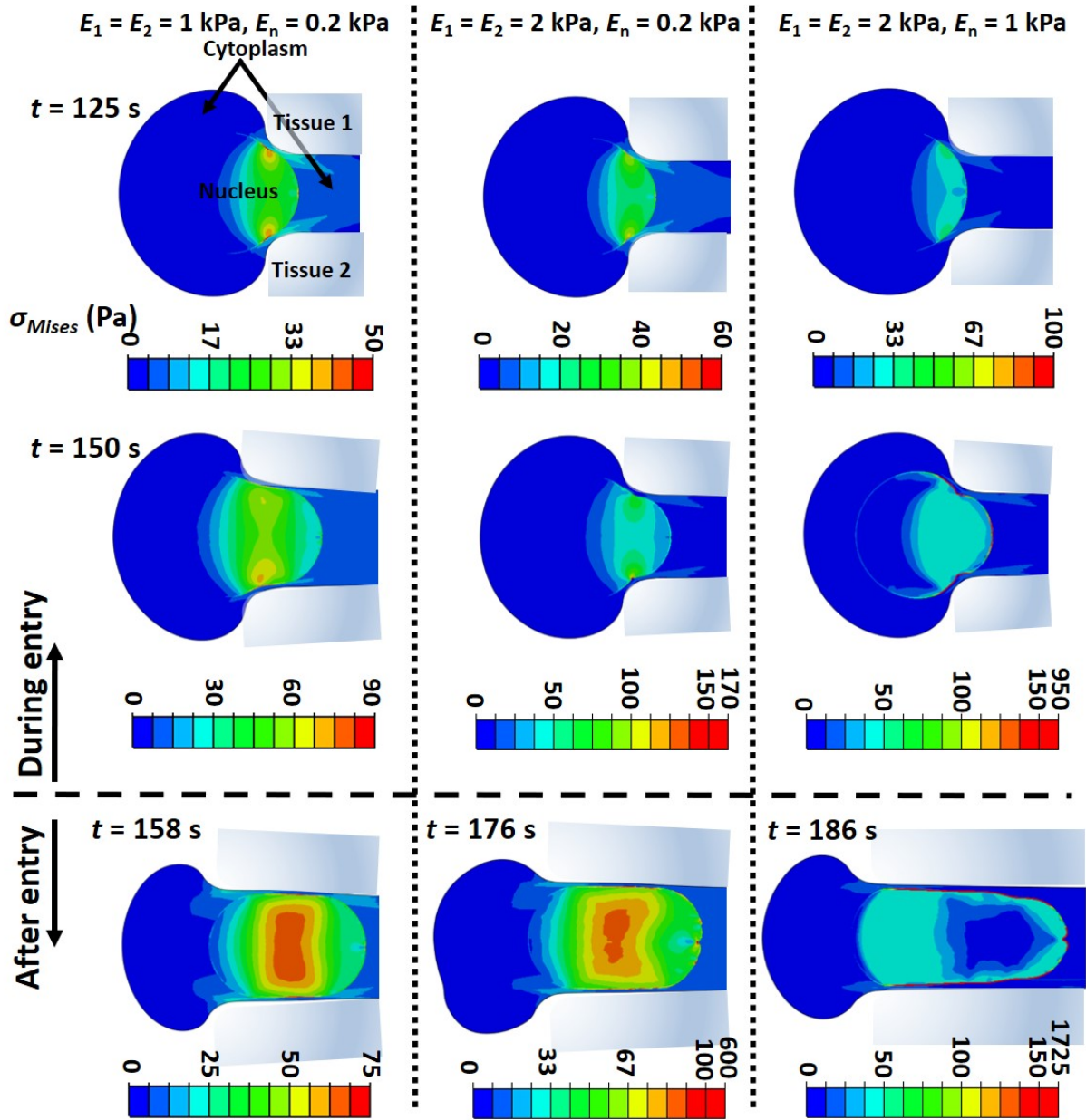


Figure 2.9: **Quantification of intracellular and intranuclear stresses during confined migration.** The spatiotemporal evolution of stress distribution before and after entry of a $5\mu\text{m}$ nucleus into a $3\mu\text{m}$ pore, i.e., $D_0/\phi = 1.67$. Contours and colourbars indicate von Mises stresses (σ_{Mises}) developed in the cytoplasm and nucleus.

Interestingly, profiles of plastically deformed nuclei revealed the presence of kinks at the front edge with large kink formation observed for the cases of $E_n \geq 1$ kPa, $E_T = (2, 5)$ kPa (Fig. 2.10A). Interfacial migration (i.e., $E_1 \neq E_2$) through stiff matrices was also found to be facilitated by plastic deformation (Fig. 2.11A). A plot of temporal evolution of hoop stress ($\sigma_{\theta\theta}$) during pore entry revealed varying stress profiles across the front end of the nuclear membrane

marked by the green-black and red-blue dots (Fig. 2.10C). For a stiff nucleus, necking was observed at the lateral edges when it is squeezed to enter the pore (Fig. 2.11B). This was also observed to be the location of initiation of plastic deformation. Necking temporally precedes kink formation at the front edge of the nucleus. For soft nucleus, i.e., $E_n = 0.2$ kPa, the front end of the nuclear membrane (i.e., green-black dots) was under compressive stresses (negative hoop stress) only. In contrast, for stiff nucleus, i.e., $E_n = 2$ kPa, while the outer edge of the front end of the nuclear membrane (i.e., blue dot) underwent drastic increase in compressive stresses, the inner edge of the nuclear membrane (i.e., red dot) underwent a sudden switch from compressive to tensile stresses. A bifurcation in stresses (red and blue curves, Fig. 2.10C) in the membrane creates a condition of extreme bending deformations which might be indicative of localized structural disintegration. In addition to highlighting the prominent role of plastic deformation of the nucleus in enabling entry into small pores, our results suggest that buildup of stresses during entry may lead to nuclear membrane damage.

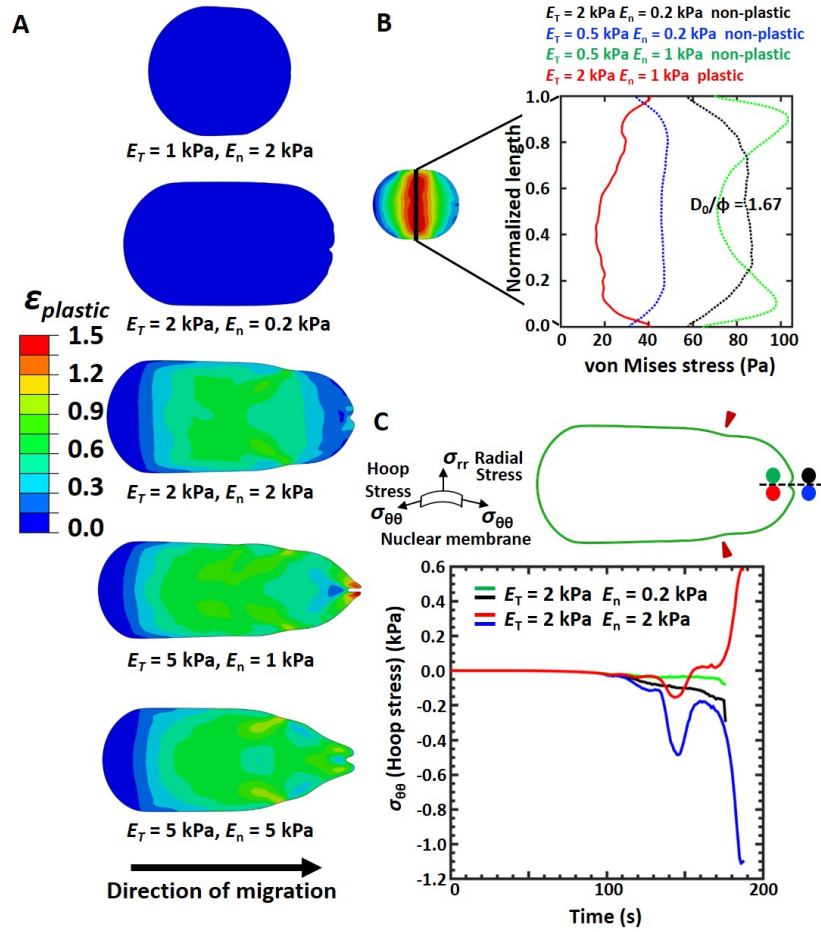


Figure 2.10: **Nuclear plasticity during confined migration.** (A) Spatial map of plastic strain ($\epsilon_{plastic}$) accumulated in the nucleus just after pore entry. The total strain (ϵ_{total}) in a body is defined as the sum of elastic ($\epsilon_{elastic}$) and plastic strain, i.e., $\epsilon_{total} = \epsilon_{elastic} + \epsilon_{plastic}$. $\epsilon_{elastic}$ is defined as the reversible strain in the body whereas, $\epsilon_{plastic}$ is irreversible. We use a strain hardening material property definition given by: $\sigma = a + b\epsilon_{plastic}^n$, where σ is the applied stress, $\sigma_{yield} = a$, and a , b and n are material properties. (B) Spatial distribution of von Mises stress in the nucleus along the vertical direction just after nuclear entry ($D_0/\phi = 1.67$). (C) Temporal evolution of hoop stresses ($\sigma_{\theta\theta}$) in the nuclear membrane from the start of simulation to the instant the nucleus completely enters the pore. The two cylindrical components of stresses, namely, radial (σ_{rr}) and hoop ($\sigma_{\theta\theta}$) stress in the nuclear membrane are depicted along with the region of nuclear membrane from which the curves are extracted ($D_0/\phi = 1.67$). Green-Black and Red-Blue curves correspond to two different combinations of E_T and E_n as shown. Green and Red dots in the representative snapshot of the nuclear membrane correspond to kinked mesh elements on the nuclear membrane at its interface with the nucleus for $E_n = 0.2 \text{ kPa}$ and $E_n = 2 \text{ kPa}$ respectively. Similarly, Black and Blue dots correspond to kinked mesh elements on the nuclear membrane at its interface with the cytoplasm.

2.6.4 Nuclear plasticity and DNA damage: insights from experiments

To finally compare our simulation predictions with experiments, confined migration experiments were performed using HT-1080 fibrosarcoma cells which are highly invasive and are capable of switching from proteolytic to non-proteolytic migration upon inhibition of protease activity (Wolf et al., 2003). This switch is enabled by nuclear softening through phosphorylation of Lamin A/C, and can also be induced by treatment with the non-muscle myosin II inhibitor blebbistatin (hereafter Blebb) (Das et al., 2019). To assess the importance of nuclear stiffness and nuclear plasticity during confined migration, experiments were performed in the presence of Blebb and the CDK inhibitor RO-3306 (hereafter RO), which inhibits lamin A/C phosphorylation (Kumar et al., 2018b). Cells treated with DMSO served as controls. At the drug doses used, no obvious differences in cell morphology were observed (Fig. 2.12A). While nuclear volume was preserved across the three conditions (Figs. 2.12B, C), AFM probing of nuclear stiffness with a stiff tip right at the center of the cell (above the nucleus), and fitting of $\sim 2 \mu\text{m}$ of force curves revealed reduction in nuclear stiffness of Blebb-treated cells compared to controls (Fig. 2.12D, E). In comparison, RO-treated nuclei were significantly stiffer.

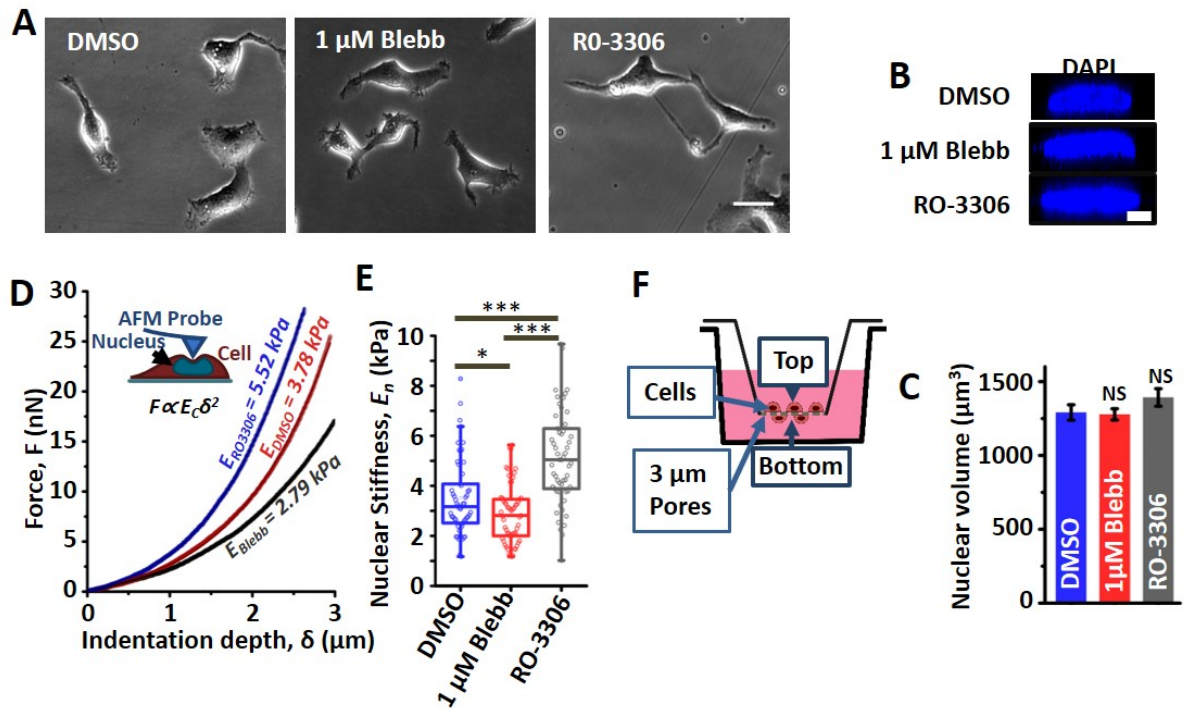


Figure 2.12: **Experiment setup and mechanical characterization of cells.** (A) Phase contrast images of HT-1080 fibrosarcoma cells treated with vehicle (DMSO), 1 μM blebbistatin (Blebb) or 10 μM RO-3306 (RO) for 12 hours. Scale bar = 30 μm . (B) Representative XZ plane images of DAPI stained nuclei of DMSO, Blebb and RO-treated cells. Scale bar = 5 μm . (C) Quantitative analysis of nuclear volume ($n = 20 - 50$ nuclei per condition across 2 independent experiments). Error bars represent $\pm\text{SEM}$. Statistical significance was determined by one-way ANOVA/Fisher Test; NS: $p > 0.05$. (D) Probing nuclear stiffness of cells with a stiff pyramidal probe. Cells were treated with DMSO, Blebb or RO for 12 hours prior to experiments. Nuclear stiffness values were estimated by fitting $\geq 2 \mu\text{m}$ of indentation data using Hertz model. (E) Quantification of nuclear stiffness of DMSO-treated, Blebb-treated and RO-treated cells ($n = 40 - 60$ nuclei per condition across 2 independent experiments). Error bars represent $\pm\text{SEM}$. Statistical significance was determined by one-way ANOVA/Fisher Test; * $p < 0.05$, *** $p < 0.001$. (F) Schematic of transwell migration assay through 3 μm pores; Cells were seeded in the upper chamber containing plain DMEM supplemented with DMSO or drugs. Lower chamber was labelled with DMEM containing 20% serum for creating a chemokine gradient.

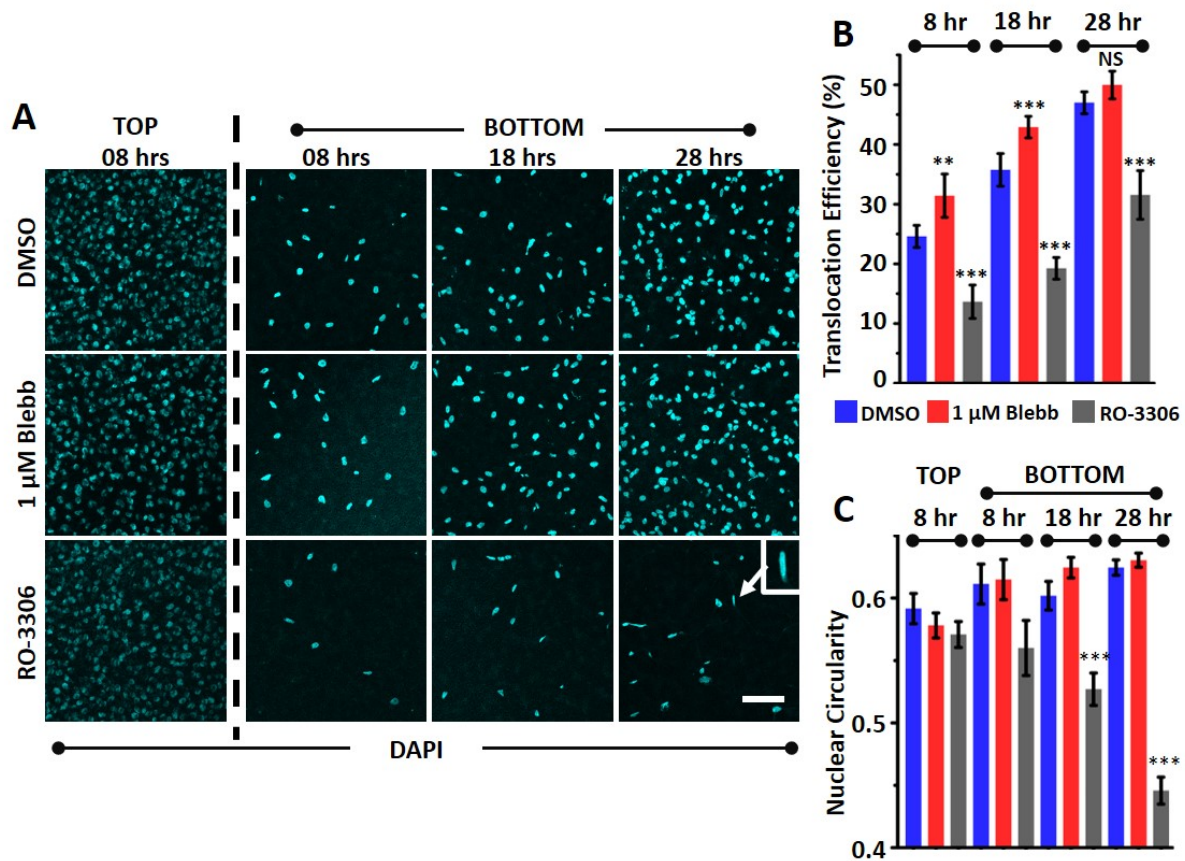


Figure 2.13: **Influence of nuclear stiffness on pore migration efficiency and nuclear plasticity.** (A) Representative DAPI stained images of nuclei in upper chamber (referred to as TOP) and lower chamber (referred to as BOTTOM) at 8, 18 and 28 hrs after cell seeding; Scale bar = 100 μm . (B) Quantification of translocation efficiency of DMSO/Blebb/RO-treated cells at 3 different time-points ($n \geq 900$ nuclei per condition were counted in the upper chamber; experiment was repeated thrice). (C) Quantification of nuclear circularity of DMSO/Blebb/RO-treated cells at the top (8 hr time point) and at the bottom surface of the pores at 3 different time-points ($n > 80$ nuclei per condition; experiment was repeated twice). Error bars represent $\pm\text{SEM}$. Statistical significance was determined by one-way ANOVA/Fisher Test; *** $p < 0.001$, ** $p < 0.01$, NS: $p > 0.05$.

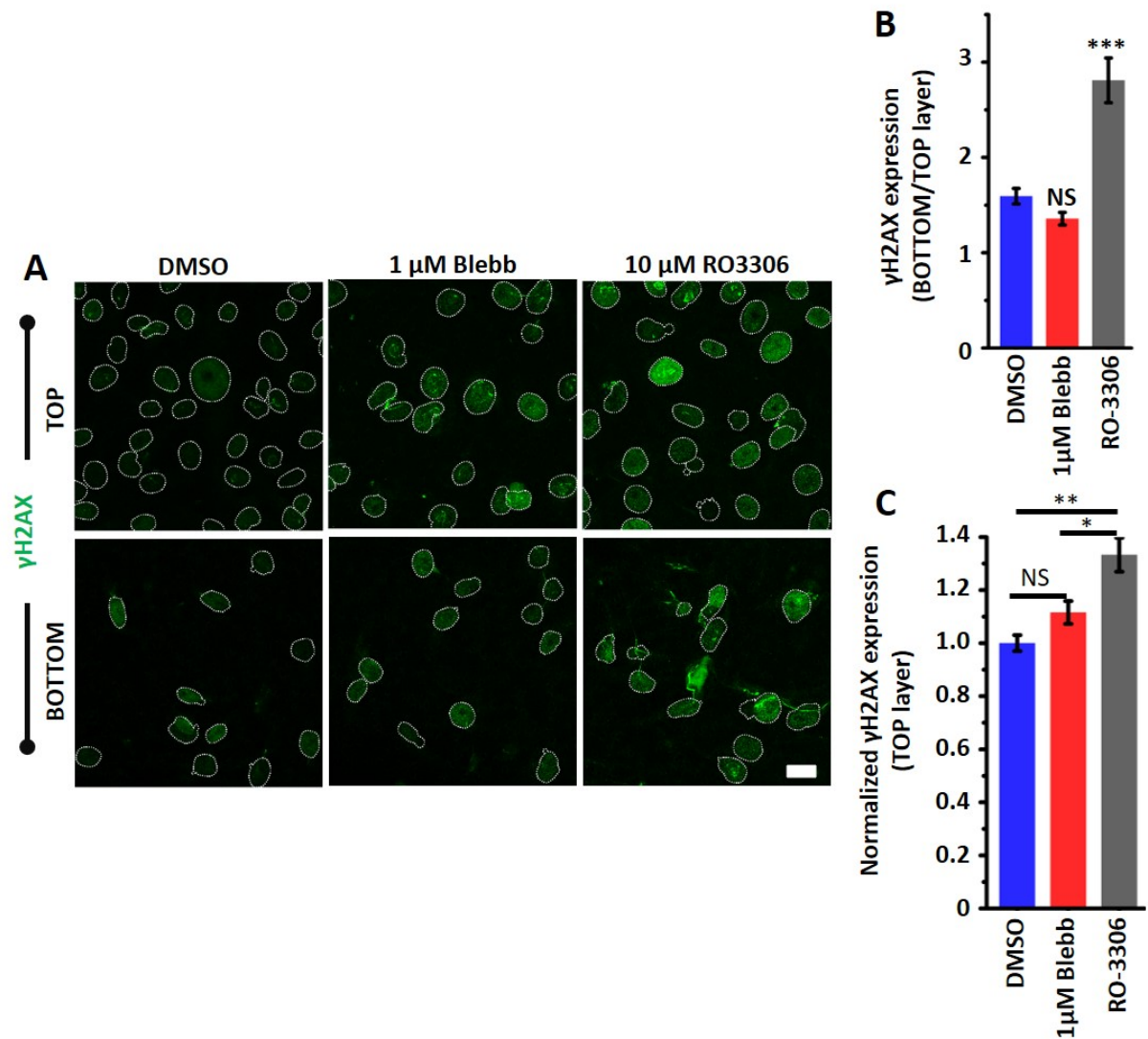


Figure 2.14: **Plastic deformation of the nucleus increases susceptibility to damage.** (A) Representative γ H2Ax-stained images of DMSO/Blebb/RO-treated cells in upper chamber (referred as TOP) and lower chamber (referred as BOTTOM) of transwell pores 28 hrs after cell seeding. Nuclei are outlined with white dotted lines; Scale Bar = 20 μ m. (B) Quantification of ratio of integrated γ H2Ax intensity between BOTTOM layer and TOP layer in DMSO/Blebb/RO-treated cells ($n = 40 - 120$ nuclei per condition; experiment was repeated twice). Error bars represent \pm SEM. Statistical significance was determined by Mann-Whitney test; *** $p < 0.001$, NS: $p > 0.05$. (C) Quantification of γ H2AX expression intensity normalized to DMSO condition at the TOP layer.

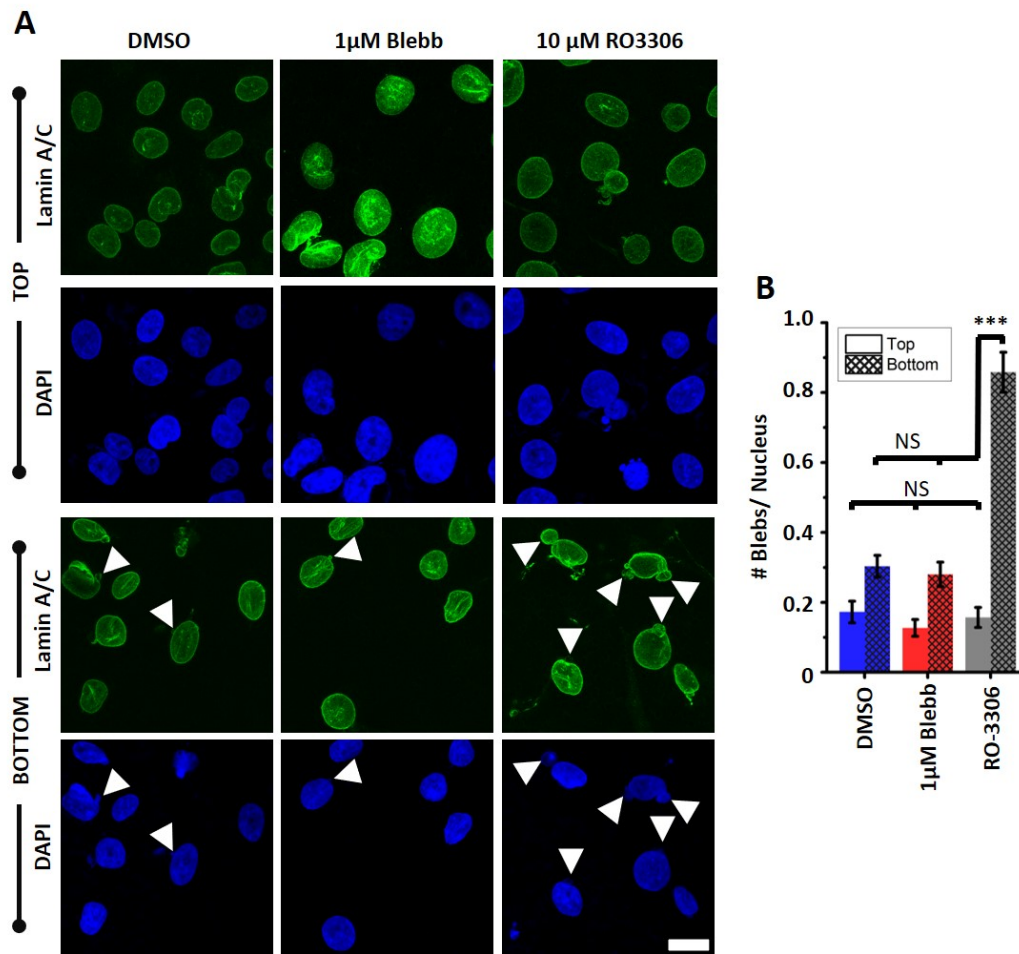


Figure 2.15: **Plastic deformation of the nucleus increases susceptibility to damage.** (A) Representative Lamin A/C (green) and DAPI (blue) stained images of DMSO/Blebb/RO-treated cells in Top and Bottom layer of transwell pores at 28 hrs after cell seeding. White arrows indicate nuclear blebs. Scale bar = 20 μ m. (C) Quantification of average number of blebs per nucleus in DMSO/Blebb/RO-treated cells in top and bottom layer of the transwell inserts ($n > 250$ nuclei per condition pooled from two independent experiments). Error bars represent \pm SEM. Statistical significance was determined by Mann-Whitney test; *** $p < 0.001$, NS: $p > 0.05$.

To assess the implications of these alterations in nuclear stiffness on the efficiency of confined migration, transwell migration through 3 μ m pores was performed wherein cells were plated on the top of the transwell pores and the fraction of cells reaching the bottom was quantified at three different time-points, i.e., 8, 18 and 28 hours after seeding (Figs. 2.12F, 2.13A). Cells were stained with DAPI for ease of cell counting as well as for assessing nuclear morphology before and after transit through the pores. Time-snaps of the number of cells that transited

through the pores and reached the bottom surface illustrated the clear advantage of nuclear softening during confined migration. While the number of nuclei at the bottom were comparable in DMSO and Blebb-treated cells at all the three time-points, the number of RO-treated nuclei were significantly lesser (Fig. 2.13A). Quantification of translocation efficiency, i.e., the fraction of cells that transited through the pores, revealed Blebb-treated cells to be the most efficient in pore migration, and RO-treated cells to be the least efficient (Fig. 2.13B).

To next assess the possibility of nuclei undergoing plastic deformation during pore migration, nuclei shape was quantified by measuring nuclear circularity as a function of time. Nuclear circularity of DMSO and Blebb-treated cells remained unchanged across the three time-points, and were comparable with cells that remained at the top surface (Fig. 2.13C). Though nuclear circularity of RO-treated cells was comparable to that of DMSO and Blebb-treated cells at the 8 hr time-point, there was a gradual drop in nuclear circularity with time with maximum drop of $\approx 25\%$ observed at the 28 hour time-point. The dramatic change in nuclear circularity of RO-treated cells suggests that nuclei of these cells have undergone plastic deformation and retain their deformed shapes.

To finally probe the link between the nature of nuclear deformation (i.e., elastic versus plastic) and nuclear damage, cells were stained with γ H2Ax, a marker of DNA damage, before and after transwell migration (Fig. 2.14A). Quantification of γ H2Ax intensity normalized to DMSO condition revealed higher basal level of damage in RO-treated cells, but no change in Blebb-treated cells (Fig. 2.14C). These baseline differences were amplified to different extents after transwell migration. Quantification of the ratio of γ H2Ax levels between BOTTOM layer and TOP layer revealed $\approx (30 - 50)\%$ increase in DMSO and Blebb-treated cells (Fig. 2.14B). In comparison, $\approx 200\%$ increase was observed in RO-treated cells. To establish a direct correlation between γ H2Ax levels and nuclear damage, nuclei co-stained with Lamin A/C and DAPI were imaged for visualizing formation of nuclear blebs (white triangles, Fig. 2.15A). For all the three conditions, the proportion of nuclei with blebs remained unchanged in cells in the TOP layer, but increased after transwell migration to different extents (Fig. 2.15B). Specifically, the proportion of cells with nuclear blebs increased from $\approx 30\%$ in DMSO/Bleb-treated cells to $\approx 90\%$ in RO-treated cells. Together, these results validate our model predictions and suggest that plastic deformation of the nucleus increases susceptibility to DNA damage.

2.6.5 Scaling relationships

The cellular force required for a nucleus to successfully enter a pore is expected to depend on both nuclear stiffness and tissue stiffness. Plotting of F_{entry} versus T_{entry} corresponding to $D_0/\phi = 1.67$ for different combinations of E_T and E_n revealed a nearly cubic scaling relationship with a factor of 2.78 (Fig. 2.16A). The dynamic change in nuclear circularity over the period of entry into the pore is then a function of the aforementioned factors. The ratio of initial nuclear size to initial pore size (D_0/ϕ) is of limited value for analyzing cell migration through deformable matrices because the pore size widens with the passage of a cell nucleus through it. A non-dimensionalized scaling relationship between nuclear circularity (D/L) and a combination of tissue and nuclear stiffness (E_1E_2/E_n^2) shows the slopes followed by cells of varying nuclear stiffness (Fig. 2.16C). Force required by a cell of given cell/nuclear stiffness for entering a pore is well fit by the following power law with an exponent of 0.43 ($R^2 = 0.75$) (Eq. 1) (Fig. 2.16B):

$$\frac{F}{E_c D} = \left(\frac{E_1 + E_2 + E_n}{E_c} \cdot \frac{L}{D} \cdot \frac{t}{\tau_c} \right)^{0.43} \quad (2.6)$$

where, E_c , t and τ_c refer to cytoplasmic stiffness, time of pore entry and viscoelastic time constant of the cytoplasm respectively. The dimensional force itself was found to increase exponentially with D/L with the exponents dictated by E_n and the extent of plastic deformation (Fig. 2.16D). The magnitude of the exponent was highest for the case of stiff nucleus ($E_n = 1$ kPa) undergoing plastic deformation, lowest for the case of stiff nucleus undergoing non-plastic deformation, and intermediate for the case of soft nucleus ($E_n = 0.2$ kPa) undergoing non-plastic deformation. These scaling relationships can be utilized for predicting cell generated forces based on experimentally observed parameters such as nuclear circularity and mechanical properties of various cellular and tissue structures.

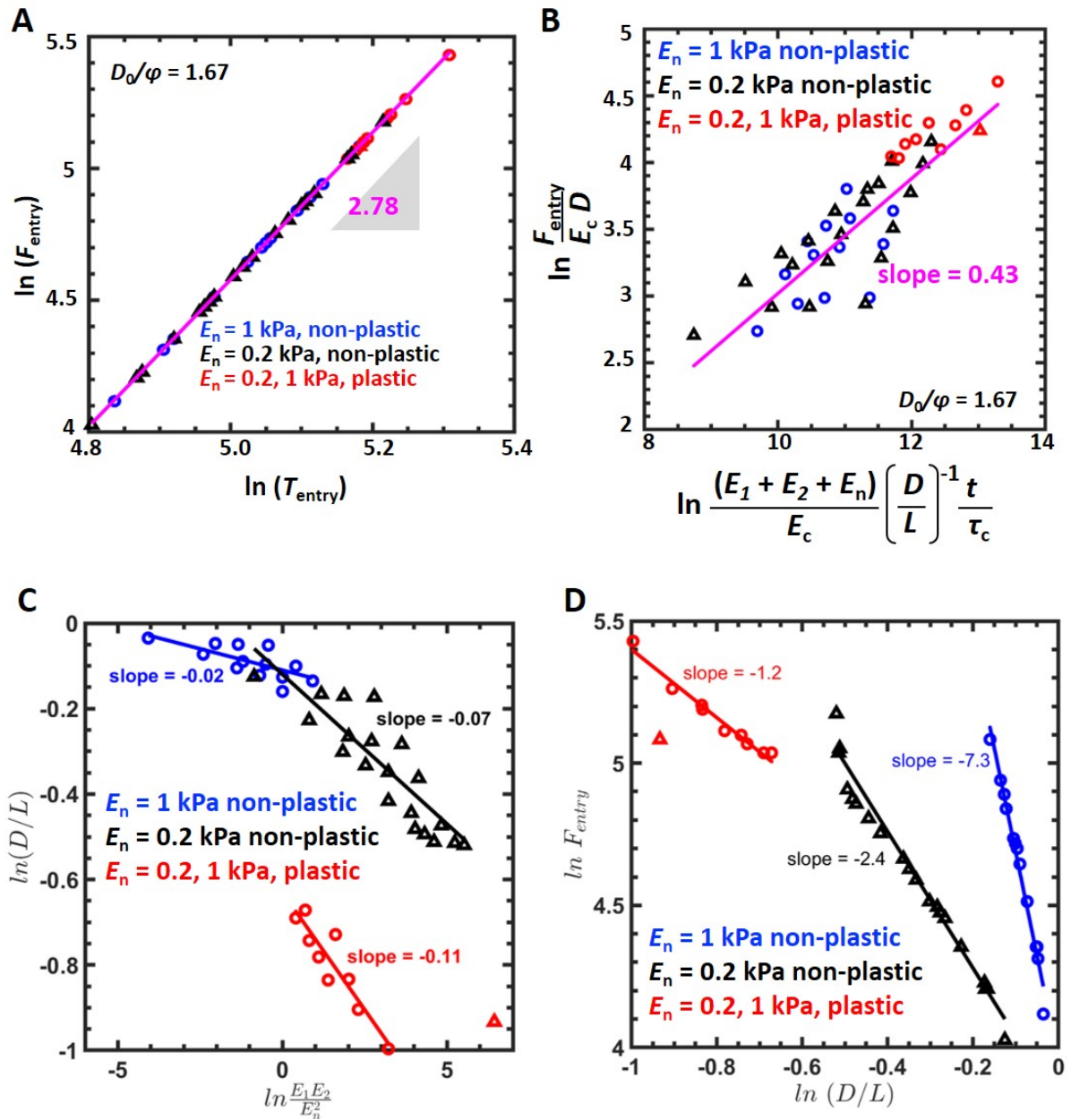


Figure 2.16: **Scaling relationships.** (A) Scaling relationship between F_{entry} ($\text{pN}/\mu\text{m}$) and T_{entry} (s) for $D_0/\phi = 1.67$. (B) Non-dimensional cellular force scaled with possible parameters affecting the cellular force generation during confined migration for $D_0/\phi = 1.67$. Scaling between nuclear circularity and (C) the coupled effect of tissue and nuclear stiffness, and (D) force required by a cell to enter a pore. All datapoints refer to the condition $D_0/\phi = 1.67$. E_1 and E_2 vary from 0.13 to 5 kPa.

2.7 Discussion

The numerical model of cell migration under confinement presented in this study incorporates essential cellular features at the microscale, namely, nuclear elastoplasticity and viscoelasticity

of other cellular components and extracellular matrices in addition to stress-stiffening of cytoplasm that make it more realistic than previous FE models (Table 2.1). The dramatic increase in instantaneous migration speed of the nucleus observed in our simulations is consistent with experimental observations (Lautscham et al., 2015; Krause et al., 2019), and can be attributed to the sudden release of the built-up potential energy due to deformation of internal elastic springs in the cell and nucleus and its conversion into kinetic energy. Though the maximum possible intracellular protrusive force (F_p) defined in our model is comparable to literature reported values (Rabodzey et al., 2008; Neelam et al., 2015), the forces predicted by our model are nearly an order of magnitude lower than the values reported by Lele and co-workers (Neelam et al., 2015). These differences may arise due to the experimental setup and/or sensitivity of experimental assays. For example, in the aforementioned literature, micropipette aspiration was performed on cells adherent on glass and migrating through stiff PDMS micropillars ($E \approx 2$ MPa).

Our model predicts that while migrating through matrices stiffer than the nucleus (i.e., $E_T/E_n > 1$), the nucleus undergoes plastic deformation (Fig. 2.17A). Plastic deformation of the nucleus was also observed for the case of a cell with a stiff nucleus ($E_n = 5$ kPa) migrating through a relatively soft matrix ($E_T = 1 - 2$ kPa). However, kink formation was observed for the first case only. Long-term change in nuclear circularity of RO-treated cells observed at the 28 hr time-point, but not of DMSO and Blebb-treated cells, is indicative of nuclei of RO-treated cells undergoing plastic deformation. However, at the 8 hr time-point, nuclear circularity of RO-treated cells which transited to the bottom of the pores was comparable to that of DMSO and Blebb-treated cells as well as with that of cells at the top. Given the broad heterogeneity in nuclear stiffness measurements, we speculate that RO-treated cells which reached the bottom of the transwell pores at the 8 hr time-point correspond to a sub-population of cells with softer nuclei which underwent elastic deformation during pore migration.

Since Lamin A/C levels scale with tissue stiffness (Swift et al., 2013), our results of cells with stiff nuclei migrating through stiffer tissues correspond to cancers such as osteosarcoma, wherein migration-induced DNA damage has been shown to cause genomic heterogeneity (Irianto et al., 2017). Stiff nuclei have been reported to result from increased lamin A concentration in the nucleus (Harada et al., 2014), especially in the genetic mutations caused in the Hutchinson Gilford Progeria Syndrome (HGPS) (Kaufmann et al., 2011; Verstraeten et al., 2008). In comparison, the absence of nuclear kinks in cells with soft nuclei passing through

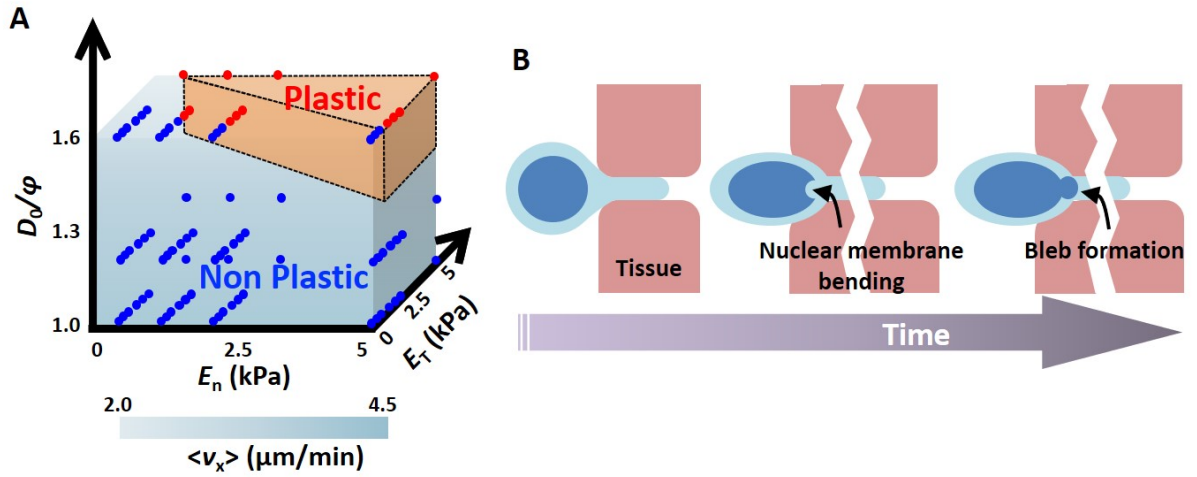


Figure 2.17: **Proposed model of nuclear damage.** (A) Phase diagram depicting the zones of non-plastic and plastic nuclear deformation required for pore entry for different values of E_n , E_T and D_0/ϕ . (B) Proposed model of nuclear damage. Compressive forces imposed by the surrounding tissues cause initial nuclear membrane damage. This serves as the precursor to nuclear bleb formation.

stiff matrices suggests that nuclear softening may represent a robust strategy utilized by cells to migrate through pores without undergoing nuclear membrane rupture. Consistent with this idea, γ H2Ax levels and the average number of nuclear blebs were comparable in control and Blebb-treated cells, but significantly elevated in RO-treated cells.

The relative insensitivity of average cell speed to E_n/E_T suggests that tissue stiffness-dependent temporal tuning of nuclear stiffness by lamin A/C phosphorylation may enable cancer cells to migrate at comparable efficiency through tissues of varying composition and pore sizes. Approximating the nuclear membrane and the lamina as a simply supported elastic plate of thickness h , the flexural rigidity (F_D) can be given as (Timoshenko and Woinowsky-Krieger, 1959):

$$F_D \approx \frac{Eh^3}{(1-\nu^2)} \quad (2.7)$$

where, E and ν are elastic properties of the nuclear lamina. Since thickness h has a relatively greater influence on flexural rigidity compared to stiffness E , a thin lamina is more prone to damage due to bending than a soft lamina. This might explain increased blebbing due to nuclear

damage reported in laminopathies (loss of lamin A/C) but not in immune cells or cancers with soft nuclei.

The chromatin contained within the nucleus is a major determinant of nuclear deformation. Mechanotransduction between the actin cytoskeleton and nucleoplasm through the interconnecting LINC complex has been shown to play a critical role in chromatin dynamics during DNA repair Swartz et al. (2014) and gene transcription (Tajik et al., 2016; Stephens et al., 2019). The spatial organization of the chromatin changes with nuclear stress and shape change. Compact chromatin network acts as an elastic spring to resist small deformations (Stephens et al., 2019). While small strains lead to strain stiffening of nuclei due to chromatin compaction (Stephens et al., 2017), large deformation of nuclei is facilitated by the actin and vimentin cytoskeleton (Patteson et al., 2019) and Lamin A/C (Stephens et al., 2017). Change in spatial organization of chromatin fibers can possibly lead to permanent plastic deformation of nuclei. A full rupture in the membrane allows the intranuclear pressure to become more than the intracellular pressure, thus facilitating the leakage of genetic material into the cytosol. An alternate mechanism is also observed in cells migrating under confinement where the nuclear membrane gets mechanically decoupled from the nuclear lamina which leads to membrane blebbing due to chromatin flow into this vacant pocket of space (Deviri et al., 2017). This experimental observation can be linked to our model prediction (Fig. 2.17B) where we find that the nuclear lamina bends when the nucleus undergoes plastic deformation. This extreme nuclear bending as seen in Figs. 2.10A and C might result in delamination of the nuclear cortex from the nuclear membrane leading to bleb formation.

Nuclear blebbing has also been reported to be caused by influx of water into the nucleus under confinement (Mistriotis et al., 2019). In this study, we did not consider the effect of water influx into the nucleus, the characteristic time (τ) for which is found to be governed by the equation: $\tau = r_n^2/D_c$, where r_n is the radius of nucleus and D_c is the diffusion coefficient of water. Thus, for an undeformed nucleus of $r_n = 2.5 \mu\text{m}$ and $D_c = 50 \mu\text{m}^2/\text{s}$ (Moeendarbary et al., 2013), $\tau = 0.125 \text{ s}$, which is extremely small compared to the timescales of migration (minutes to hours), even smaller for deformed nuclei. Moreover, since we consider a quasi-static viscoelastic description of the model, we did not consider the transient poroelasticity of nuclei or cytoplasm. Our results show that there is a time-dependent spatial gradient of compressive forces on the nuclear lamina due to actomyosin fibres during nuclear entry into a pore. In such

a situation, by the time the nucleus completely enters into the pore, the front of the nucleus relative to the direction of migration has been under compressive stresses much longer than the rear. Therefore, the probability of nuclear membrane rupture at the nuclear front is much higher than at the rear as has been consistently reported in experiments. Compressive stresses beyond a critical threshold (yield stress σ_y) causes the nucleus to yield and this yield zone is also found to spread starting from the frontolateral region of the nucleus where necking occurs due to constriction to the rear of the nucleus (Fig. 2.11B). In case of stiff nuclei transiting through stiffer matrices ($E_n \geq 1$ kPa, $E_T \geq E_n$), plasticity-induced deformation of the nuclear membrane leads to buckling and finally membrane failure. The combination of nuclear stress profiles and γ H2Ax results suggests that plastic nuclear deformation that initiates at the nuclear lamina gets propagated throughout the nucleus.

Nuclear membrane rupture in micropipette aspiration experiments has been attributed to tensile stresses at the anterior periphery of the nucleus (Zhang et al., 2019; Xia et al., 2019). Similar results have been recapitulated by Cao et al. (Cao et al., 2016) in their model where they proposed that the front and lateral edges of the nucleus might be susceptible to tensile-stress induced damage during migration through ECM-like environments. Though these findings implicate tensile stresses as a factor contributing to nuclear damage, nuclei are primarily subjected to compressive forces during confined migration. Our observations of kink formation at the tip of the nuclear membrane proximal to the direction of migration correlates with experimental observations of the spatial location of nuclear damage during migration through extreme confinement in stiff environments (Raab et al., 2016; Hatch and Hetzer, 2016; Deviri et al., 2019). Since kink formation is expected to occur between the stages of nuclear compression, subsequent blebbing and eventual rupture, resolving it temporally during experiments is challenging. However, there might be some indication of kink formation in-vitro in a study by Lammerding and co-workers (Denais et al., 2016) where they show that lamin B is depleted from the region where membrane bleb is formed. They suggest that this is due to detachment of lamina from the membrane. In our simulations, this detachment can be related to mechanical delamination (similar to delamination in composite structures) under compression. The kink formation might be a consequence of excessive bending of the nuclear lamina driven by the combined effects of tissue stiffness and the peri-nuclear cytoskeleton. Formation of smaller lateral kinks might aid in the initiation of plastic deformation. We propose that rapid buildup of compressive and tensile stresses at the point of pore entry induces nuclear envelope damage; subsequent localized

delamination of the lamina from the nuclear membrane may serve as a precursor to experimentally observed nuclear blebbing (Fig. 2.15A). The genetic material, already under significant external pressure and previously held back by the structural integrity of the nuclear lamina, then oozes out through the damaged orifice to form a bleb that may eventually rupture subject to membrane tension. However, unless the damage is extreme, nuclear rupture is repaired using ESCRT machinery (Denais et al., 2016; Raab et al., 2016; Deviri et al., 2017). Our results suggest that compressive stress-induced membrane damage and nuclear blebbing only occurs in a specific window depending on nuclear/tissue stiffness and extent of confinement, and may be critical for migration through stiff environments. Our experimental observations indeed support this idea as change in nuclear circularity indicative of plastic deformation of the nucleus was only observed in RO-treated cells, where DNA damage was maximum. The lack of plastic deformation in Bleb-treated cells which were more invasive and had lesser DNA damage suggests that nuclear softening may be a more effective invasion strategy compared to nuclear plasticity.

2.8 Conclusion

In conclusion, we have developed a numerical model of confined cell migration that contributes to our understanding of the underlying physics of nuclear deformation and stresses during confined migration. We further validate our key prediction of nuclear plasticity leading to nuclear damage using experiments wherein RO-induced nuclear stiffening led to plastic deformation and higher DNA damage. Our model suggests that nuclear membrane damage in stiff nuclei plastically deformed by compressive stresses, may serve as the precursor for bleb formation that ultimately facilitates successful migration of a cell through stiff tissues.

Chapter 3

Mechanical modelling of the cellular glyocalyx

3.1 Introduction

A thick outer coat of sugars and proteins, called the glyocalyx, is generally found beyond the cell membrane in most eukaryotic cells. This coat is such that long polymeric chains (sometimes made of $\approx 20,000$ monomeric units) act as randomly coiled springs beyond their persistence length (usually about 10 nm (Shurer et al., 2019)) and as rigid beams below it. Such a coat has long been observed experimentally (Chang et al., 2016), but rarely modelled physically. Recent physical models developed shed light onto the possibility that this coat might be made of two classes of polymers, distinguished by their chain lengths (Iyer et al., 2009; Dokukin et al., 2016).

Experimental data and intensity mapping of the glyocalyx (or, pericellular matrix (PCM)) by (Chang et al., 2016) show that it increases in thickness over time before saturating, indicating a diffusion-based growth or polymerization in the region. Significantly, the authors find that this swelling is not the result of polymerization of HA, but rather due to the attachment of aggrecan molecules to the vacant sites in the HA polymeric chain. Attachment of aggrecan to HA leads to the stretching out of the HA polymer backbone due to steric hindrance thus forming a polymer brush around the cell.

The morphology of glyocalyx polymers found around cells can be differentiated into two primary types, namely, mushroom and brush depending on the side-chain length and orientation (Shurer et al., 2019). The mushroom configuration is found to occur when the polymer attachment density (N) is low where the polymers become more rounded and their persistence

length decreases due to less steric hindrance. Conversely, for high N and consequent high steric hindrance, the persistence length of glycocalyx polymers increases and they form elongated brush-like structures. These membrane configurations can be broadly classified according to the attachment density of glycocalyx polymers leading to formation of various polymer shapes on cell membranes into categories such as: flat or 2D, blebs, tubes and pearls. Fig. 3.1A shows a schematic of glycopolymer brush on a cell being compressed under indentation forces and Fig. 3.1B depicts existence of a glycocalyx (brush form) around a cell that is removed by the application of the enzyme Neuraminidase.

We developed a basic finite element model of cell migration in Chapter 2. However, we had considered a cell devoid of a coat of glycocalyx. In this Chapter, we consider a cell decorated with glycopolymers forming a brush attached to the cell membrane and evaluate its mechanical properties and impact on cell indentation and compression against the surrounding ECM. We first created axisymmetric models of cell indentation by a spherical indenter and glycocalyx compression with ECM due to a sandwich configuration using a hyperelastic definition of the glycocalyx. We then implemented these models to study cell migration through a matrix and understand the role of glycocalyx in aiding this process.

3.2 Materials and Methods

3.2.1 Methodology

We designed continuum models to mimic the mechanical effect of glycocalyx. According to AFM indentation data on the glycocalyx presented by the group of I. Sokolov (Iyer et al., 2009; Sokolov et al., 2013; Dokukin et al., 2016), we could not find evidence of adhesive contact between the AFM indenter and glycocalyx. Therefore, we did not use the JKR model (Johnson et al., 1971) which is used for adhesive contact between two elastic bodies.

The entropic brush model used to predict the indentation load on an indenter indenting a glycocalyx brush (Dokukin et al., 2016) assumed to be made up of polymer chains was equated to the Hertz model for contact between an indenter and a finitely thick glycocalyx on an in-

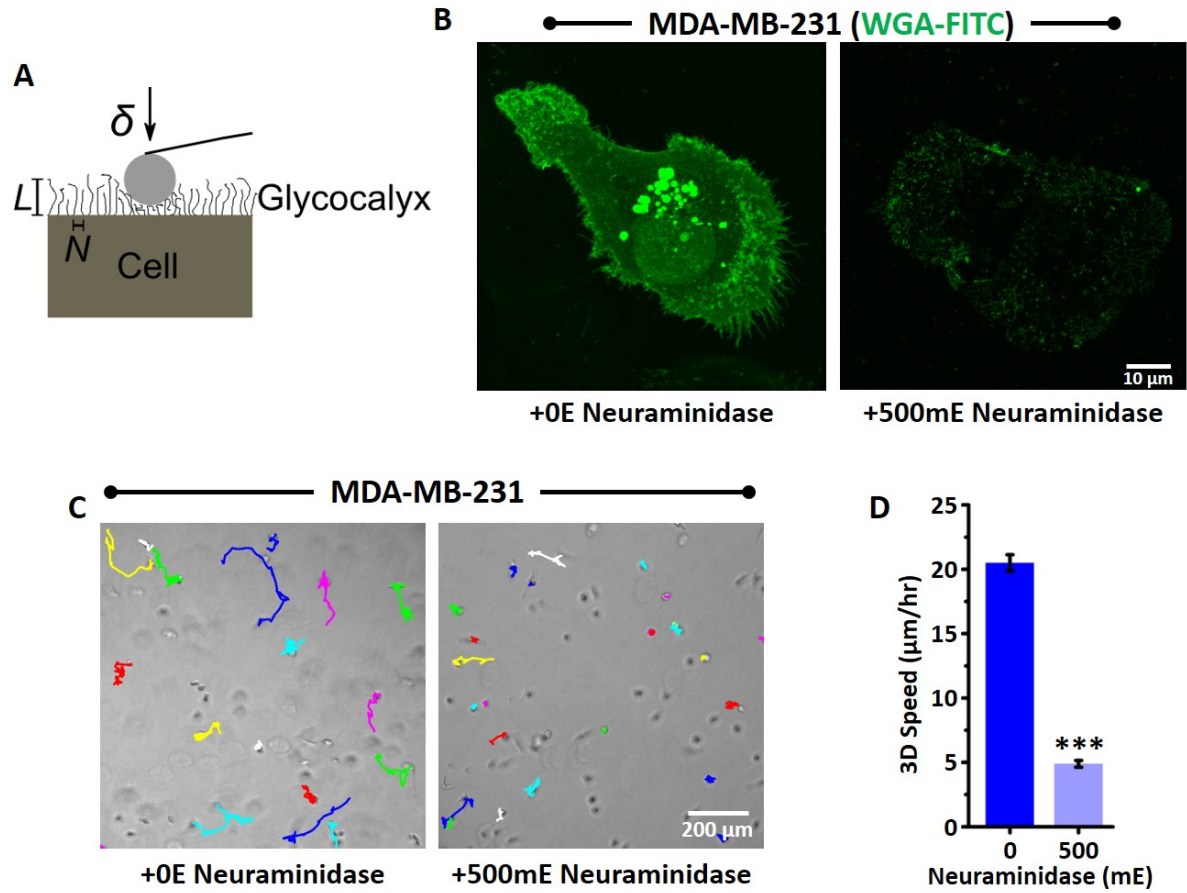


Figure 3.1: **Glycocalyx attached to plasma membrane of cells.** (A) Schematic of an AFM probe indenting a glycocalyx brush. (B) Enzymatic removal of cell surface glycocalyx. MDA-MB-231 Cells were treated with 0 and 500 milliunit (mE) neuraminidase for 3 h and was fixed and stained with WGA-FITC to visualize surface glycan. Images are representative confocal maximum intensity images. (C) Glycocalyx mediates invasiveness of MDA-M-231 cells. Invasion was checked after encapsulating cells in 3D collagen gels using live cell imaging. Figure shows 12 h migration trajectories. (D) Quantification of the cell migration trajectories over 12 h ($n > 120$ cells from 2 independent experiments, Statistical significance were determined using Mann-Whitney test, ***: $P < 0.001$).

finitely large cell. For a glycocalyx assumed to be comprised of polymer chains of nearly the same length, the force is given as (Dokukin et al., 2016):

$$F_{\text{single brush}} \approx 100k_B T R^* N^{3/2} e^{-\frac{2\pi h}{L}} L \quad (3.1)$$

where, k_B = Boltzmann constant ($1.38 \times 10^{-23} \text{ J.K}^{-1}$), T = temperature (298 K), $R^* = (R_{\text{probe}} \times$

$R_{cell})/(R_{probe} + R_{cell})$ with R_{cell} in our case $\rightarrow \infty$. Therefore, in our case $R^* \rightarrow R_{probe}$. N is the brush density, L is the length of brush and h is the distance between the indenter tip and cell body at the instant when the force is predicted. This predicted force is then equated to that predicted by the Hertz contact model, given by:

$$F_{Hertz} = \frac{4}{3}E^*R_{probe}^{1/2}\delta^{3/2} \quad (3.2)$$

where,

$$\frac{1}{E^*} = \frac{1 - \nu_{probe}^2}{E_{probe}} + \frac{1 - \nu_{glycocalyx}^2}{E_{glycocalyx}} \quad (3.3)$$

and δ is the indentation depth related to h as $\delta = 1 - h$. Assuming a fully compressive glycocalyx (that is, $\nu_{glycocalyx} = 0$) and $E_{probe} \rightarrow \infty$, we get $E^* = E_{glycocalyx}$. For a finitely thick glycocalyx layer on a semi-infinite cell, we use the correction proposed by Dimitriadis et al. (2002):

$$F_{corrected} = \frac{4}{3}E_{glycocalyx}R_{probe}^{1/2}(L - h)^{3/2}f(\chi) \quad (3.4)$$

where, $\chi = \frac{\sqrt{R\delta}}{L}$, and $f(\chi)$ is given as:

$$f(\chi) = \left[1 - \frac{2\alpha_0}{\pi}\chi + \frac{4\alpha_0^2}{\pi^2}\chi^2 - \frac{8}{\pi^3}\left(\alpha_0^3 + \frac{4\pi^2}{15}\beta_0\right)\chi^3 + \frac{16\alpha_0}{\pi^4}\left(\alpha_0^3 + \frac{3\pi^2}{5}\beta_0\right)\chi^4 \right] \quad (3.5)$$

Here, considering a glycocalyx layer bonded to the cell surface, α_0 and β_0 are given as:

$$\alpha_0 = -\frac{1.2876 - 1.4678\nu_{glycocalyx} + 1.3442\nu_{glycocalyx}^2}{1 - \nu_{glycocalyx}} \quad (3.6)$$

$$\beta_0 = \frac{0.6387 - 1.0277\nu_{glycocalyx} + 1.5164\nu_{glycocalyx}^2}{1 - \nu_{glycocalyx}} \quad (3.7)$$

For $\nu_{glycocalyx} = 0$, $\alpha_0 = -1.2876$ and $\beta_0 = 0.6387$. It is clearly visible that as glycocalyx thickness L increases with respect to indenter radius and indentation depth, χ decreases and

$F_{corrected} \rightarrow F_{Hertz}$ eventually. Therefore, equating Eq. 3.1 with Eq. 3.4, we get:

$$100k_B T R_{probe} N^{3/2} e^{-\frac{2\pi h}{L}} L = \frac{4}{3} E_{glycocalyx} R_{probe}^{1/2} (L-h)^{3/2} f(\chi) \quad (3.8)$$

Through Eq. 3.8 we can easily calculate the apparent glycocalyx stiffness $E_{glycocalyx}$ corresponding to N and L of a given polymer brush. Since the entropic brush formula (Eq. 3.1) is valid for $0.2 < h/L < 0.8$, we use the $E_{glycocalyx}$ corresponding to $h/L = 0.2$ as our initial glycocalyx stiffness in our further simulations (Fig. 3.2). We evaluate the brush equations at room temperature ($T = 298$ K).

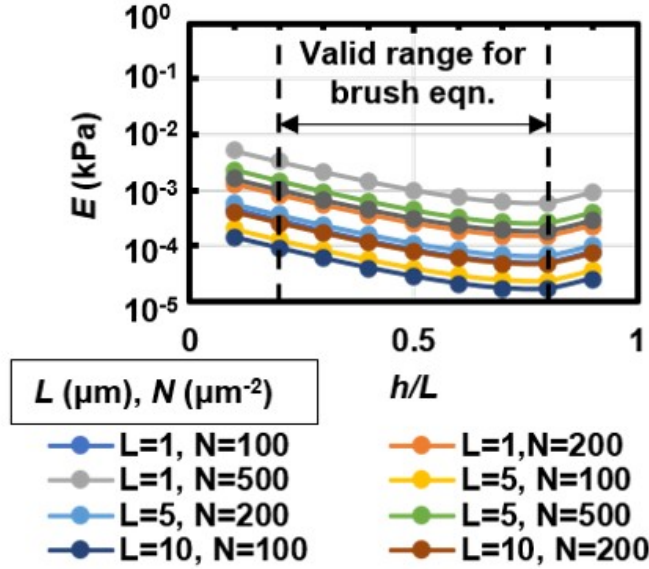


Figure 3.2: **Variation of brush stiffness E with glycocalyx thickness L , density N and indentation depth δ .** The units of L and N are μm and μm^{-2} respectively. The range of validity of the brush model by Dokukin et al. (2016) is also indicated by the dotted lines. The value of E taken in simulations corresponds to $h/L = 0.8$ (corresponding to a 20% indentation depth, or $\delta/L = 0.2$).

Dokukin et al. (2016) also formulated an expression for a double brush that consists of two different categories of brushes (with different brush sizes and densities, namely, L_1, L_2 and N_1, N_2 respectively). In such a scenario, the force due to this double brush could be predicted

as:

$$F_{double\ brush} \approx 100k_B T R_{probe} [N_1^{3/2} e^{-\frac{2\pi h}{L_1}} L_1 + N_2^{3/2} e^{-\frac{2\pi h}{L_2}} L_2] \quad (3.9)$$

Eq. 3.9 can then be equated with the corrected Hertz contact model in Eq. 3.4 to calculate the equivalent initial stiffness of the glycocalyx. As can be expected, the glycocalyx stiffness is very low as compared to general cell stiffness (by nearly O(2)) (Fig. 3.3).

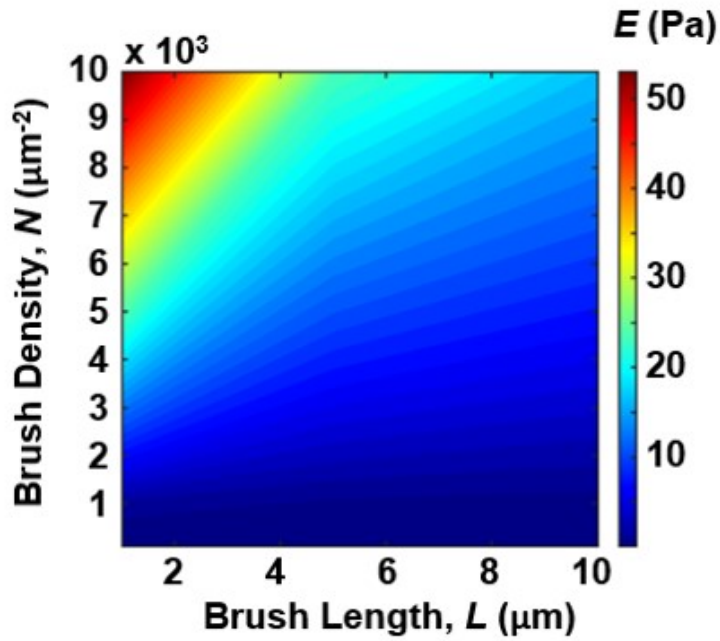


Figure 3.3: **Variation of brush stiffness E with glycocalyx thickness L , density N at indentation depth $h/L = 0.8$ or $\delta/L = 0.2$.** The units of L and N are μm and μm^{-2} respectively. The colorbar indicates the value of effective stiffness E , in Pa, calculated from the entropic brush model and the Hertz contact model.

Table 3.1: **Material parameters**

Component	Density (ρ) (kg/m ³)	Young's Modulus (E) (Pa)	Poisson's ratio (ν)
Cell	1050	500, 1800, 2000	0.5
ECM	1800	1000, 5000	0.5

3.2.2 Physical description of the modelling problem

Spherical indentation of glycocalyx

The glycocalyx is made up of brush polymers that lend it an effective stiffness under external stresses. This stiffness might be a result of combined effects of a finite persistence length and steric hindrance between the brush polymeric chains. AFM indentation studies of cells with glycopolymers attached to the cell membrane have shown that glycocalyx stiffness varies with its thickness (polymer length) and polymer density (Iyer et al., 2009; Dokukin et al., 2016). To simulate AFM indentation on cells with glycocalyx attached to the cell membrane, we created an axisymmetric FE model where the cell and its associated glycocalyx were assumed to very large compared to the spherical indenter to neglect edge effects (Fig. 3.4). The cell nucleus was assumed to not contribute significantly to the mechanics of indentation. The boundary conditions on the indenter in the cylindrical coordinate system were as follows: $u_z = 0$, at $t = 0s$, $u_z = 0.4L$, at $t = T$, and $u_r = 0$, for $t \rightarrow [0, T]$. The boundary conditions on the cell and glycocalyx taken together were: $u_r = 0$, for $r = 0$ and $t \rightarrow [0, T]$. Also, $u_z = u_r = 0$ for $z = 0$.

Compression of glycocalyx of cell sandwiched between rigid plate and ECM

Cells sitting sandwiched between the ECM and a rigid substrate, often an example of interfacial migration, can be found to push against the ECM (George et al., 2018). To simulate such

Table 3.2: **Stiffness dependence of Glycocalyx on L and N**

L (μm)	N (μm^{-2})	Equivalent E (Pa)
1	100	0.054
1	200	0.15
1	500	0.6
1	1000	1.7
1	10000	53.7
5	100	0.024
5	200	0.068
5	500	0.27
5	1000	0.757
5	10000	24
10	100	0.017
10	200	0.048
10	500	0.19
10	1000	0.536
10	10000	17

situations, we created FE models modulating the initial glycocalyx thickness L as 1 and 5 μm and cell spreading radius as 1 and 10 μm (Fig. 3.5). The cell nucleus was assumed to not play a significant mechanical role in these compression simulations and it was assumed that an aggregate cellular stiffness due to the effects of cytoskeleton, nucleus and other organelles would suffice. Experimental studies have shown that glycopolymers lead to clustering of integrin-

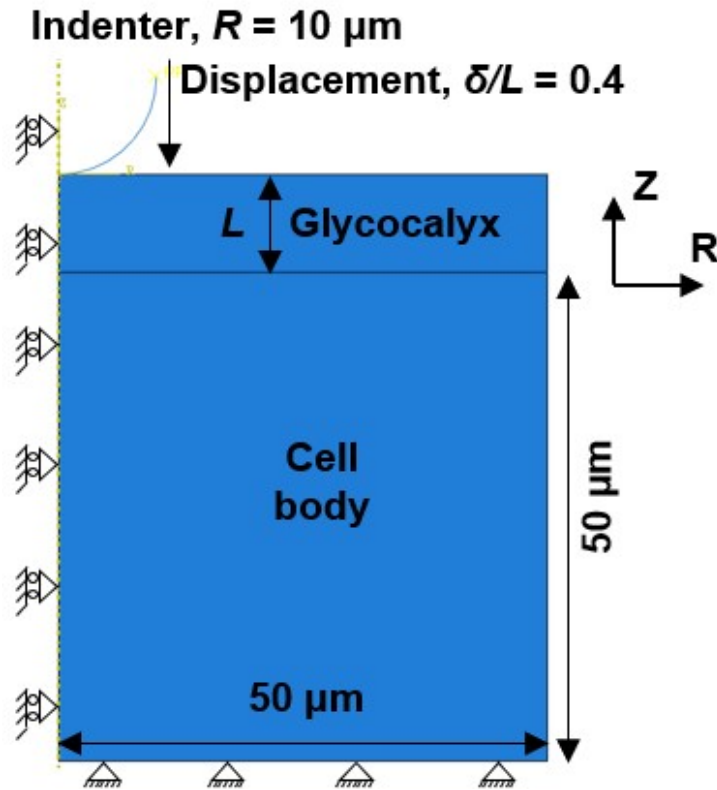


Figure 3.4: **Model schematics used for simulations of spherical indentation of a cell with glycocalyx surrounding it.** A rigid indenter of radius = $10 \mu\text{m}$ is displaced by 40% of initial glycocalyx thickness (L). The axis of symmetry, boundary conditions of the system and undeformed dimensions are shown. The axial and radial directions are denoted in the figure by Z and R respectively.

mediated focal adhesions that attach the cell to the underlying substrate (Paszek et al., 2014). In line with these experimental observations, the glycocalyx is absent in the region where the cell is attached to the rigid plate in our simulations. Moreover, the ECM was chosen to be large enough ($50 \times 50 \mu\text{m}^2$) as compared to the cell so as to mitigate any possible edge effects.

3.2.3 Finite Element Model

The finite element model used in this study was implemented in the commercial software ABAQUS. The mesh elements were chosen to be two-dimensional hybrid 4-node bilinear axisymmetric quadrilateral (CAX4RH) with reduced integration. The minimum elemental dimension in the mesh was chosen as $0.1 \mu\text{m}$. The glycocalyx was modelled as a compressible Neo

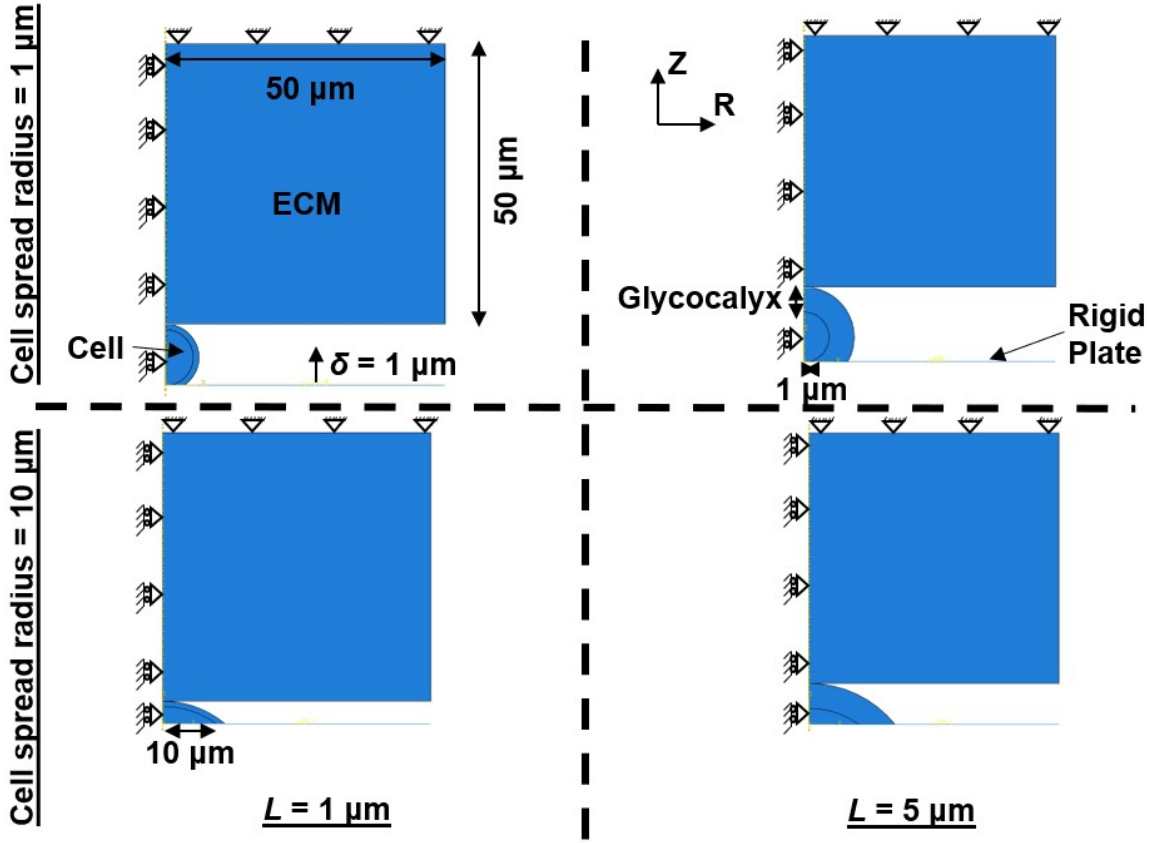


Figure 3.5: **Model schematics used for simulations of glyocalyx compression due to cells sandwiched between a rigid plate and ECM.** Two degrees of cell spreading area were studied, denoted by radii of $1 \mu\text{m}$ and $10 \mu\text{m}$ and the initial glyocalyx thickness was taken to be either $1 \mu\text{m}$ or $5 \mu\text{m}$. The rigid plate is displaced in the axial direction by $1 \mu\text{m}$. The axial and radial directions are denoted in the figure by Z and R respectively.

Hookean material, which can be written in terms of strain energy function Ψ as:

$$\Psi = C_1(I_1 - 3 - 2\ln J) + D_1(J - 1)^2 \quad (3.10)$$

where, C_1 and D_1 are material constants related to Lamé parameters μ and λ as $C_1 = \mu/2$ and $D_1 = \lambda/2$ respectively. I_1 is the 1st invariant or trace of the right Cauchy-Green deformation tensor, given by:

$$I_1 = \lambda_1^2 + \lambda_2^2 + \lambda_3^2 \quad (3.11)$$

and J is the determinant of deformation gradient, given by:

$$J = \lambda_1 \lambda_2 \lambda_3 \quad (3.12)$$

where, λ_1 , λ_2 and λ_3 are the principal stretches.

In the simulations for spherical indentation of glycocalyx, the lower edge of the cell body domain was constrained in all degrees of motion (encastered) as shown in Fig. 3.3. Due to the axisymmetric condition, only half of the full domain in 2D plane was modelled and symmetric boundary conditions were imposed on the domain. A maximum displacement of 40% of the initial glycocalyx thickness was applied on the rigid spherical indenter. Since the material model chosen is hyperelastic and therefore strain-independent, a total simulation time of 1 second was applied. The radial R and axial Z coordinates in the model in Fig. 3.4 correspond to X and Y coordinates in the 2D Cartesian coordinate system. Contact between the indenter and glycocalyx was assumed to be frictionless.

In the simulations for glycocalyx compression due to cells sandwiched between a rigid plate and ECM, the upper edge of the ECM domain was constrained in all degrees of motion (encastered) as shown in Fig. 3.5. Similar to Fig. 3.4, due to the axisymmetric condition, only half of the full domain in the 2D plane was modelled and symmetric boundary conditions in the cylindrical coordinate system were imposed on the domain. The cell in each condition was considered to be sandwiched between the ECM and a rigid plate and a maximum displacement of $1 \mu\text{m}$ was applied to the rigid plate. The cell volume was conserved in all cases and the cell spreading only affected the geometry of the sandwiched cell. The glycocalyx thickness was varied and contact between glycocalyx and ECM was assumed to be frictionless. The cell and glycocalyx were assumed to be attached at their lower surface to the rigid plate by the ‘tie’ condition.

3.3 Results

3.3.1 Magnitude and localization of maximum stresses change in cell body and glycocalyx with increasing glycocalyx thickness during spherical indentation

Indenting a Neo Hookean glycocalyx attached to an elastic cell body of effective stiffness $E_{cell} = 1.8$ kPa by a spherical indenter of $10 \mu\text{m}$ radius, we determined the evolution of von Mises stresses in the glycocalyx and the cell. We found that for a thin glycocalyx, that is, for $L = 1 \mu\text{m}$, stresses arising due to indentation are maximally localized to the cell body under the indenter (Fig. 3.6A). However, as we transition from a thin to a thick glycocalyx ($L = 1 \mu\text{m} \rightarrow 5 \mu\text{m} \rightarrow 10 \mu\text{m}$), a 40% indentation depth ($h/L = 0.4$) leads to a change in localization of maximal stresses from cell body (Fig. 3.6A) to the glycocalyx and cell being nearly equally stressed (Fig. 3.6B) and finally to the glycocalyx bearing most of it (Fig. 3.6C). Additionally, the von Mises stresses were found to increase with increase in polymer brush density N and decrease in polymer length L . These figures also demonstrate that stresses in the cell body decrease with glycocalyx thickness.

3.3.2 Evolution of indentation loads during spherical indentation of cellular glycocalyx

The evolution of indentation loads with indentation depth demonstrate a nonlinear dependence of load on indentation depth as shown in Fig. 3.7. The nonlinearity increases with increase in polymer or glycocalyx density N . Fig. 3.7 also shows that indentation loads have a greater dependence on glycocalyx density N rather than glycocalyx thickness L . This can be understood physically by the fact that closely attached fibres or brush impose greater steric hindrance for indenters of a finite size than sparsely distributed fibres. It is to be noted that the entropic brush equation that relates force and indentation depth for a certain L and N are valid beyond an indentation depth (δ/L) of 0.2 as shown by the green arrow in Fig. 3.7.

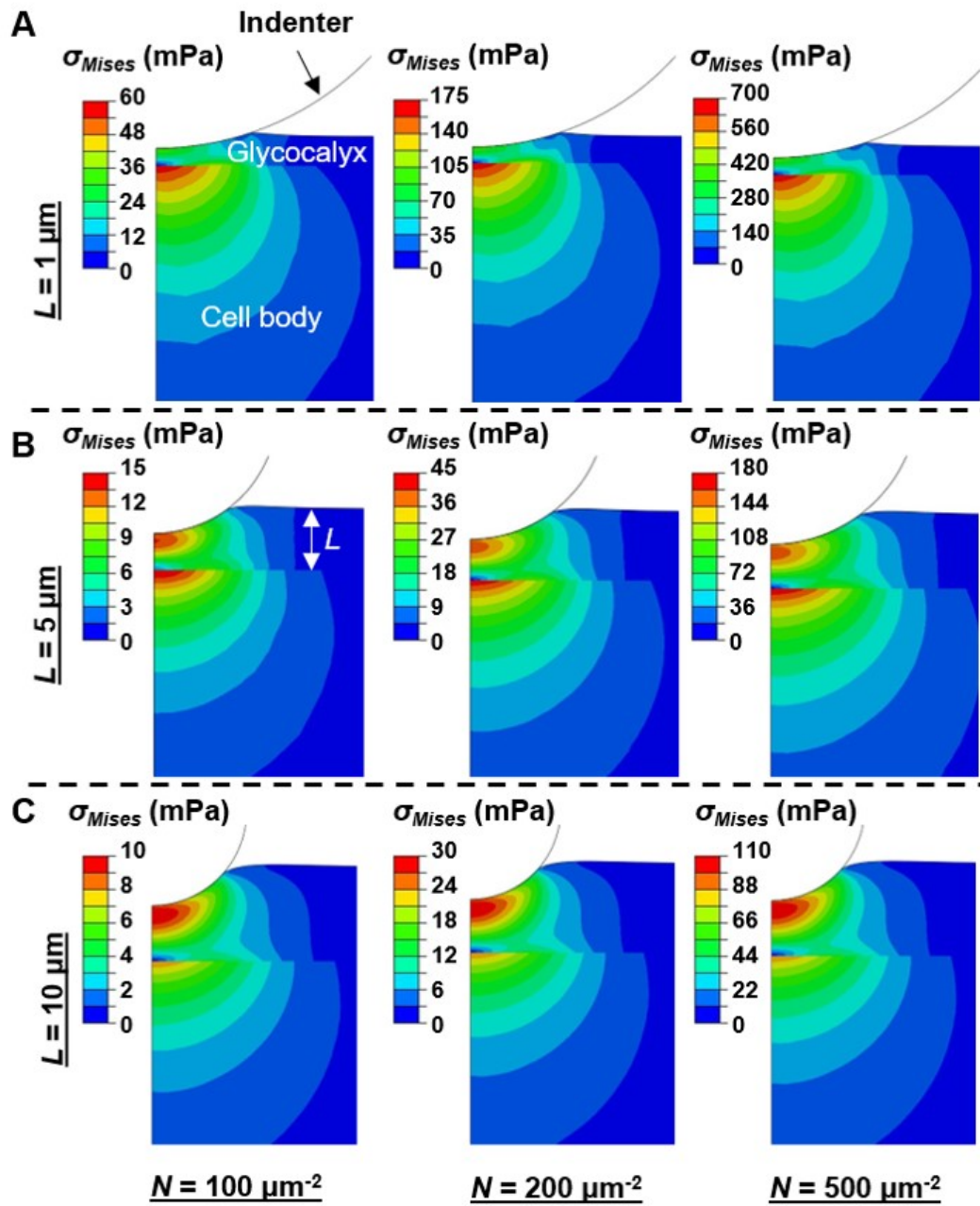


Figure 3.6: von Mises stress contours in cell body and cell glycoalyx for $N = \{100, 200, 500\} \mu\text{m}^{-2}$ and (A) $L = 1 \mu\text{m}$, (B) $L = 5 \mu\text{m}$, and (C) $L = 10 \mu\text{m}$. Maximum indentation depth δ/L is 0.4.

3.3.3 Compression of cellular glycoalyx against ECM

A thin glycoalyx ($L = 1 \mu\text{m}$) was found to be under larger stresses when cell and ECM were both stiff, that is, $E_{cell} = 2 \text{ kPa}$ and $E_{ECM} = 5 \text{ kPa}$ for $L = 1 \mu\text{m}$ and $N = 10,000 \mu\text{m}^{-2}$ and the

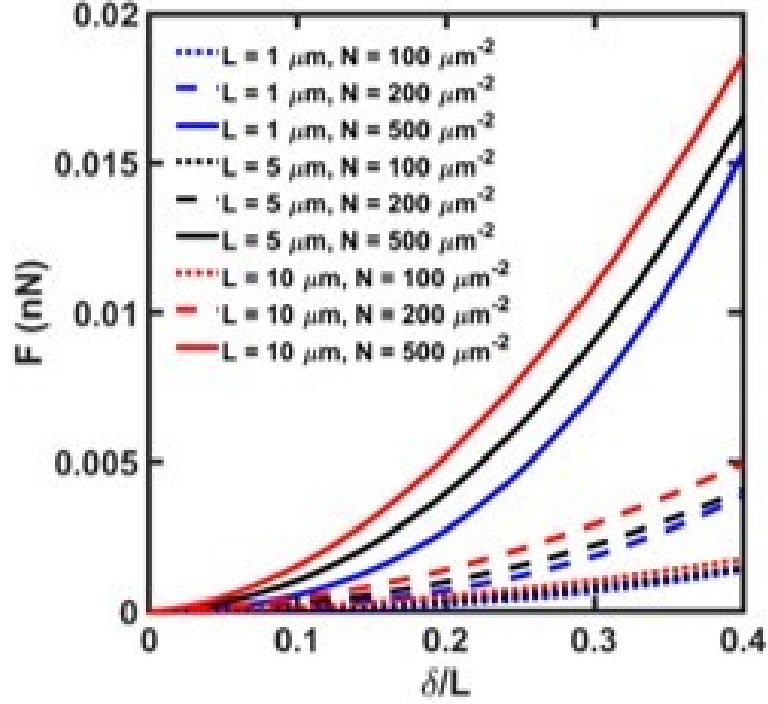


Figure 3.7: **Variation of normal indentation load F with relative indentation depth h/L for $L = \{1, 5, 10\} \mu\text{m}$ and $N = \{100, 200, 500\} \mu\text{m}^{-2}$.** Green dashed line and arrow mark the region beyond which the brush model is applicable. Maximum indentation depth δ/L is 0.4.

peak von Mises stress in this case was ≈ 3 -4 times greater than for $N = 1000 \mu\text{m}^{-2}$ (Fig. 3.8). A sparse glycocalyx ($N = 1000 \mu\text{m}^{-2}$) was also found to deform more than a dense one. Intra-cellular stresses increased with increase in E_{ECM} and were higher for $N = 10,000 \mu\text{m}^{-2}$ when compared to $N = 1000 \mu\text{m}^{-2}$ (≈ 4 times higher). Correspondingly, the deformation of cellular glycocalyx was found to decrease as N increased from 1000 to 10,000 μm^{-2} . This might indicate that a dense glycocalyx deforms the cell more than a sparse one.

A change of an order of $O(1)$ to $O(2)$ of magnitude of von Mises stresses was observed as N changed from 100 to 1000 μm^{-2} in all the four cases shown in Fig. 3.9. Interestingly, von Mises stresses along the axis of symmetry in a thin glycocalyx increase by an order $O(3)$ as compared to those in a thick glycocalyx. This was found to be true even if cells had the same spreading radii. Greater cell spread radius (10 μm) led to an increase in von Mises stresses in case of $N = 1000 \mu\text{m}^{-2}$ and $L = 1 \mu\text{m}$ when compared to more rounded cells. However, for a thick glycocalyx, cell spreading and cell and ECM stiffness did not have a significant effect on von Mises stresses. It was additionally found that contact force between the glycocalyx and ECM increased in a highly nonlinear manner with increase in glycocalyx compression depth

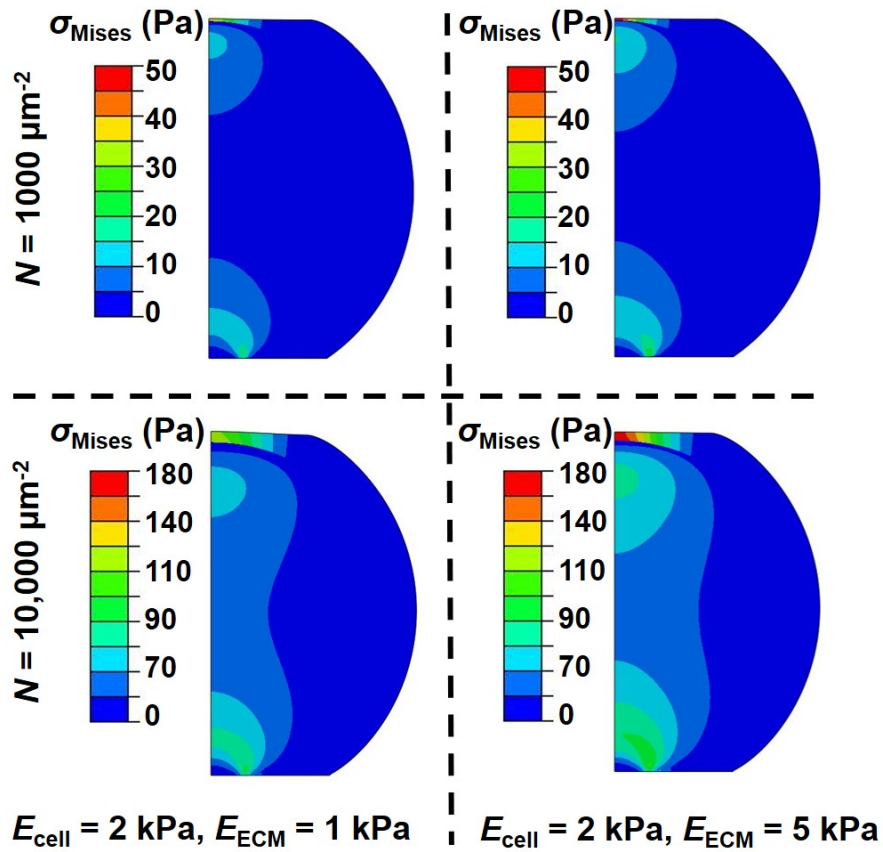


Figure 3.8: von Mises stress contours in cells along with the glycocalyx for $L = 1 \mu\text{m}$ and $N = \{1000, 10,000\} \mu\text{m}^{-2}$. Two combinations of E_{cell} and E_{ECM} are analyzed where $E_{cell} = 2 \text{ kPa}$ and $E_{ECM} = \{1, 5\} \text{ kPa}$ were used for the simulations. Colourbar depicts the von Mises stress.

(Fig. 3.10). Maximum contact forces were observed to be the highest when cell and ECM were both stiff (2 and 5 kPa respectively). It was also found that greater cell spreading led to greater contact force between the glycocalyx and the ECM for a thin glycocalyx. However, as in Fig. 3.9, for a thick glycocalyx, contact forces were found to depend only on N and not on cell or ECM stiffness. A thin glycocalyx ($L = 1 \mu\text{m}$) around the cell was found to result in an increase in maximum contact forces by an order of $O(2)$ greater than those in a thick glycocalyx ($L = 5 \mu\text{m}$) in case of a rounded cell and $O(3)$ in case of a spread cell.

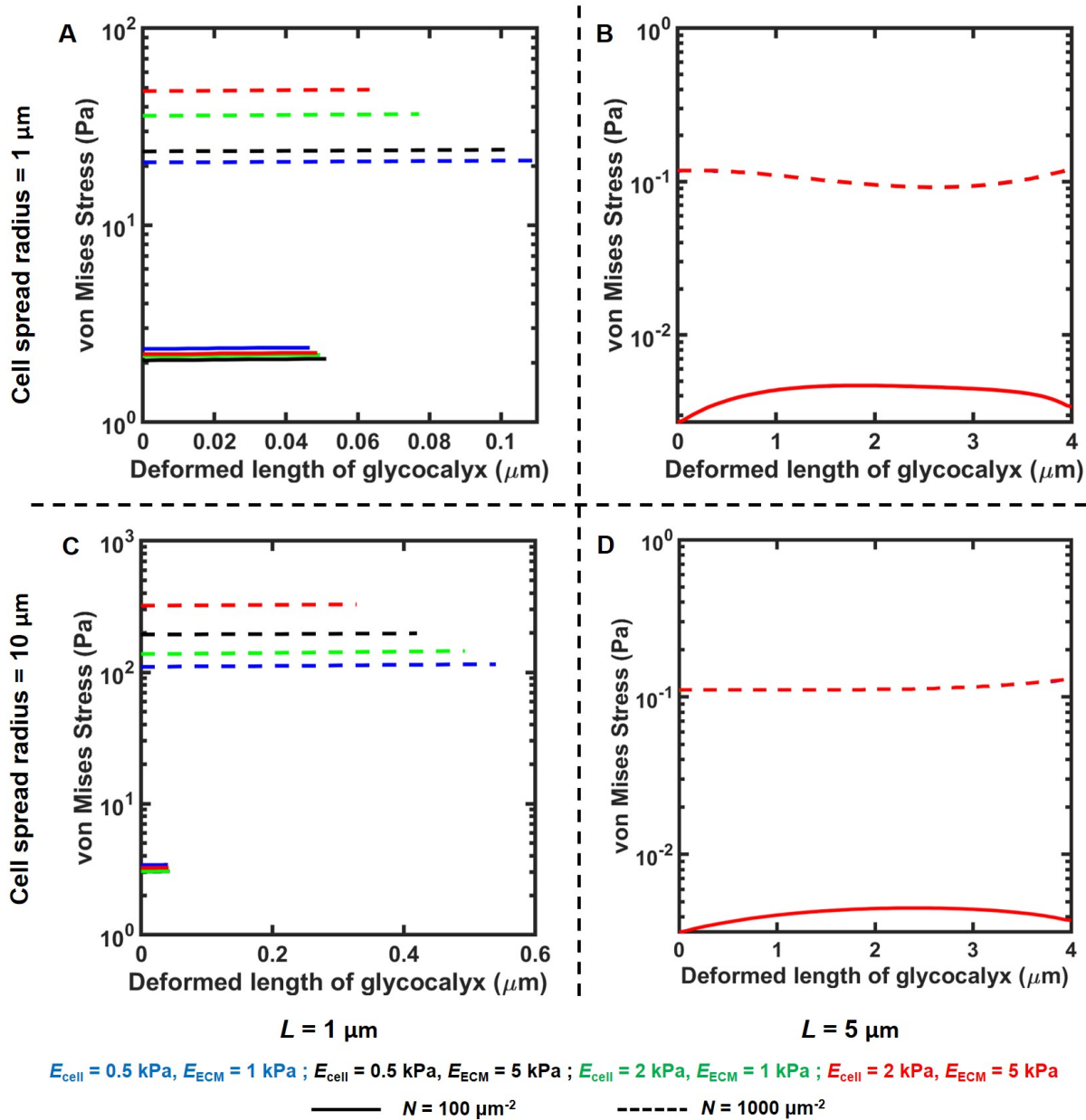


Figure 3.9: von Mises stresses in the deformed cellular glycocalyx along the axis of symmetry for: (A-D) $L = \{1, 5\} \mu\text{m}$ and $N = \{100, 1000\} \mu\text{m}^{-2}$. Various combinations of $E_{\text{cell}} = \{0.5, 2\} \text{ kPa}$ and $E_{\text{ECM}} = \{1, 5\} \text{ kPa}$ were used for the simulations.

3.3.4 ECM displacement due to compression of cellular glycocalyx against ECM

ECM displacement was found to increase with decrease in glycocalyx thickness and increase in spreading (Fig. 3.11). Additionally, ECM displacement also increased with increase in N

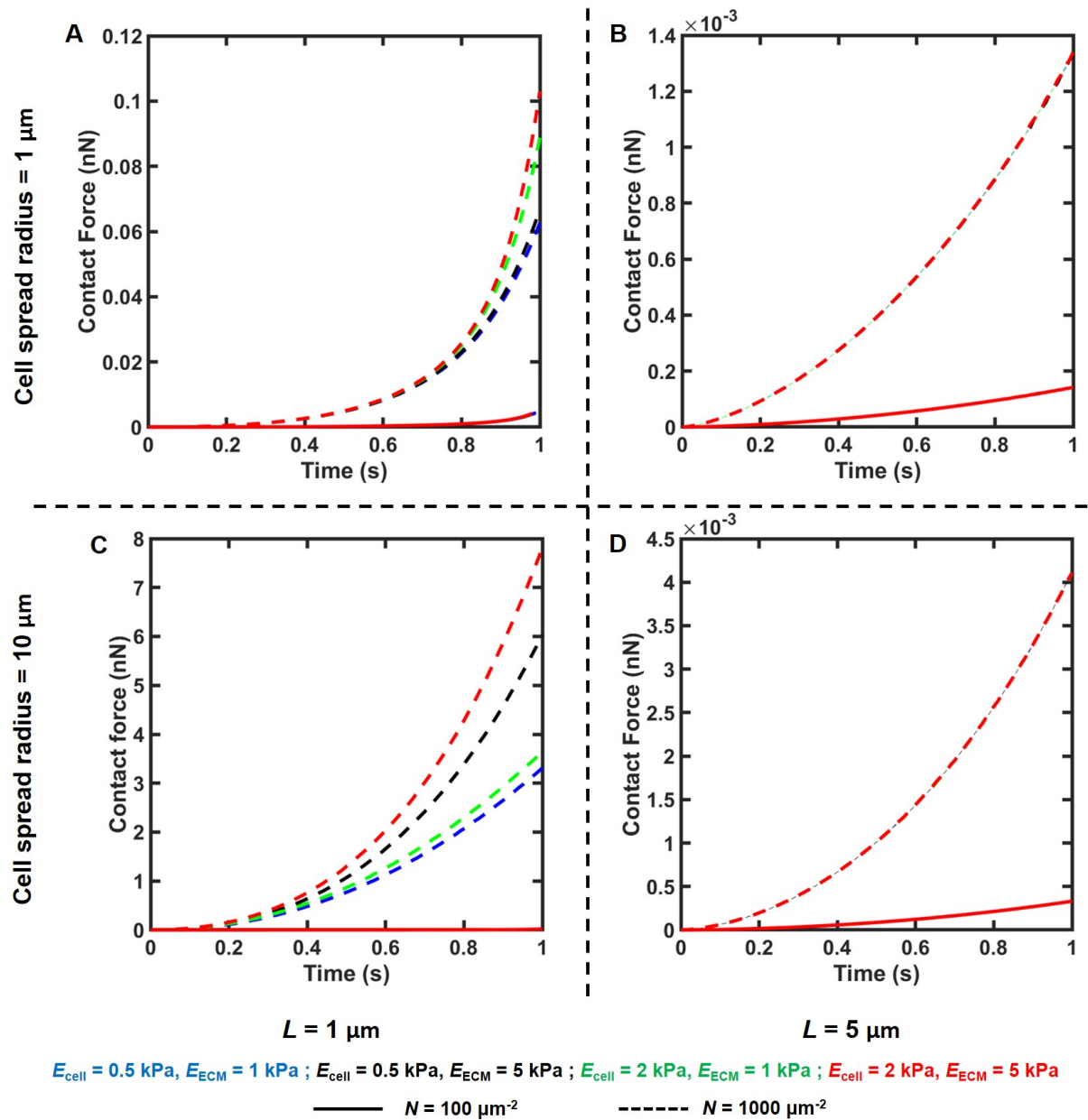


Figure 3.10: **Normal contact forces between the cellular glycocalyx and ECM** for: (A-D) $L = \{1, 5\} \mu\text{m}$ and $N = \{100, 1000\} \mu\text{m}^{-2}$. Various combinations of $E_{cell} = \{0.5, 2\}$ kPa and $E_{ECM} = \{1, 5\}$ kPa were used for the simulations.

and E_{cell}/E_{ECM} ratio. For thick glycocalyx, ECM displacement was found to depend only on N and E_{ECM} and not on E_{cell} , whereas, for $N = 1000 \mu\text{m}^{-2}$, ECM displacement increased with cell spread area for a thin glycocalyx by at least an order $O(1)$. There was a difference of up to an order $O(3)$ between the peak ECM displacement for a thin versus a thick glycocalyx for the same spread area. However, such a large difference was not observed between a thin and a thick glycocalyx for more rounded cells.

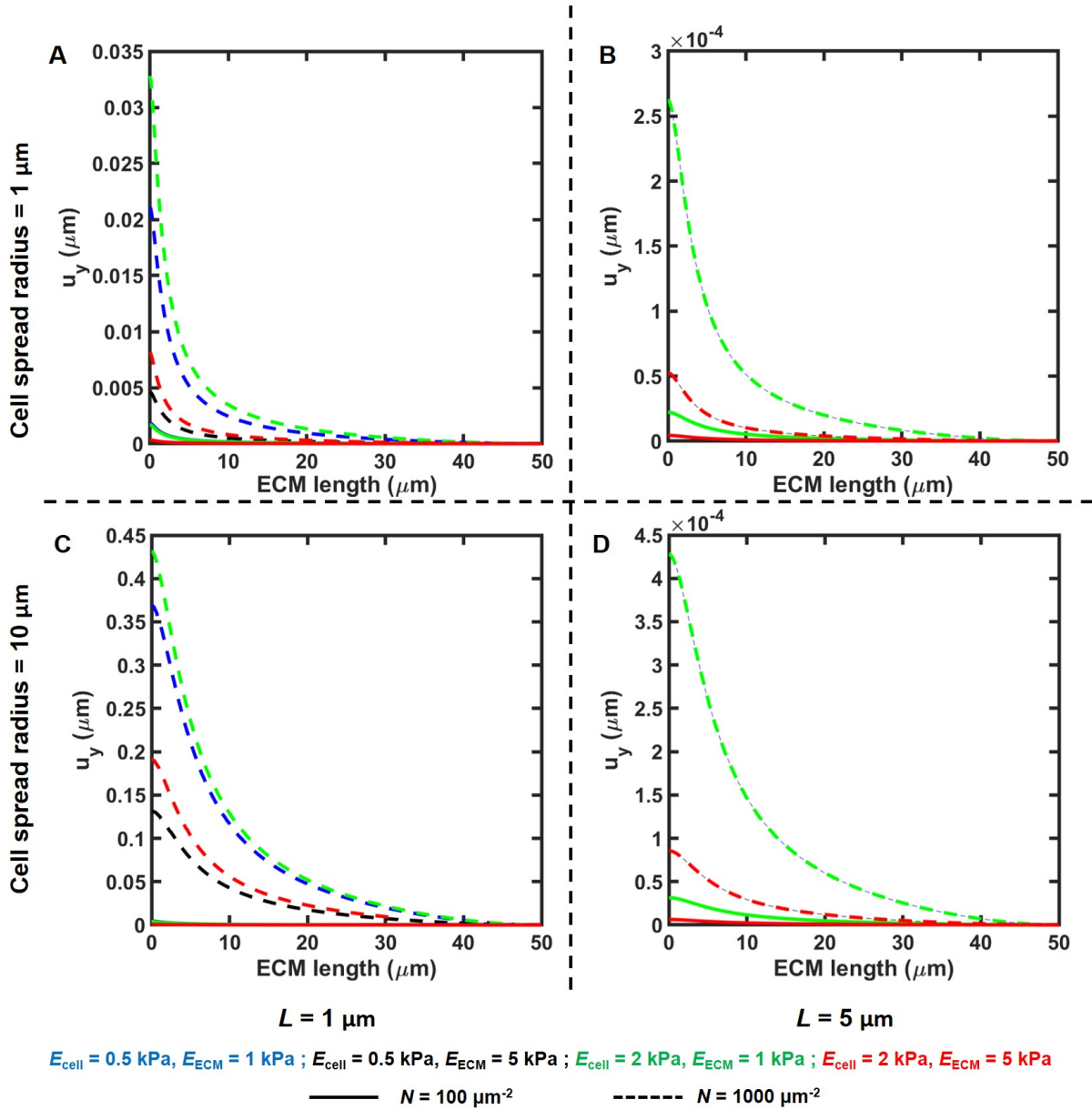


Figure 3.11: **ECM axial displacement along the axis of symmetry** for: (A-D) $L = \{1, 5\} \mu\text{m}$ and $N = \{100, 1000\} \mu\text{m}^{-2}$. Various combinations of $E_{\text{cell}} = \{0.5, 2\}$ kPa and $E_{\text{ECM}} = \{1, 5\}$ kPa were used for the simulations.

For a highly dense glycocalyx ($N = 10,000 \mu\text{m}^{-2}$), more rounded cells were found to impose largely localized ECM displacement (Fig. 3.12). Peak ECM displacement was also found to increase with decrease in brush thickness. Moreover, the peak ECM displacement in spread cells was ≈ 2 times greater than in rounded cells.

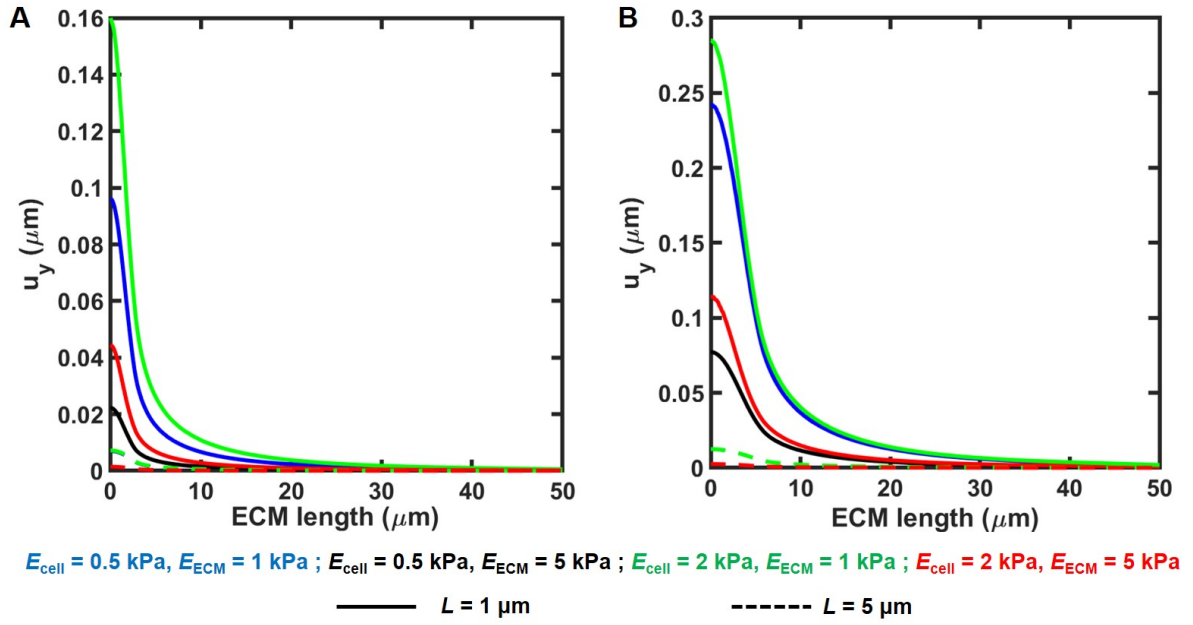


Figure 3.12: **ECM displacement due to a sandwiched cell for $L = \{1, 5\} \mu\text{m}$ and $N = 10,000 \mu\text{m}^{-2}$.** (A) ECM displacement in +y-direction along the contact surface (longitudinal direction) of ECM and cell for a cell spread radius of $1 \mu\text{m}$. (B) ECM displacement in +y-direction along the contact surface (longitudinal direction) of ECM and cell for a cell spread radius of $10 \mu\text{m}$. Various combinations of $E_{cell} = \{0.5, 2\} \text{ kPa}$ and $E_{ECM} = \{1, 5\} \text{ kPa}$ were used for the simulations. Solid curves indicate $L = 1 \mu\text{m}$ and dashed curves indicate $L = 5 \mu\text{m}$.

3.3.5 Mechanical implications of glycocalyx as a double brush

Dokukin et al. (2016) suggest that the cellular glycocalyx is made up of at least two different lengths and densities of polymer brushes and the force due to this double brush polymer can be predicted by Eq. 3.9. Thus, using Eq. 3.4 and Eq. 3.9 we calculated the corresponding glycocalyx stiffness. We used the values $L_1 = 1 \mu\text{m}$, $L_2 = 5 \mu\text{m}$ and $N_1 = 10,000 \mu\text{m}^{-2}$, $N_2 = 1000 \mu\text{m}^{-2}$ thus assuming that short brushes are densely attached to the cell membrane, whereas, long brushes are sparsely distributed.

Our results show that the contact force between the cellular glycocalyx and the ECM depends only on cell spreading as evidenced by the fact that all dotted curves and all solid curves overlap (Fig. 3.13A). Moreover, similar to Fig. 3.12, ECM displacement varies only with E_{ECM} and cell spreading (Figs. 3.13B, C).

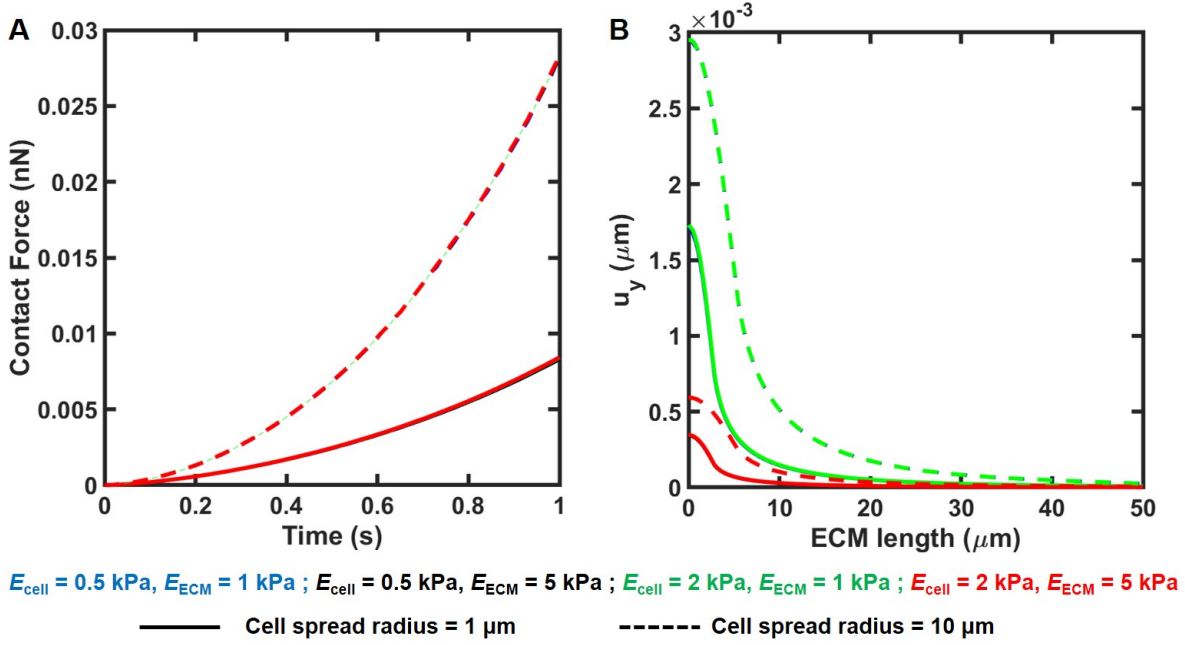


Figure 3.13: **Mechanical implications of glycocalyx as a double brush.** (A) Contact force between the glycocalyx and ECM, and (B) ECM vertical displacement u_y along its entire length, for $\{L_1, L_2\} = \{1, 5\} \mu\text{m}$ and $\{N_1, N_2\} = \{10,000, 1000\} \mu\text{m}^{-2}$. Dotted curves represent a cell spread radius of $10 \mu\text{m}$ and solid curves represent a cell spread radius of $1 \mu\text{m}$. Various combinations of $E_{\text{cell}} = \{0.5, 2\} \text{ kPa}$ and $E_{\text{ECM}} = \{1, 5\} \text{ kPa}$ were used for the simulations.

3.4 Discussion

The numerical model presented in this study considers the glycocalyx to be a continuum where its mechanical properties can be defined by the aggregated brush stiffness and resistance to indentation or compression provided by steric hindrance. Here it must be noted that we consider that the individual glycopolymer strands along with their sidechains are close enough and the polymer brush is dense enough to be considered as a continuum. Moreover, we choose to simplify the mechanical behaviour of the glycocalyx by choosing it to be a Neo Hookean hyperelastic material rather than a poroelastic material with fluid flow under stress. In our model, we do not consider flow of solvent molecules under stress due to lack of comprehensive experimental data on the stress-strain relationships of the glycocalyx brush. Also, on account of these glycopolymers having contour lengths ($0.1 - 5 \mu\text{m}$) much longer than their persistence lengths ($5 - 10 \text{ nm}$), they frequently behave as randomly coiled flexible chains (Kuo et al.,

2018). These chains can assume random configurations and orientations without a preferred direction, and therefore, we consider the entire glycocalyx as isotropic and homogeneous.

To calculate the initial stiffness of glycocalyx brush, we equate the forces predicted by the entropic brush model for single and double brush and equate these to those provided by the Hertz contact model for an indentation depth δ/L of 0.2. Additionally, by virtue of the glycocalyx proteins like mucins with their glycan sidechains being brush-like polymers, we also assume the glycocalyx as a whole to be fully compressible ($\nu = 0$). To further account for nonlinear deformations of the glycocalyx, we consider it to be Neo-Hookean hyperelastic.

Our experimental results show that the cellular glycocalyx facilitates cell migration in 3D. Additionally, cancer cells have been shown to secrete higher levels of hyaluronic acid and glycoproteins. This is also manifested in thicker glycocalyx coats around cancer cells. Coupled with the fact that greater glycocalyx concentration on the cell membrane of metastatic cancer cells also led to cell rounding (by reducing integrin-based adhesions), there is a high probability that glycocalyx has a significant mechanical influence on cancer cell migration. However, the significance of the mechanical aspect of the glycocalyx has not been adequately studied in previous literature. We hypothesized that the glycocalyx acts as a polymer brush to cushion the cell against extracellular stresses as well as help the cell squeeze through confinement.

To elucidate the mechanical implications of the cellular glycocalyx, we simulated two cases of extracellular stresses imposed on it. Firstly, we considered a rigid indenter (an AFM probe) indenting the glycocalyx and the cell underneath. Secondly, we considered a situation where the cell along with its associated glycocalyx compresses itself against an ECM. Interestingly, we found that a thick glycocalyx cushions the cell underneath it from extracellular stresses, that is, maximal stresses develop in the glycocalyx rather than the cell body as the thickness increases. Moreover, the peak stresses in the system decrease as the glycocalyx thickness increases. These observations are accompanied with the finding that a dense glycocalyx results in greater contact forces between the indenter and glycocalyx than a sparse glycocalyx, irrespective of its thickness. This supports our initial hypothesis and suggests that a thick glycocalyx, such as that around a highly metastatic cancer cell might facilitate cell migration through mechanically hostile and confined environments. Analyzing the results of compression of cell against the ECM matrix, we find that building up on our indentation studies, for a certain glycocalyx thickness, increased glycopolymer density leads to greater ECM deformation (less

glycocalyx deformation) and greater stresses in the glycocalyx. The increase in peak stresses within a thin glycocalyx is not only a function of glycopolymer density, but also a function of cell spreading and cell and ECM stiffness. However, surprisingly, for a thick glycocalyx there was no variation in peak stresses with change in any of the above parameters. Moreover, stresses were much less than in a thin glycocalyx. Similar trends were found to be true in case of contact forces and ECM displacements as well. All of these point to the possibility that a thick glycocalyx is mechanically beneficial for a cell migrating through confined environment or under large external stresses imposed on it, for instance, during intravasation or extravasation through blood vessel epithelia during metastasis. However, it must be noted that the stresses inside the glycocalyx or the contact forces or the ECM displacement due to the glycocalyx in this study were relatively less as compared to the cellular or nuclear stresses that a migrating cell without a glycocalyx as proposed in Chapter 2 has to endure. Incorporating a glycocalyx on top of a cell therefore leads to a reduction in cellular stresses.

3.5 Conclusion

In conclusion, we developed axisymmetric models of cells with glycocalyx attached to their plasma membrane indented by a rigid probe to simulate AFM indentation. Additionally, we developed axisymmetric models of glycocalyx-mediated compression of cells sandwiched between ECM and a rigid plate. Approximating the glycocalyx as a continuum and defining its material properties based on a brush model, our simulation results demonstrate the efficacy of such a glycocalyx in acting as a buffer or shock-absorber for a cell against external stresses. The efficacy of the glycocalyx as a buffer depends on its thickness and density. These results are validated by experiments from the literature which indicate that the metastatic potential of cancer cells is positively correlated to the glycocalyx thickness and density.

Chapter 4

Detection of tumor nodule embedded inside healthy tissue

Note: This chapter has been modified from the following manuscript: Mukherjee A, Gupta A, Sen S, Yan W, Saigal A, Singh R K, "Palpation sensitivity of an embedded nodule using the finite element method", *Under Review*

4.1 Introduction

Palpation is the method of probing and feeling an object to gain more insight into its mechanical properties. A physician or surgeon palpates a tissue to detect an embedded nodule and to estimate its mechanical properties relative to the surrounding tissue based on the judgment of contact forces and apparent tissue stiffness (Howe et al., 1995). With the emergence of advanced imaging methods like magnetic resonance imaging (MRI), computed tomography (CT) and ultrasound a few decades ago, it has become much easier to detect stiff and dense nodules embedded in tissues. Once the tumor is located and images generated, surgeons proceed with tumor removal using 2D scan images. This is a major clinical challenge as the surgeons do not usually have the luxury of a simultaneous MRI or CT procedure being done to locate the tumor in real-time. Therefore, in such cases the surgeon must feel the tumor embedded in the tissue either with their fingers or with a surgical tool.

Palpation is done to sense stiff nodules in the breast, liver, pancreas, stomach and other tissues. Palpation for tumors in laparoscopic or minimally invasive surgeries require the surgeon to feel the nodule using a surgical tool, a process which isolates the sense of touch that surgeons rely on. It is therefore desired that the detection and localization of a tumor through palpation

be as accurate as possible. With the advent of robotic surgery, these laparoscopic procedures are executed by robotic instruments that are controlled remotely by a surgeon. A major limitation to the currently available robotic surgery instruments is that they are unable to transmit the forces that their end-effectors experience during a surgical procedure. As a result, the surgeon is unable to perceive the encountered forces. The problem of efficient nodule detection is important from a robotics and healthcare point of view.

Contact models have traditionally been used to quantify the mechanical characteristics of various materials. Sneddon (1965) developed an analytical expression for the force applied on an indenter of general shape to indent a substrate by a desired amount. Hayes et al. (1972) found that a non-linear relationship exists between indentation depth and load applied when indenting a cartilage tissue using a spherical indenter. Their results indicate that the indentation depth for any given load is less when applied with a large radius indenter than when applied with a small radius indenter. Conversely, it implies that for a given indentation depth, the applied load would be higher for an indenter with a large radius. A study by Konstantinova et al. (2017) has suggested that a minimal contact area for measurement is desirable for achieving accurate measurements from an inhomogeneous material during palpation. Spherical indentations were investigated using four of the most commonly used hyperelastic models (Fung, Mooney-Rivlin, Neo-Hookean and Arruda-Boyce models) by Zhang et al. (2014). They proposed a method based on dimensional analysis, Hertz formulation and finite element simulations to establish a relationship between material properties of biological tissues and indentation responses. Although the Hertz contact model is arguably the most popular method to quantify material properties and is applicable for hard materials, its applicability to soft materials that deform easily is debatable.

Previous palpation or indentation studies on soft materials/ tissues have typically utilized the Hertz contact formulation and based their predictions of tissue material properties on this formulation (Konstantinova et al., 2013, 2017). However, this formulation is applicable only in homogeneous elastic materials for very small deformations, which cannot be assumed in soft tissues with embedded cancerous nodules. Moreover, most tissues are anisotropic, with orientation-dependent mechanical properties that make the application of the Hertz contact formulation erroneous. Therefore, there is a need to comprehensively study indentation/ palpation mechanics in heterogeneous soft tissues with embedded nodules with and without anisotropic

material characteristics.

Indentation has been widely studied in literature to gain insight into the correlation of indentation depth, applied load, material hardness and contact area of indenter. However, such correlations have not been studied extensively in cases where a relatively stiff nodule ($5 \leq G_n/G_0 \leq 15$) is embedded inside a tissue of finite thickness thus rendering the system inhomogeneous. Here, G_n and G_0 are the shear stiffnesses of nodule and tissue respectively. In addition, most of the studies reported in the literature are specific to the tissue and nodule properties used in the simulation. Hence, a non-dimensional study which is valid for a wide of range of tissues and nodule properties is imperative.

This study develops a computational model of indentation with a hemispherical indenter to relate the physical and material properties of an embedded nodule to the indentation load. Such relations would be beneficial to predict the location and properties of embedded nodules with unknown properties. The developed model has been compared with the Hertzian contact model and also benchmarked against the experimental results reported in the literature (Zhang et al., 2014). Based on the validated finite element model, correlations have been developed between non-dimensional force and ability of a robotic probe to detect an embedded nodule in a soft tissue and identify regimes of possible nodule detection. Palpation sensitivity, defined as the difference between indentation load in presence and that in absence of an embedded nodule is determined based on which nodule detection regimes are plotted. Additionally, the effect of anisotropic material properties on embedded nodule detection has been assessed by analyzing the effect of fiber dispersion on indentation loads and consequent stress evolution in tissue and nodule.

4.2 Materials and Methods

An axisymmetric model of indentation was developed to simulate a condition where a tumor nodule is embedded inside an otherwise healthy tissue (Fig. 4.1). The motivation for developing this model was to analyze the detectability (palpation sensitivity) of such an embedded nodule using laparoscopic instrumented probes. The developed model (homogeneous tissue) was validated with experimental results from Zhang et al. (2014) and also compared with Hertzian

contact model predictions.

An embedded tumor was then incorporated in our simulations and indentation loads were computed for two cases, namely, Case I: without the embedded nodule, and Case II: with the embedded nodule. Loads on the indenter were then compared for these two cases and the effects of the contrast of shear moduli of nodule versus tissue, nodule size and position and indentation depth were determined. Fig. 4.1 demonstrates the modelling process flow in this work. Dimensional analysis was used to generate predictive relationships between indentation load and physical characteristics of the embedded nodule and palpations sensitivity maps were constructed to determine regimes of nodule detectability. This model might be helpful in predicting location of an embedded cancer nodule in any organ provided the material parameters of the healthy tissue are known.

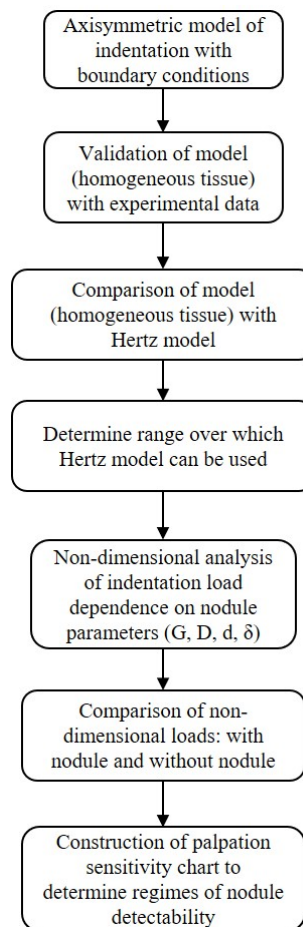


Figure 4.1: **Flowchart of the modelling process.**

4.2.1 Physical description of the modelling problem

Laparoscopic surgical procedures are performed on organs that remain constrained in their original environment, for instance, the liver sits on top of the rib-cage and spine. Therefore, we created our model such that it simulates indentation of such organs under boundary conditions that mimic their native environment. In our simulations, a spherical indentation probe of radius R was displaced downwards by a predefined amount (δ) along the axis of symmetry and the resultant contact forces (F), which were a function of nodule stiffness (G_n) along with its diameter (D) and depth (d), were quantified (Fig. 4.2). The tissue was assumed to be of a finite thickness (h) with a rigid underlying substrate that was used to simulate hard bone underneath soft tissues (Fig. 4.3). The indentation depth was defined to be 0.5, 1 and 2 mm for tissue thickness of $h = 10, 20$ and 50 mm. The indenter was chosen to have a spherical tip (Figs. 4.2 and 4.3) as it is unaffected by edge effects that occur in flat cylindrical indenters and to better resemble a human finger during palpation exercises. Furthermore, a curved surface conforms to the indented tissue surface more than a flat cylindrical surface. Moreover, the nonlinearity of responses due to this profile are lesser than conical or pyramidal indenters (Valero et al., 2016). Two types of indenters were used in simulations (thin and thick) corresponding to radii of 3 and 5 mm respectively. Laparoscopic instruments used in minimally-invasive surgical procedures generally have diameters ranging from 3 mm to 30 mm so that they fit inside the trocars. Among these, instruments with diameters of 5 mm, 6 mm and 10 mm are the most common. The tissue width was determined such that it was > 5 times the indenter radius to minimize edge effects. Nodules of diameters in the range 0.5 to 6 mm were simulated (1 nodule per condition) to lie along the axis of symmetry at a depth that was in the range 0.1 to 3.5 mm.

4.2.2 Numerical formulation

The finite element model used in this study was implemented using the commercial software ABAQUS. Hybrid or mixed-formulation elements were employed to mesh the incompressible soft tissues. Two-dimensional hybrid 4-node bilinear axisymmetric quadrilateral (CAX4H) stress elements were used in this study as opposed to two-dimensional plane stress elements

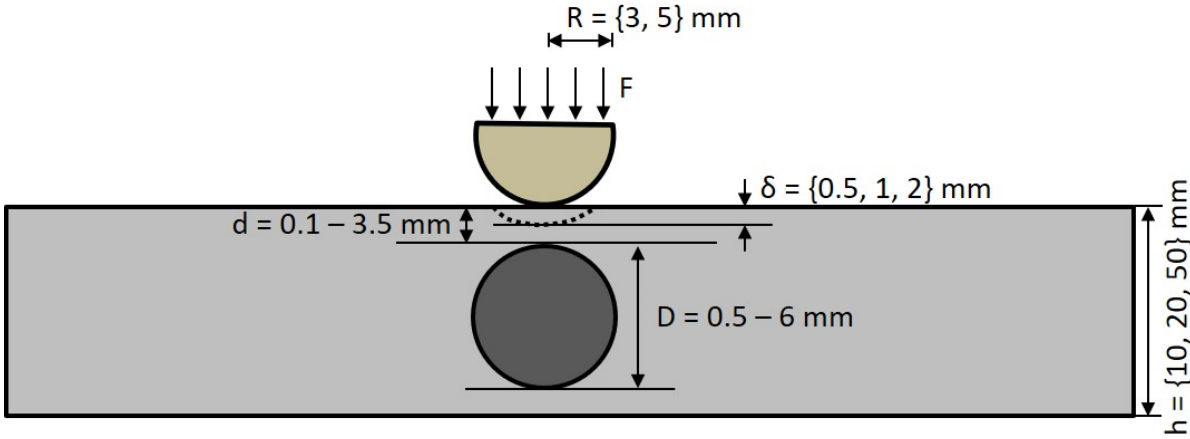


Figure 4.2: **A cross-sectional schematic of indentation of a soft tissue with an embedded nodule.** The indenter of radius R is hemispherical and nodule of diameter D and depth d is spherical. The nodule is embedded in a tissue of finite thickness h . A prescribed indentation depth δ leads to the generation of an indentation load F .

used by Sangpradit et al. (2009) and Konstantinova et al. (2017). Plane stress formulation neglects the out-of-plane stresses and are thus incapable of mimicking the physics of the indentation process. Axisymmetric models therefore are more capable of closely mimicking indentation physics. Nodules of various sizes (diameter D ranging from 0.5 to 6 mm) were assumed to be embedded at various depths (d) along the axis of symmetry. A mesh convergence analysis based on von Mises stress under the indenter was done, and it was determined that a minimum element dimension of 0.1 mm was sufficient to model the system. The total number of elements in the model were around 4750.

4.2.3 Loading and boundary conditions

Indentation generally assumes that the diameter of the indenter tip is very small relative to the width of the substrate and that the indentation depth to substrate thickness $\delta/h \ll 1$. In the axisymmetric model used in our simulations, the axis of the indenter is perpendicular to the tissue surface and coaxial with the diameter of the nodule (Fig. 4.3). The boundary conditions of the model in the Cartesian coordinate system are as follows: $u_x = 0$ at $x = 0$, $u_y = 0$ at $y = 0$ for the tissue, and $u_y = 0$ at $t = 0$, and $u_y = -\delta$ at $t = T$ for the indenter. The cylindrical coordinate system (r, Z, θ) is equivalent to the Cartesian coordinate system (x, y, z) at $\theta = 0$. Therefore, x

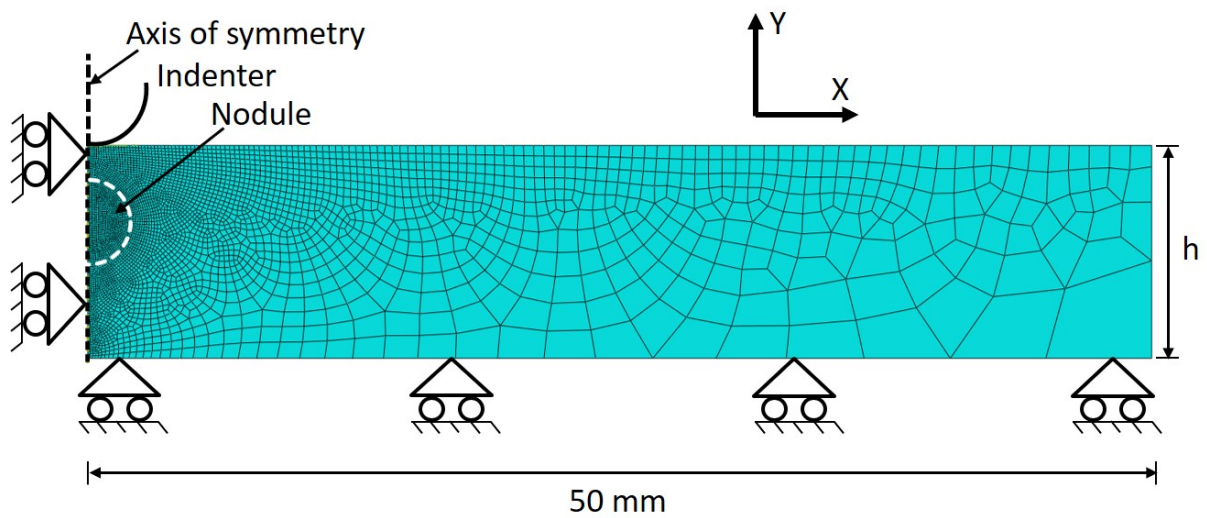


Figure 4.3: A representative finite element model depicting the axisymmetric setup where the indenter is displaced downwards (-y direction) along the axis of symmetry. Boundary conditions are also marked. Radial and axial directions are denoted by x-axis and y-axis respectively.

and y correspond to r and Z in the cylindrical coordinate system. This mimics tissues such as muscles resting on hard bones or visceral organs like liver and pancreas resting on the ribs. Indentation depths of 0.5, 1.0 and 2.0 mm corresponding to $\delta/h = 0.05, 0.1$ and 0.2 respectively for a tissue thickness of 10 mm, are applied. The model is based upon contact and indentation studies done by Lebedev and Ufliand (1958), Hayes et al. (1972) and Costa and Yin (1999). The studies by Hayes et al. (1972) and Costa and Yin (1999) considered the tissue to be a finite elastic space instead of considering the tissue to be semi-infinite. The contact between indenter and tissue is considered to be frictionless and hard contact as we do not consider adhesion of tissue and indenter surfaces.

4.2.4 Material model

The properties of a material are ultimately a function of its microstructure and rheology and therefore, should be modeled to include such effects. However, a coarse-grained approximation of the microstructural properties can be found to suffice while describing tissue-level material properties if the chosen material model sufficiently accounts for the macroscopic manifestation

of the microstructural properties.

Arruda-Boyce hyperelastic model

In this study, we use an Arruda-Boyce hyperelastic model to describe tissue deformation behavior due to its physical macromolecular basis as it incorporates the mechanics of polymer chains (Arruda and Boyce, 1993). It has been previously validated and implemented by several indentation studies on soft tissues (Liu et al., 2004; Sangpradit et al., 2009; Zhang et al., 2014; Pan et al., 2016). Moreover, although there are several other hyperelastic models available, such as: Neo-Hookean, Mooney-Rivlin, Ogden and Fung, there is no clear consensus in the literature regarding the suitability of a particular hyperelastic model for soft tissue simulations. We do not account for viscous effects in our model as the indentation process we consider in our study lasts for timescales ($\approx 1 - 2$ seconds) less than viscoelastic timescales (> 10 seconds). Thus, we consider the materials used in this study to be strain-rate independent for short timescales.

Tissue material properties have been found to have a large variation which might be due to the variation in conditions they were tested in, the mammal the tissue belonged to, the testing instrument used or due to intrinsic tissue inhomogeneities. The Young's modulus of healthy breast and brain tissues is found to lie within the range of 3 to 3.5 kPa and that of tumors may range between 5 to 15 times that of the healthy tissue depending on their type (Samani et al., 2007; Murphy et al., 2016). Thus, we selected an initial shear modulus (G_0) value of 1 kPa to model healthy tissue and 5, 10 and 15 kPa values to model cancerous tissue ($G = E/(2(1 + \nu))$). A hyperelastic Arruda-Boyce model (Arruda and Boyce, 1993) was used with maximum limiting stretch (λ_m) as 1.05 and the tissue was assumed to be nearly incompressible ($\nu = 0.4999$). These are generalized values for the sake of simplicity and they have been non-dimensionalized in our further analysis. The Arruda-Boyce model is specified as follows:

$$\Psi = G \left\{ \frac{1}{2}(\bar{I}_1 - 3) + \frac{1}{20\lambda_m^2}(\bar{I}_1^2 - 9) + \frac{11}{1050\lambda_m^4}(\bar{I}_1^3 - 27) + \frac{19}{7000\lambda_m^6}(\bar{I}_1^4 - 81) + \frac{519}{673750\lambda_m^8}(\bar{I}_1^5 - 243) \right\} + \frac{1}{M} \left(\frac{J_{el}^2 - 1}{2} - \ln(J_{el}) \right) \quad (4.1)$$

where Ψ = strain energy per unit reference volume, G , λ_m and M are temperature-dependent material parameters, $\bar{I}_1 = \bar{\lambda}_1^2 + \bar{\lambda}_2^2 + \bar{\lambda}_3^2$ is the 1st deviatoric stretch invariant, J_{el} is elastic volume

ratio between deformed and undeformed volumes of a differential volume element. Deviatoric stretches are defined as $\bar{\lambda}_i = J_{el}^{1/3} \lambda_i$ where λ_i denote principal stretches. The Arruda-Boyce model can also be expressed as:

$$\Psi = G \sum_{i=1}^5 \alpha_i \beta^{i-1} (\bar{I}_1^i - 3^i) + \frac{1}{D} \left(\frac{J_{el}^2 - 1}{2} - \ln(J_{el}) \right) \quad (4.2)$$

where, $\alpha_1 = \frac{1}{2}$, $\alpha_2 = \frac{1}{20}$, $\alpha_3 = \frac{11}{1050}$, $\alpha_4 = \frac{19}{7000}$, $\alpha_5 = \frac{519}{673750}$, and $\beta = \frac{1}{\lambda_m^2}$. For the incompressible Arruda-Boyce model to be consistent with linear elasticity, with G_0 as the initial shear modulus of the material, the following condition has to be satisfied:

$$\left. \frac{\partial \Psi}{\partial I_1} \right|_{I_1=3} = \frac{G_0}{2} \quad (4.3)$$

Substituting Eq. 4.2 in Eq. 4.3, we get:

$$\left. \frac{\partial \Psi}{\partial I_1} \right|_{I_1=3} = G \sum_{i=1}^5 i \alpha_i \beta^{i-1} \bar{I}_1^{i-1} = \frac{G_0}{2} \quad (4.4)$$

Now, inserting the values of α_i and β in Eq. 4.4, we get the initial shear modulus as:

$$G_0 = G \left(1 + \frac{3}{5\lambda_m^2} + \frac{99}{175\lambda_m^4} + \frac{513}{875\lambda_m^6} + \frac{42039}{67375\lambda_m^8} \right) \quad (4.5)$$

$D \approx 0$ refers to the condition of near incompressibility ($\nu \approx 0.5$). A summary of the material parameters employed in the model are specified in Table 4.1.

Table 4.1: **Material parameters used in the model**

Material	Shear Modulus $G(\text{kPa})$	Young's Modulus $E(\text{kPa})$	Maximum limiting stretch (λ_m)	Poisson's Ratio (ν)	References
Tissue	1	3	1.05	0.4999	(Samani et al., 2007; Murphy et al., 2016)
Nodule	5, 10, 15	15, 30, 45	1.05	0.4999	(Skovoroda et al., 1995; Samani et al., 2007)

Gasser Ogden Holzapfel (GOH) anisotropic hyperelastic model

To analyze the effect of anisotropy on nodule detection, the Gasser Ogden Holzapfel (GOH) anisotropic hyperelastic material model (Holzapfel et al., 2000; Gasser et al., 2006) was used to model anisotropic tissue or cellular properties. This model assumes that a material is composed of two families of fibers whose mean directions are separated by an angle 2γ . While the two fiber families have the same mechanical properties, the macroscopic material properties of the substance vary with γ . This has been shown to be the case in arterial walls and cardiac muscles (Gasser et al., 2006). In this model, the strain energy for an incompressible material can be defined as:

$$\Psi = \frac{C}{2} (\hat{I}_1 - 3) + \frac{k_1}{k_2} \left[\exp \left\{ k_2 \left(\kappa \hat{I}_1 + (1 - 3\kappa) \hat{I}_4 - 1 \right)^2 \right\} - 1 \right] \quad (4.6)$$

where, λ is the stretch and C , k_1 and k_2 are material parameters. The 1st part of the equation corresponds to a Neo-Hookean ground matrix or base material and the 2nd part corresponds to the anisotropic fibres. \hat{I}_1 is the 1st invariant and \hat{I}_4 is a pseudo invariant to describe the anisotropic nature of fibres. The uniaxial stress σ_{11} (normal stress in the loading direction) can

then be defined as:

$$\sigma_{11} = \lambda \cdot \frac{d\Psi}{d\lambda} \quad (4.7)$$

4.2.5 Model validation

We validated our model with experimental observations from the study by Zhang et al. (2014). To replicate their study, we used an axisymmetric model of spherical indentation on a homogeneous substrate of shear modulus $G_0 = 0.246$ MPa and maximum locking stretch $\lambda_m = 2.1$. The substrate material was assumed to be Arruda-Boyce hyperelastic and the indenter was assumed to be rigid. The spherical indenter had a radius of 3 mm and the homogeneous tissue was 51 mm in radius and 31 mm thick. As shown in Fig. 4.4, the error between our simulations and the experimental data was within 6% for $\delta/R \leq 0.5$.

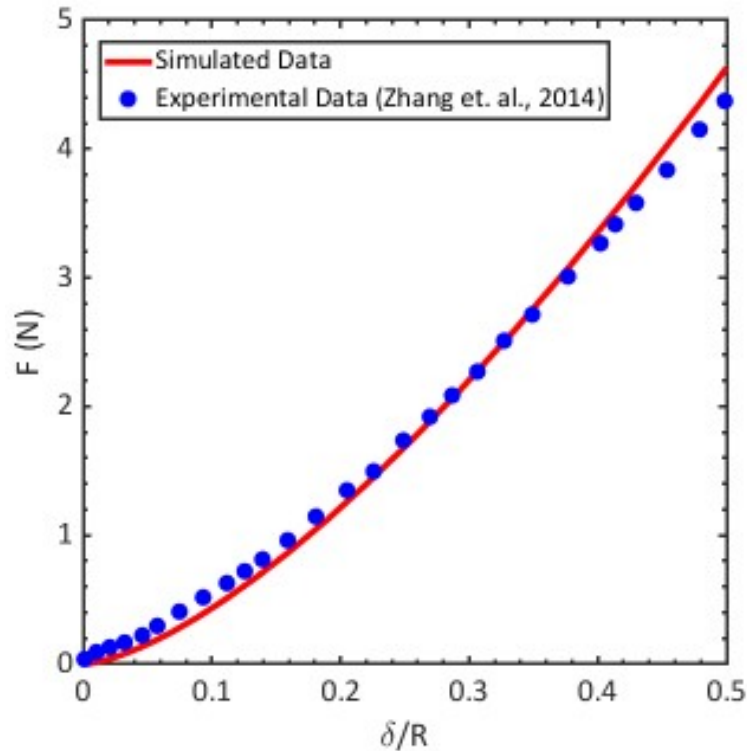


Figure 4.4: **Model validation with experimental data of spherical indentation.** The dependence of indentation load (F) on the ratio of indentation depth (δ) to indenter radius ratio (R) is shown. Data from our simulations are compared with experimental data from Zhang et al. (2014).

4.2.6 Dimensional analysis

Dimensional analysis techniques have been used in several studies on indentation to identify various physical dependencies of the indentation load and hardness of the material (Liu et al., 2010; Low et al., 2015; Yan et al., 2006; Zhang et al., 2014). This technique allows one to develop general relations between physical quantities without the necessity of specifying units of measurement.

The indentation load has been assumed to be the output response in this study. We assume that G_0 represents the apparent stiffness observed by the indenter for the case when nodule is absent (reference case) and G_n represents the stiffness of embedded nodule. We also assume that the indentation load would depend on the material parameters of the hyperelastic model such as the Poisson's ratio ν , stretch ratio λ and model parameters namely, nodule diameter D , nodule depth d , indenter radius R and indentation depth δ/h . The ratio δ/h helps mitigate the effect of finite tissue thickness. The indentation load depends on the independent variables $\lambda_n, \lambda_0, \nu_n, \nu_0, G_n, G_0, D, d, R$ and δ/h where the subscripts "n" and "0" refers to the nodule and tissue (without nodule) parameter, respectively. Therefore, indentation load F can be expressed as:

$$F = f(\lambda_n, \lambda_0, \nu_n, \nu_0, G_n, G_0, D, d, R, \delta/h) \quad (4.8)$$

Since our model considers the tissue and nodule to be incompressible, ν_n and ν_0 can be neglected from further analysis. Moreover, it was demonstrated by Zhang et. al. (Zhang et al., 2014) that indentation load varies with the stretch ratio λ_m of the tissue, but we do not consider variations in λ_n and λ_0 in our study. This reduces the number of variables on which indentation load depends:

$$F = f(G_n, G_0, D, d, R, \delta/h) \quad (4.9)$$

Thus, using the Buckingham Pi theory of dimensional analysis, we consider indenter radius R and shear modulus of tissue without nodule G_0 to be independent parameters. The

indentation load (F) can then be simply written as:

$$\prod_1 = \frac{F}{R^2 G_0} \quad (4.10)$$

where, \prod_1 is a non-dimensional parameter describing the indentation load. This non-dimensional parameter can be considered physically similar to the strain imposed by an indenter of radius R on a healthy tissue of shear modulus G_0 . Further relating this imposed strain to the dimensionless parameters nodule diameter and depth, shear modulus of nodule and indentation depth, we get:

$$\frac{F}{R^2 G_0} = \prod_2 \left(\frac{G_n}{G_0}, \frac{D}{R}, \frac{d}{R}, \frac{\delta}{h} \right) \quad (4.11)$$

Simulations relating both sides of Eq. 4.11 have been carried out in the subsequent sections to explore the predictability of the presence of an embedded cancer nodule in a healthy tissue.

4.3 Results and discussion

The results in this section allow us to derive relations between the indentation load and the factors affecting it in an attempt to increase the efficiency and predictivity of nodule detection and localization. The substrate tissue stiffness assumed in our model is similar to soft human tissues like the brain (Murphy et al., 2016), liver, breast, tongue, tonsils and spleen. Cancerous nodules have been shown to have an increased stiffness of nearly 5 to 15 times that of the corresponding healthy tissue (Skovoroda et al., 1995; Samani et al., 2007). Using simulations, we analyze the limitations of the Hertz contact theory predictions and its efficacy in determination of composite tissue stiffness (tissue with an embedded nodule). Although some earlier studies (Konstantinova et al., 2013, 2017) have analyzed the effect of embedded nodule diameter and depth on indentation load, they have used Hertz contact model to relate the load to nodule physical properties. We also analyze the effect of nodule parameters such as stiffness, diameter and depth on indentation loads and this allows us to create a palpation sensitivity chart to define regions of nodule detectability. Additionally, we study how indentation or palpation loads are

affected if an anisotropic nodule is embedded in an isotropic tissue and vice-versa.

4.3.1 Detection of composite stiffness of tissue and nodule using Hertzian and finite element approach

Detection of composite tissue (tumor nodule embedded inside healthy tissue) stiffness is the first essential step to detect a nodule and determination of its characteristics. Composite tissue relatively stiffer than its local environment might indicate presence of embedded nodule and it can then be further probed locally to detect properties of the nodule. The classical Hertz formulation can be used to determine force (F_{Hertz}) and deformation relationship in elastic contact between two bodies. One of which has very high stiffness and, hence, can be assumed to be rigid. The other body which is deformable, is generally described as:

$$F_{Hertz} = \frac{4G_0R^{1/2}\delta^{3/2}}{1-\nu^2} = \frac{16G_0\delta\sqrt{R\delta}}{3} \quad (4.12)$$

where G_0 is the shear modulus of deformable body, R and δ are the indenter radius and indentation depth respectively and $\nu \approx 0.5$, assuming incompressibility. Tissues are generally heterogeneous and have a finite thickness. Hayes et al. (1972) suggested a mathematical formulation that takes into account the effect of tissue thickness in linear elastic materials:

$$F_{Hayes} = \frac{4aG_0\delta}{1-\nu} \times \omega\left(\frac{R}{h}, \frac{\delta}{h}\right) \quad (4.13)$$

where a = radius of contact circle, G_0 = shear modulus of substrate, δ = indentation depth, R = indenter radius, h = tissue thickness, ω = factor used to introduce the effect of substrate thickness. On comparing the FE solution with the analytical solution for indentation on a substrate of finite thickness by (Hayes et al., 1972) we found that for $\delta/h < 5\%$, the FE solution matches the Hertz solution more closely ($\leq 1.55\%$ difference) rather than Hayes' solution ($\leq 4.64\%$ difference) (Tables 4.2, 4.3).

A linear elastic model of contact between a hemispherical indenter and a tissue was therefore first validated by comparing it to the Hertzian model of contact for small strains. Fig. 4.5

Table 4.2: **Difference between FE solution and Hertz solution for homogeneous tissue of $G_0 = 1$ kPa for varied tissue thickness**

Tissue thickness, h (mm)	Maximum difference ($F_{FE} - F_{Hertz}$) ($\times 10^{-4}$) (N)	$\left(\frac{F_{FE} - F_{Hertz}}{F_{Hertz}}\right) \times 100\%$
10	4.054	1.55%
20	1.337	0.51%
30	0.496	0.19%
40	0.005	0.0019%
50	-0.025	-0.0096%

Table 4.3: **Difference between FE solution and Hayes' solution for homogeneous tissue of $G_0 = 1$ kPa for varied tissue thickness**

Tissue thickness, h (mm)	Maximum difference ($F_{FE} - F_{Hayes}$) ($\times 10^{-4}$) (N)	$\left(\frac{F_{FE} - F_{Hayes}}{F_{Hayes}}\right) \times 100\%$
10	-1.20	-3.27%
20	0.74	2.18%
30	1.22	3.69%
40	1.45	4.44%
50	1.50	4.64%

suggests that the Hertz solution is sufficiently accurate to quantify the stiffness of homogeneous tissue of finite thickness when $\delta/h \leq 5\%$. It was also found that in case of finitely thick tissues,

the Hertz solution is not suitable for large indentation depths ($\delta/h \geq 10\%$). The Hertz solution underestimates the tissue stiffness at large indentation depths as seen in Fig. 4.5 where greater force amplitude of the solid curve (red) implies higher effective tissue stiffness. Even the dashed (black) and dotted (magenta) curves diverge slightly from the predicted Hertz solution at a δ/h ratio of 10% and 4% respectively. Using the Hertz formulation in Eq. 4.12, one cannot detect heterogeneities in the substrate except by comparing the coupled material properties of the substrate with a reference. A spherical indenter can be employed to determine the coupled stiffness in the presence of an embedded nodule using the Hertz contact solution. This equation can be modified to attain the form:

$$\frac{dF}{d\delta} = 8G\sqrt{R\delta} \quad (4.14)$$

where $dF/d\delta$ represents instantaneous stiffness evolving with the indentation depth as the load is increased on the indenter tip. An instantaneous stiffness as a function of non-dimensional deformation for nodules located at different depths (embedded near the tissue surface (i.e. $d = 0.5$ mm and $d = 3.5$ mm) relative to a homogeneous tissue (without nodule) (Fig. 4.6a). Initially, the instantaneous stiffness increases with indentation depth before saturating at greater indentation depths. However, a near-linear relationship is found to exist between $dF/d\delta$ and $\sqrt{R\delta}$ whose slopes ($= 8G$) determine the shear moduli G of the composite incompressible tissues (Fig. 4.6b). This indicates that the Hertz formulation can be employed to detect the coupled stiffness of substrates but it cannot differentiate between presence and absence of a nodule, especially if the nodule is located deep inside the tissue ($d = 3.5$ mm). The effect of tissue thickness on our results was mitigated by using the non-dimensional indentation depth δ/h relative to the tissue thickness.

4.3.2 Effect of non-dimensional parameters on indentation load

The radius of the indenter (R) is expected to be an important factor in nodule detection as this radius along with the indentation depth determines the contact surface area between the indenter and tissue surface. Contact force should vary with a variation in the contact area for a constant indentation depth. The optimal design and size of the indenter can allow a robotic in-

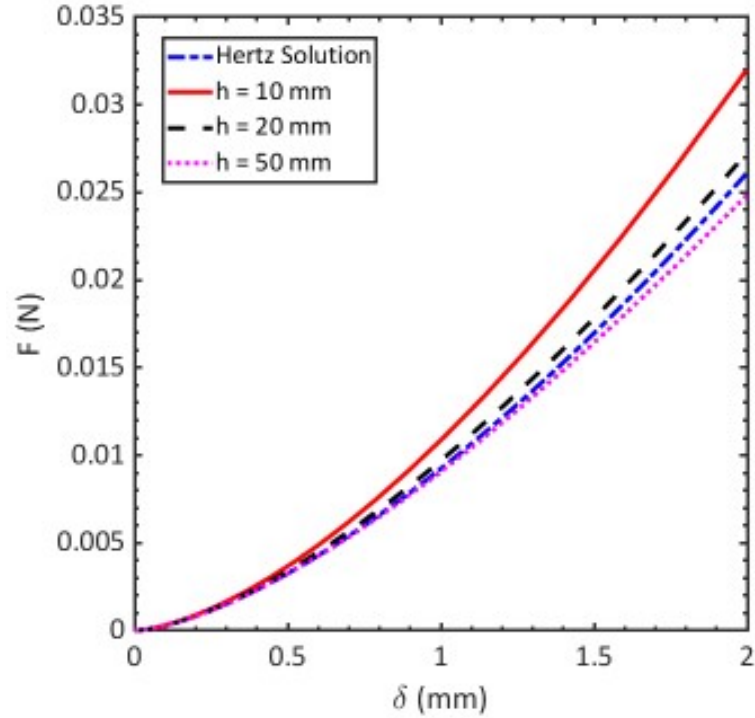


Figure 4.5: **Comparison of the computationally generated indentation load F_0 with analytical Hertzian solution F_H up to a maximum indentation depth $\delta = 2$ mm.** Homogeneous tissues (without nodule) of various thicknesses (h) are considered.

strumented probe to be much more sensitive towards sensing embedded nodules in tissues. This can make the robotic palpation process more efficient. Therefore, using dimensional analysis, we investigated its influence on peak indentation load for indenters of two radii: 3 mm and 5 mm. Dimensional analysis techniques allow us to develop general physical relations between quantities of interest in a system.

Effect of nodule depth, d on indentation load

The effect of nodule depth (d) on dimensionless indentation load was investigated for an indentation depth (δ) of 0.5 mm that corresponds to a normalized depth (δ/h) of 0.05. Our results show that for a representative nodule of diameter $D = 5$ mm and $G_n/G_0 = 15$, a thin indentation/palpation probe ($R = 3$ mm) is more sensitive to variation in nodule depth relative to indenter radius (d/R) (Fig. 4.7a). That is, the detection resolution of a thin indenter is higher than a thick one for a constant nodule diameter (D/R). Even for a relatively deeply embedded nodule, that is, as d/R increases, a thick probe is less likely to detect it based on relative

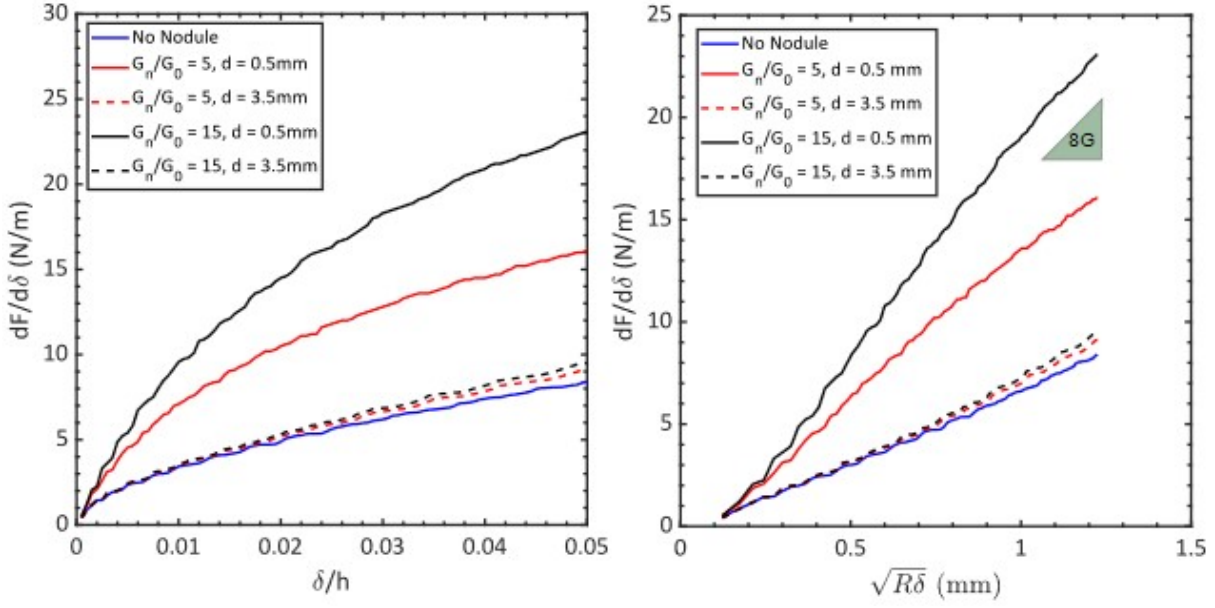


Figure 4.6: **Instantaneous tissue stiffness measured as a function of indentation load and depth.** (A) Relation of instantaneous tissue stiffness ($dF/d\delta$) with the indentation depth normalized by tissue thickness (δ/h). (B) Relation between $dF/d\delta$ and $\sqrt{R\delta}$, parameters of the Hertz model to determine composite tissue stiffness. Both plots are for $h = 10$ mm, $R = 3$ mm and $D = 5$ mm.

comparison with the surrounding areas. Therefore, palpation probes with small radii are better suited to detection of an embedded nodule. Curve-fitting of the data as in Fig. 4.7a reveals predictive relationships between dimensionless indentation load and the nodule depth normalized by indenter radius. As shown in Fig. 4.7A, for $R = 3$ mm, the dimensionless force varies as:

$$F/(R^2G_0) = -7.14(d/R)^{0.23} + 7.96 \quad (4.15)$$

and for $R = 5$ mm, it varies as:

$$F/(R^2G_0) = -2.26(d/R)^{0.36} + 2.40 \quad (4.16)$$

These relations show that although a larger probe is capable of sensing greater indentation loads as evidenced by the power of d/R , the curvature resulting from a smaller probe leads to greater sensing resolution, as given by the coefficient of d/R .

Fig. 4.7b shows the influence of indentation depth on load for an embedded nodule. It was

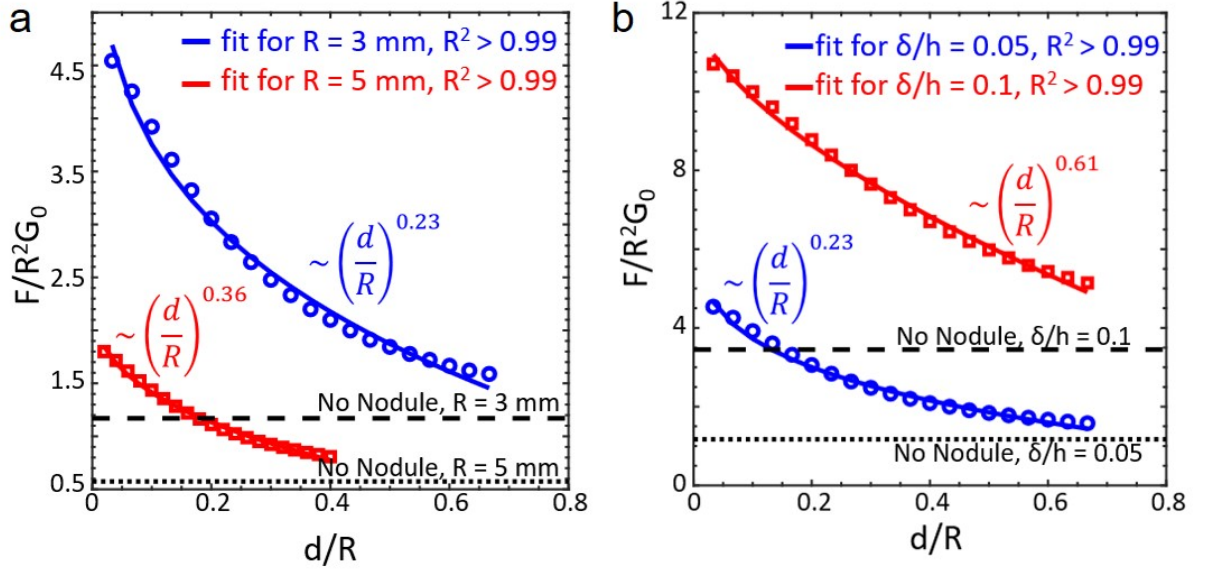


Figure 4.7: **Dependence of nodule detectability on nodule depth.** (a) Variation of F/R^2G_0 with d/R for $R = 3$ mm (dashed line) and 5 mm (dotted line). (b) Variation of F/R^2G_0 with d/R for $\delta/h = 0.05$ (dotted line) and 0.1 (dashed line). Both (a) and (b) refer to cases where $G_n/G_0 = 15$ and $D = 5$ mm. The power-law dependence is denoted beside the fitted curve.

found that loads decrease more rapidly (greater initial slope) in case of $\delta/h = 0.1$ for a range of nodule depths. There ceases to be an appreciable difference in indentation loads with increase in d/R beyond a certain value which increases with δ/h . For $\delta/h = 0.05$, the dimensionless force varies as:

$$F/(R^2G_0) = -7.09(d/R)^{0.23} + 7.90 \quad (4.17)$$

and for larger indentation depth $\delta/h = 0.1$, it varies as:

$$F/(R^2G_0) = -9.21(d/R)^{0.61} + 12.10 \quad (4.18)$$

These results show that as indentation depth increases, the effect of nodule depth on indentation load increases. Therefore, the deeper a probe palpates, the greater the chance is of detecting an embedded nodule, a prediction that is physically reasonable.

Effect of nodule diameter, D on indentation load

Cancer nodules have been found to have a positive correlation between diameter and malignancy over time. Small early-stage cancerous nodules if detected, can be removed to avoid later complications. Although nodule size, malignancy and stiffness are independent quantities in cancer, they are usually correlated, i.e. a large nodule is more likely to be stiffer and malignant than a small one as tumor sizes increase with maturity (Evans et al., 2012).

Dimensionless indentation load increases nonlinearly with nodule diameter as shown in Fig. 4.8a. For $R = 3$ mm, dimensionless load can be curve-fit as:

$$F/(R^2G_0) = 0.87(D/R)^{1.5} + 1 \quad (4.19)$$

and for $R = 5$ mm as:

$$F/(R^2G_0) = 0.73(D/R)^{1.8} + 0.51 \quad (4.20)$$

Both curves fit the simulated data very well with $R^2 > 0.99$. Unlike the case of load dependence on nodule depth d/R in Fig. 4.7a, the coefficients of D/R for $\delta/h = 0.05$ and 0.1 are not too far apart. Therefore, the sensing resolution of nodule diameter change is relatively similar in both cases.

Increasing indentation depth relative to the tissue thickness increases the detectability of larger nodules as shown in Fig. 4.8b. The dimensionless force is found to vary with D/R for $\delta/h = 0.05$ as:

$$F/(R^2G_0) = 0.87(D/R)^{1.53} + 1.07 \quad (4.21)$$

and for $\delta/h = 0.1$ as:

$$F/(R^2G_0) = 2.05(D/R)^{2.05} + 3.32 \quad (4.22)$$

For large indentation depths ($\delta/h \geq 0.1$), a steep increase in indentation load beyond a threshold

nodule diameter ($D/R > 1$) is found to occur. This is reflected in the greater power of D/R for $\delta/h = 0.1$. Greater indentation depth can predict the diameter of a nodule with higher sensitivity based on higher indentation load.

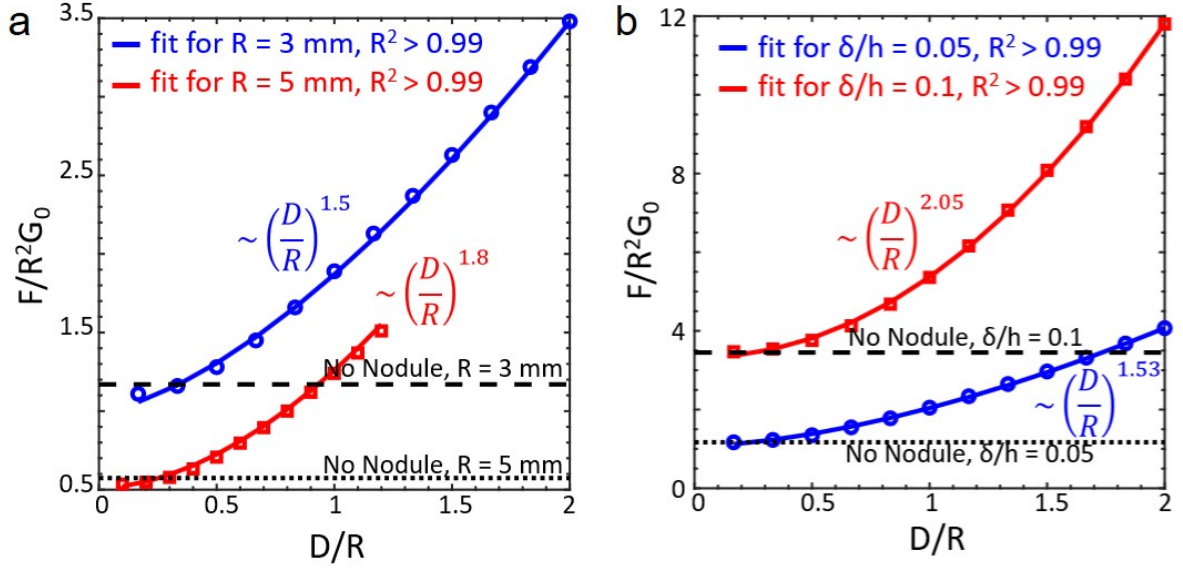


Figure 4.8: **Dependence of nodule detectability on nodule diameter.** (a) Variation of F/R^2G_0 with D/R for $R = 3$ mm (dashed line) and 5 mm (dotted line), and (b) Variation of F/R^2G_0 with D/R for $\delta/h = 0.05$ (dotted line) and 0.1 (dashed line). G_n/G_0 and d in all cases were fixed at 15 and 0.5 mm respectively. The power-law dependence is denoted beside the fitted curve.

4.3.3 Effect of anisotropy on nodule detection

Many tissues are most accurately described as anisotropic with material properties differing with fiber orientation, for instance, arteries, cardiac tissue and muscular tissues (Holzapfel et al., 2000; Gasser et al., 2006). Directional distribution of internal fibers in a tissue alters its mechanical properties. A fibrous material has greater mechanical strength in the direction of fiber orientation than transverse to it. To investigate the effect of anisotropic material properties on detection of an embedded nodule, we employed the GOH material model as described above. The strain energy of a GOH material model is as defined in Eq. 4.6 in Section 4.2.4. Here, $\hat{I}_4 = \lambda_x^2 \cos^2 \gamma + \lambda_y^2 \sin^2 \gamma$, with λ_x and λ_y being stretches in the x and y directions. For a cylindrical coordinate system, x and y are replaced by r and z respectively. Two fibre families (both

assumed to have the same mechanical properties) with directions a_{01} and a_{02} are separated by an angle 2γ , as shown in Fig. 4.9a.

By fitting Eq. 4.7 to experimental data, we can identify the variables C , k_1 and k_2 . Due to the difficulty of acquiring relevant data to quantify the anisotropy in tissues, for our study we use the pig aorta experimental data provided by Peña et al. (2010). They found C , k_1 and k_2 to be 24.6 kPa, 4.9 kPa and 2.93, respectively. They also found the inter-fiber angle to be nearly 46° . Using these material parameters interchangeably to define the tissue and the nodule, we assessed the influence of fiber dispersion index (κ) on nodule detection. κ varies from 0 to $1/3$, where $\kappa = 0$ when fibers are highly directional parallel to the indentation axis and $\kappa = 1/3$ when all fibers are dispersed homogeneously and its effect on strain energy can be quantified from Eq. 4.6.

Our results show that although an anisotropic nodule embedded in an isotropic tissue versus an isotropic nodule embedded in an anisotropic tissue can be differentiated between using indentation, fiber orientation itself had no significant influence on nodule detection (Fig. 4.9A). In fact, fibrous tissue occluded an embedded nodule from getting detected by a palpation probe leading to non-significant changes in indentation load.

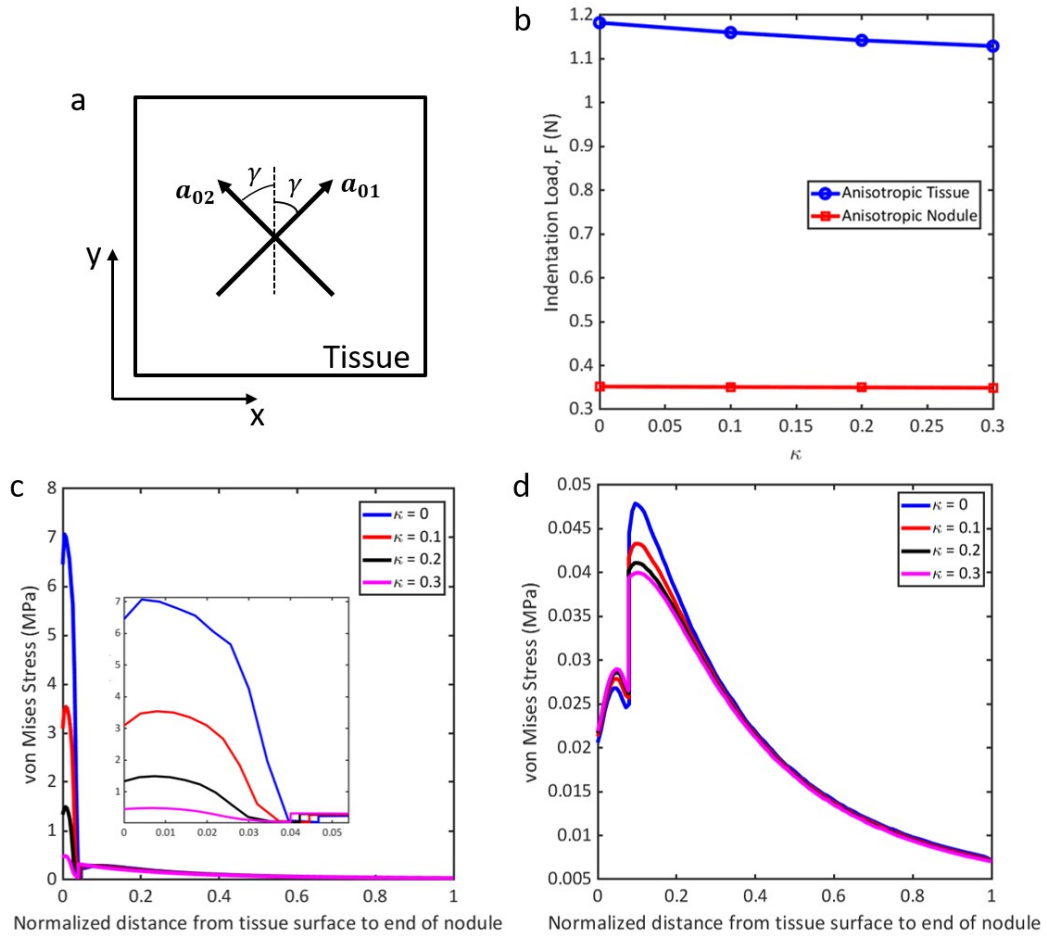


Figure 4.9: **Effect of anisotropy on nodule detection.** (A) A schematic of GOH material model. a_{01} and a_{02} denote two fiber families of same mechanical properties but separated by an angle 2γ embedded in a fibrous tissue. (B) Dependence of indentation load F on fiber orientation κ for isotropic nodule embedded in anisotropic tissue (blue circles) and for anisotropic nodule embedded in isotropic tissue (red squares). Both curves correspond to $d/R = 0.17$, $D/R = 1.67$ and $\delta/h = 0.1$. (C) Stress profiles in anisotropic tissue embedded with isotropic nodule under indenter from tissue surface to end of nodule. The change in von Mises stress profiles is shown for various degrees of fiber dispersion. (Inset) Stress profiles just under the indenter are magnified for clarity. All curves correspond to $d/R = 0.17$, $D/R = 1.67$ and $\delta/h = 0.1$. (D) Stress profiles in isotropic tissue embedded with anisotropic nodule under indenter from tissue surface to end of nodule. All curves correspond to $d/R = 0.17$, $D/R = 1.67$ and $\delta/h = 0.1$. (C, D) The change in von Mises stress profiles is shown for various degrees of fiber dispersion. (B-D) For anisotropic nodule embedded in isotropic tissue, initial $G_n = 24.6$ kPa, initial $G_0 = 10$ kPa, while for isotropic nodule in anisotropic tissue, initial $G_n = 250$ kPa, initial $G_0 = 24.6$ kPa.

Interestingly, stresses in the composite tissue under the indenter increased by an order $O(2)$ in case of anisotropic tissues with isotropic embedded nodule (Fig. 4.9C) over isotropic tissues with anisotropic embedded nodule (Fig. 4.9D). The largest peak stress was found when the fibers in the tissue were highly directional parallel to the indentation axis ($\kappa = 0$). A significant difference of $\approx 1300\%$ between the peak stresses in $\kappa = 0$ and $\kappa = 0.3$ was observed in Fig. 4.9B while there was a difference of only 18.75% between the same conditions in Fig. 4.9D with change in fiber dispersion index. It is also interesting to note that the stresses at the tissue-nodule interface in Figs. 4.9C and 4.9D do not show appreciable change but the stresses drastically decrease in the tissue under the indenter above the tissue-nodule interface in Fig. 4.9C. We find these trends to be similar even if we increase the indentation depth δ/h to 20%. Therefore, our results suggest that embedded isotropic nodules in fibrous tissue or fibrous nodules in smooth tissue cannot be detected simply by palpating the tissue and measuring the indentation load, but would additionally require an estimation of internal stress field generated in the system. Tumors have been shown to generally lack a definite fiber direction and thus can be considered isotropic. Tissues that are usually palpated to detect nodules are breast (non-invasive palpation), liver, pancreas, intestine and other abdominal organs (invasive/laparoscopic palpation). Many of these tissues including breast, liver, pancreas and intestine are either glandular or made of smooth muscles, the quantitative palpation technique described in our study can be readily applied to detect embedded isotropic tumors. However, for fibrous tissues such as heart, arteries and muscles, additional techniques are required to predict presence and properties of isotropic tumor nodules. Therefore, instrumented indentation to detect cancer/tumor nodules embedded in fibrous tissues might not be a favorable technique to predict the location, size and material properties of cancer tissues.

4.4 Palpation sensitivity chart

Based on our aforementioned non-dimensional analyses, we determine regimes where an isotropic nodule embedded in an isotropic tissue can be detected by a palpation probe with reasonable accuracy. Studies suggest that a change of at least 7% in loads felt by a human finger is required to discriminate a hard surface from a soft one (Pang et al., 1991). To allow for instrument and sensor errors, in our study, we use a very conservative threshold of 20% between indentation

loads with and without a nodule to determine the presence of an embedded nodule. This quantity is defined as $\Delta F/F_0 = (F - F_0)/F_0$ and is termed as palpation sensitivity in this study, where F is the indentation load in presence of nodule and F_0 is the load in absence of nodule. The palpation sensitivity charts in Fig. 4.10 allow us to predict regimes where an embedded nodule would be detectable by a palpation probe of a given radius. These charts summarize and quantify our predictions that the detectability of an embedded nodule parameterized by the change in indentation load in presence and in absence of nodule increase with increasing diameter and decreasing depth of nodule. Large nodules deeply embedded in tissues can also be detected by this process. These charts also demonstrate that with increasing nodule stiffness, there is a leftward shift of the threshold (20%) line indicating greater sensitivity of palpation process with increasing stiffness. However, this process suggests that palpation would not be able to detect stiff and very small nodules even if they are located close to the tissue surface.

It is interesting to note that the palpation sensitivity of embedded nodules decreases in case of greater indentation depth $\delta/h = 0.2$ than $\delta/h = 0.1$. This might be because as indentation depth increases in a tissue of finite thickness, the effect of the rigid underlying substrate leads to a nonlinear increase in indentation loads both in presence and in absence of nodule. The effect of the underlying rigid substrate in case of tissues in the abdomen such as a thin section of liver over a hard bone must be considered during palpation. This palpation sensitivity map might serve as a guideline for precise instrumented palpation or robotic surgery before surgical removal of tumor from healthy tissue. Due to the generality of our model and results, various material and physical properties of an embedded nodule relative to the surrounding healthy tissue might be gained by analyzing the output indentation loads.

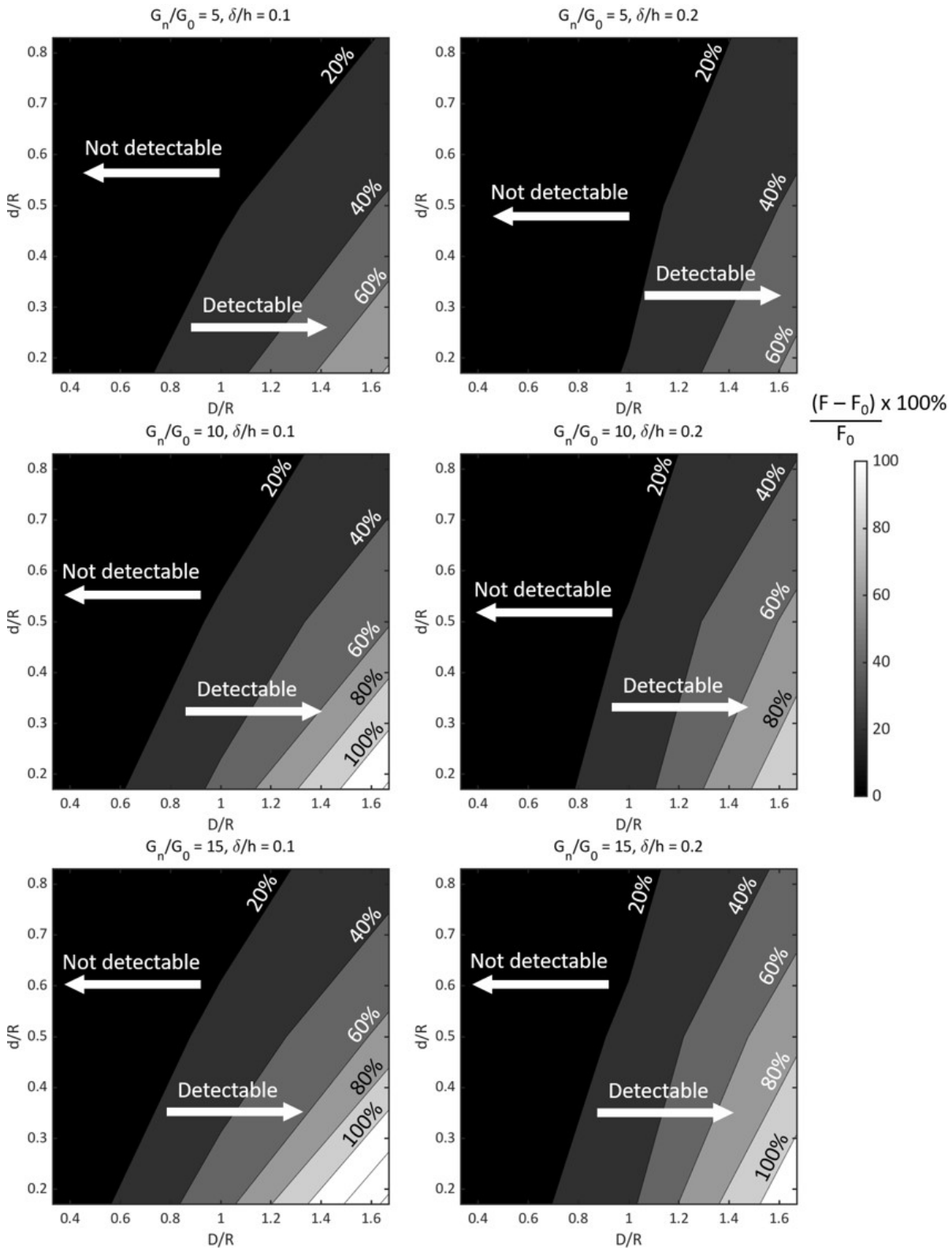


Figure 4.10: Palpation sensitivity chart for $\% \Delta F / F_0$ versus nodule diameter and depth relative to indenter radius for $G_n / G_0 = 5, 10$ and 15 for large indentation depths $\delta / h = 0.1$ and 0.2 . Grayscale represents the value of $\% \Delta F / F_0$. The detectable and undetectable regimes and $\% \Delta F / F_0$ of contour lines $> 20\%$ (detection threshold) are indicated for all cases.

4.5 Conclusion

This study proposes a general methodology to detect the presence and location of an embedded spherical inhomogeneity in a soft material and the extraction of its material properties. Using a hyperelastic material model our study examines the effect of nodule diameter and nodule depth on detection and localization of an embedded nodule inside a tissue. Our study also analyzes the influence of anisotropic material properties of the tissue and nodule itself on nodule detection. Our dimensional analysis results can be employed to analyze any indentation study on any homogeneous hyperelastic material with an embedded inhomogeneity, as this model is independent of indenter size and individual mechanical properties of substrate and nodule. The contributions of this study are summarized in Fig. 4.11. Following key conclusions can be drawn from this study:

- The Hertzian model cannot sufficiently predict the presence of an embedded nodule in a soft tissue beyond an indentation depth of $> 5\%$. Moreover, it cannot predict the material or physical properties of an embedded nodule. Hence, there is a need for a better predictive model for inhomogeneous hyperelastic materials.
- Contact force between the indenter and the tissue with an embedded nodule depends on the aspect ratio of nodule relative to the indenter. A thin indenter can predict the nodule depth with greater accuracy and sensitivity than a thick indenter.
- Indentation load alone is insufficient to predict the presence of an embedded isotropic nodule in an anisotropic tissue due to change in fibre dispersion or vice versa. However, it can clearly differentiate between an isotropic nodule embedded in an anisotropic tissue versus an anisotropic nodule embedded in an isotropic tissue.
- Stresses in the composite tissue under the indenter increased by an order $O(2)$ in case of anisotropic tissues with embedded isotropic nodule over isotropic tissues with embedded anisotropic nodule.
- A predictive palpation sensitivity map has been developed in this study to define regions of detectability of nodule using a threshold of 20% increase of indentation load in presence of nodule to that in case of a homogeneous tissue.

It must be noted that in the section where we assess the detectability of an isotropic nodule in anisotropic tissue and vice-versa, we assume the tissue and nodule to have properties similar to arteries from the literature, mainly due to unavailability of experimental results. However, the conclusions from the study are general and can be extended to other kinds of tissues that have been shown to have layered morphology with two families of fibers. Tissues of this kind include the stomach wall, tendons and ligaments. The purpose of this study is to assess tumor nodule detectability via laparoscopic/minimally invasive surgical procedures.

In our study, to take into account noisy acquisition of force signals during instrumented palpation, we set a very conservative threshold of $\% \Delta F / F_0 = 20\%$ below which we assume that an embedded nodule cannot be detected. It is likely that using high-precision force sensors for signal acquisition would have a better nodule detection resolution. The palpation sensitivity maps proposed in this thesis can be used in conjunction with imaging techniques to detect tumor nodules. Using modern imaging techniques like MRI, an estimated region where the nodule is located can be detected via 2D images of the tissue. The instrumented palpation probe can then be used to determine the exact location of the nodule in the real tissue. It can also be used to determine the approximate nodule stiffness relative to tissue stiffness to estimate the tumor condition or stage.

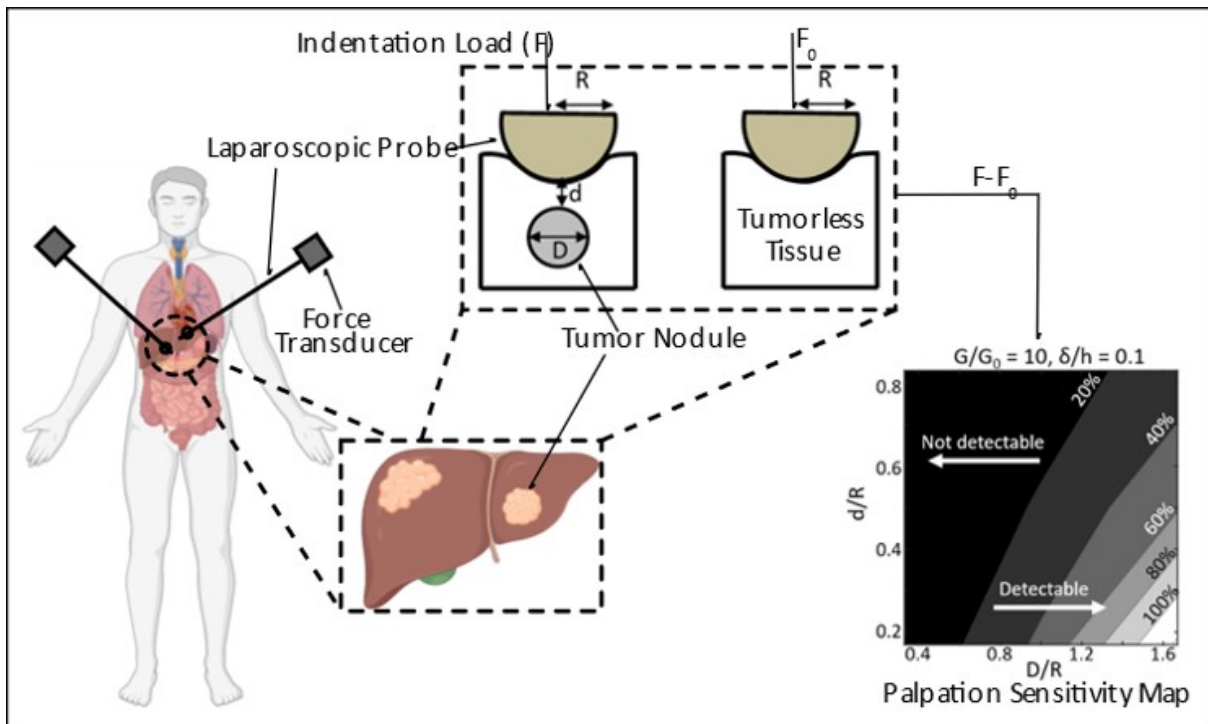


Figure 4.11: Summary of the contributions of this study on embedded nodule detection.

Chapter 5

Summary and Conclusions

Cancer development and spreading mechanisms have been studied a lot from a molecular and systems point of view. However, a mechanical understanding of cancer metastasis and tumor detection has not been sufficiently emphasised in the literature. In this thesis, the modelling of cancer mechanics at the cellular and tissue levels is described in three parts. In the first part of this thesis, the development of a cell migration model is described. This model considers a cell devoid of glycocalyx migrating through an extracellular matrix (ECM). Cell migration is crucial in processes of tissue development, cancer metastasis and wound healing, to name a few. Very often the migrating environment involves interfacial migration, that is, cell migration at the interface of two dissimilar types of tissues. In such a scenario, how the relative mechanical properties of cell nucleus and tissue enable or impede migration was studied as part of this thesis. The system was modelled to be viscoelastic. Additionally, we considered cytoskeletal stiffening under strain and plastic deformation of the nucleus. Our results show that cells migrate through confined environments mainly by two strategies: nuclear softening or plastic deformation of stiff nuclei. Neutrophils instrumental in wound healing and highly metastatic cancer cells have been shown to have soft nuclei whereas, osteosarcoma cells (bone cancer) and HGPS (progeria) cells have been shown to have stiff nuclei. Soft nuclei deform easily and facilitate confined migration. Stiff and plastic nuclei in our model were predicted to undergo compression-induced extreme nuclear membrane bending that could be related to nuclear membrane blebbing and rupture incidences observed in experiments. This leads us to speculate on the possibility that plastic deformation and nuclear rupture in such scenarios might be a DNA damage limiting and survival mechanism of cells while ensuring successful migration through confinement. To validate our model predictions, we also performed experiments on stiff and soft nuclei showing that stiff nuclei indeed undergo plastic deformation under confinement and result in greater DNA damage.

In the second part of this thesis, we built up on our cell migration model to incorporate

a glycocalyx that is assumed to be attached to the cell membrane as a continuum and modelled as a Neo-Hookean hyperelastic material. Glycocalyx is made of sugar molecules and polypeptide polymers with sidechains. These polymer chains collectively act as a polymer brush in the event of external forces or stresses. Moreover, the glycocalyx has been shown to regulate cell membrane shapes depending on polymer chain length and polymer density and segregate integrin-based adhesions. Additionally, the glycopolymer thickness and density have been shown to strongly correlate with the metastatic potential of a cancer cell. These experimental observations point to the glycocalyx mechanically facilitating confined cell migration. Indeed, our results recorded in this thesis demonstrate that upon indentation, a thick glycocalyx acts as a shock absorber or cushion under large strains primarily by increasing the surface area of external force application. Further analysis of cell compression in a sandwiched configuration between a rigid plate (on which the cell is assumed to be attached) and the ECM revealed that cell spreading is a critical factor that determines intracellular stresses, ECM displacement due to glycocalyx and contact forces between glycocalyx and ECM. These additional factors were found to have an impact on the mechanics of cellular glycocalyx apart from its thickness and density.

Combining the first and second part of the thesis by moving on to the tissue level of tumor formation and detection, we created a model to detect an embedded tumor in healthy tissue. This model was created to mimic indentation or probing a tissue using a laparoscopic probe. In laparoscopic surgeries, the surgeon cannot palpate a tissue to "feel" the location, stiffness and size of an embedded tumor as in a conventional surgery. The surgeon must use a thin laparoscopic probe for the procedure. This leads to a possible loss of sensation for the surgeon. We used dimensional analysis techniques and developed predictive power laws to relate indentation loads to size and location of embedded nodules in tissue. Additionally, we developed palpation sensitivity maps to predict the regions of detectability of an embedded tumor nodule based on its stiffness relative to the surrounding tissue, size and location. In contrast to a human perception threshold of around 7% difference in perceived loads required to detect difference in stiffness of two objects, we used a very conservative threshold of 20% to account for possible measurement/instrument errors. These maps and relations can be used by clinicians to predict presence or absence of an embedded tumor nodule. It must be noted that tumors form progressively over time. It is the result of cell migration and a plethora of molecular and chemical changes in cells that clump together and accelerate the growth of a

tumor. The cellular glycocalyx and ECM play a significant role in tumor formation as they are instrumental in facilitating cell migration and also impart stiffness to the tumor. A cancer cell is often softer than a healthy cell, however, a cancerous tumor is stiffer than healthy tissue.

5.1 Contributions

This research aims at understanding and modelling the mechanics of cancer cells and tumors. The main contributions of this research work are as follows:

- A new continuum model for confined interfacial cell migration was developed. Predictions of this model can be used to complement experimental observations.
- The importance of nuclear softening on the one hand and plastic strain hardening on the other were studied to define regimes where either of these could be used as strategies by cells to migrate.
- A possible reason for nuclear rupture in-vivo was proposed based on computer simulations.
- A novel continuum model of glycocalyx brush was developed.
- The mechanical influence of cellular glycocalyx in presence of extracellular stresses was studied.
- A tissue-scale model was developed to detect embedded spherical tumor nodules in healthy tissue.
- Dimensional analysis was used to predict indentation loads as simple power law functions of nodule size and location.
- Palpation sensitivity maps were created to define regions of detectability of embedded nodule based on its stiffness, size and location. These maps and relations can guide clinicians to perform more precise surgeries and to train haptic simulators.

5.2 Scope for future research

Modelling of cell and tissue mechanics pertaining to cancer has huge potential as advanced experimental techniques uncover more of the mysteries that lie at these levels. Moreover, interdisciplinary research at the interface of engineering, physics and biology can give a holistic understanding into these biological systems. Therefore, in our view, this study can be extended by increasing the complexity of cell migration model to analyze the influence of fibrous ECM on cell mechanics during migration. The effect of various organelles and the dynamics of the actin cytoskeleton during migration are other avenues that can be explored. Additionally, the effect of various nodule shapes embedded in healthy tissue on their detectability can be studied.

List of Publications

Journal Publications: Included in Thesis

1. **Mukherjee A**, Barai A, Singh R K, Yan W, Sen S, 2020, “Nuclear Plasticity Increases Susceptibility to Damage During Confined Migration”, *PLoS Computational Biology*, 16(10):e1008300. doi: 10.1371/journal.pcbi.1008300
2. **Mukherjee A**, Gupta A, Sen S, Yan W, Saigal A, Singh R.K, “Palpation sensitivity of an embedded nodule using the finite element method”, *ASME Journal of Engineering and Science in Medical Diagnostics and Therapy*, (Accepted)

Manuscript under Preparation

1. “Modelling the mechanical impact of glycocalyx on confined cell migration”

Journal Publications: Not included in Thesis

1. Barai A, **Mukherjee A**, Das A, Sen S, 2020, “ α -actinin-4 is a regulator of myosin IIB expression and myosin IIA localization”, (Under Preparation)

International Conferences

1. **Mukherjee A**, Barai A, Singh R K, Yan W, Sen S, 2020, “Evolution of Cell/Substrate Stresses During Confined Interfacial Migration ”, *64th Biophysical Society Annual Meeting 2020, San Diego, USA*

2. **Mukherjee A**, Singh R K, Yan W, Sen S, 2019, “Evolution of Stresses at Cell-Gel Interfaces During Confined Interfacial Migration”, *63rd Biophysical Society Annual Meeting 2019, Baltimore, USA*

References

- Alberts, B., Johnson, A., Lewis, J., Raff, M., Roberts, K., Walter, P., 2007. *Molecular Biology of the Cell*. New York: Garland Science .
- Alexander, S., Weigelin, B., Winkler, F., Friedl, P., 2013. Preclinical intravital microscopy of the tumour-stroma interface: invasion, metastasis, and therapy response. *Curr. Opin. Cell Biol.* 25, 659–671.
- Arruda, E.M., Boyce, M.C., 1993. A three-dimensional constitutive model for the large stretch behavior of rubber elastic materials. *J. Mech. Phys. Solids* 41, 389–412.
- Aung, A., Seo, Y.N., Lu, S., Wang, Y., Jamora, C., del Álamo, J.C., Varghese, S., 2014. 3D traction stresses activate protease-dependent invasion of cancer cells. *Biophys. J.* 107, 2528–2537.
- Bergert, M., Erzberger, A., Desai, R.A., Aspalter, I.M., Oates, A.C., Charras, G., Salbreux, G., Paluch, E.K., 2015. Force transmission during adhesion-independent migration. *Nat. Cell Biol.* 17, 524–529.
- Booth-Gauthier, E.A., Du, V., Ghibaudo, M., Rape, A.D., Dahl, K.N., Ladoux, B., 2013. Hutchinson–gilford progeria syndrome alters nuclear shape and reduces cell motility in three dimensional model substrates. *Integr. Biol.* 5, 569–577.
- Buxboim, A., Swift, J., Irianto, J., Spinler, K.R., Dingal, P.D.P., Athirasala, A., Kao, Y.R.C., Cho, S., Harada, T., Shin, J.W., et al., 2014. Matrix elasticity regulates lamin-a, c phosphorylation and turnover with feedback to actomyosin. *Curr. Biol.* 24, 1909–1917.
- Cao, X., Moeendarbary, E., Isermann, P., Davidson, P.M., Wang, X., Chen, M.B., Burkart, A.K., Lammerding, J., Kamm, R.D., Shenoy, V.B., 2016. A chemomechanical model for nuclear morphology and stresses during cell transendothelial migration. *Biophys. J.* 111, 1541–1552.
- Carmeliet, P., Jain, R.K., 2000. Angiogenesis in cancer and other diseases. *Nature* 407, 249–257.

- Chang, P.S., McLane, L.T., Fogg, R., Scrimgeour, J., Temenoff, J.S., Granqvist, A., Curtis, J.E., 2016. Cell surface access is modulated by tethered bottlebrush proteoglycans. *Biophys. J.* 110, 2739–2750.
- Chaudhuri, O., 2017. Viscoelastic hydrogels for 3d cell culture. *Biomater. Sci.* 5, 1480–1490.
- Coffinier, C., Chang, S.Y., Nobumori, C., Tu, Y., Farber, E.A., Toth, J.I., Fong, L.G., Young, S.G., 2010. Abnormal development of the cerebral cortex and cerebellum in the setting of lamin b2 deficiency. *Proc. Natl. Acad. Sci. U.S.A.* 107, 5076–5081.
- Costa, K., Yin, F., 1999. Analysis of indentation: implications for measuring mechanical properties with atomic force microscopy. *J. Biomech. Eng.* 121, 462–471.
- Cross, S.E., Jin, Y.S., Rao, J., Gimzewski, J.K., 2007. Nanomechanical analysis of cells from cancer patients. *Nat. Nanotechnol.* 2, 780–783.
- Dahl, K.N., Engler, A.J., Pajerowski, J.D., Discher, D.E., 2005. Power-law rheology of isolated nuclei with deformation mapping of nuclear substructures. *Biophys. J.* 89, 2855–2864.
- Das, A., Barai, A., Monteiro, M., Kumar, S., Sen, S., 2019. Nuclear softening is essential for protease-independent migration. *Matrix Biol.* .
- Davidson, P.M., Lammerding, J., 2014. Broken nuclei–lamins, nuclear mechanics, and disease. *Trends Cell Biol.* 24, 247–256.
- De, R., Zemel, A., Safran, S.A., 2007. Dynamics of cell orientation. *Nat. Phys.* 3, 655.
- Del Giudice, F., Tassieri, M., Oelschlaeger, C., Shen, A.Q., 2017. When microrheology, bulk rheology, and microfluidics meet: broadband rheology of hydroxyethyl cellulose water solutions. *Macromolecules* 50, 2951–2963.
- Denais, C.M., Gilbert, R.M., Isermann, P., McGregor, A.L., Te Lindert, M., Weigel, B., Davidson, P.M., Friedl, P., Wolf, K., Lammerding, J., 2016. Nuclear envelope rupture and repair during cancer cell migration. *Science* 352, 353–358.
- Desprat, N., Richert, A., Simeon, J., Asnacios, A., 2005. Creep function of a single living cell. *Biophys. J.* 88, 2224–2233.

- Deviri, D., Discher, D.E., Safran, S.A., 2017. Rupture dynamics and chromatin herniation in deformed nuclei. *Biophys. J.* 113, 1060–1071.
- Deviri, D., Pfeifer, C.R., Dooling, L.J., Ivanovska, I.L., Discher, D.E., Safran, S.A., 2019. Scaling laws indicate distinct nucleation mechanisms of holes in the nuclear lamina. *Nat. Phys.* 15, 823–829.
- Dimitriadis, E.K., Horkay, F., Maresca, J., Kachar, B., Chadwick, R.S., 2002. Determination of elastic moduli of thin layers of soft material using the atomic force microscope. *Biophys. J.* 82, 2798–2810.
- Dokukin, M., Ablaeva, Y., Kalaparthy, V., Seluanov, A., Gorbunova, V., Sokolov, I., 2016. Pericellular brush and mechanics of guinea pig fibroblast cells studied with afm. *Biophys. J.* 111, 236–246.
- Elosegui-Artola, A., Andreu, I., Beedle, A.E., Lezamiz, A., Uroz, M., Kosmalska, A.J., Oria, R., Kechagia, J.Z., Rico-Lastres, P., Le Roux, A.L., et al., 2017. Force triggers yap nuclear entry by regulating transport across nuclear pores. *Cell* 171, 1397–1410.
- Esteban-Manzanares, G., González-Bermúdez, B., Cruces, J., De la Fuente, M., Li, Q., Guinea, G.V., Pérez-Rigueiro, J., Elices, M., Plaza, G.R., 2017. Improved measurement of elastic properties of cells by micropipette aspiration and its application to lymphocytes. *Ann. Biomed. Eng.* 45, 1375–1385.
- Evans, A., Whelehan, P., Thomson, K., McLean, D., Brauer, K., Purdie, C., Baker, L., Jordan, L., Rauchhaus, P., Thompson, A., 2012. Invasive breast cancer: relationship between shear-wave elastographic findings and histologic prognostic factors. *Radiology* 263, 673–677.
- Frantz, C., Stewart, K.M., Weaver, V.M., 2010. The extracellular matrix at a glance. *J. Cell Sci.* 123, 4195–4200.
- Friedl, P., Wolf, K., 2010. Plasticity of cell migration: a multiscale tuning model. *J. Cell Biol.* 188, 11–19.
- Fung, Y.C., 1993. *Mechanical properties of living tissues*. volume 547. Springer.
- Gardel, M., Shin, J.H., MacKintosh, F., Mahadevan, L., Matsudaira, P., Weitz, D., 2004a. Elastic behavior of cross-linked and bundled actin networks. *Science* 304, 1301–1305.

- Gardel, M., Shin, J.H., MacKintosh, F., Mahadevan, L., Matsudaira, P., Weitz, D., 2004b. Scaling of f-actin network rheology to probe single filament elasticity and dynamics. *Phys. Rev. Lett.* 93, 188102.
- Gardel, M.L., Kasza, K.E., Brangwynne, C.P., Liu, J., Weitz, D.A., 2008. Mechanical response of cytoskeletal networks. *Method. Cell Biol.* 89, 487–519.
- Gasser, T.C., Ogden, R.W., Holzapfel, G.A., 2006. Hyperelastic modelling of arterial layers with distributed collagen fibre orientations. *J. R. Soc. Interface* 3, 15–35.
- George, E., Barai, A., Shirke, P., Majumder, A., Sen, S., 2018. Engineering interfacial migration by collective tuning of adhesion anisotropy and stiffness. *Acta Biomater.* 72, 82–93.
- Graham, D.M., Andersen, T., Sharek, L., Uzer, G., Rothenberg, K., Hoffman, B.D., Rubin, J., Balland, M., Bear, J.E., Burrige, K., 2018. Enucleated cells reveal differential roles of the nucleus in cell migration, polarity, and mechanotransduction. *J. Cell Biol.* 217, 895–914.
- Guck, J., Schinkinger, S., Lincoln, B., Wottawah, F., Ebert, S., Romeyke, M., Lenz, D., Erickson, H.M., Ananthakrishnan, R., Mitchell, D., et al., 2005. Optical deformability as an inherent cell marker for testing malignant transformation and metastatic competence. *Biophys. J.* 88, 3689–3698.
- Guilak, F., Jones, W.R., Ting-Beall, H.P., Lee, G.M., 1999. The deformation behavior and mechanical properties of chondrocytes in articular cartilage. *Osteoarthr. Cartil.* 7, 59–70.
- Guilak, F., Tedrow, J.R., Burgkart, R., 2000. Viscoelastic properties of the cell nucleus. *Biochem. Biophys. Res. Comm.* 269, 781–786.
- Guo, M., Ehrlicher, A.J., Mahammad, S., Fabich, H., Jensen, M.H., Moore, J.R., Fredberg, J.J., Goldman, R.D., Weitz, D.A., 2013. The role of vimentin intermediate filaments in cortical and cytoplasmic mechanics. *Biophys. J.* 105, 1562–1568.
- Gupta, G.P., Massagué, J., 2006. Cancer metastasis: building a framework. *Cell* 127, 679–695.
- ten Haaf, K., van Rosmalen, J., de Koning, H.J., 2015. Lung cancer detectability by test, histology, stage, and gender: estimates from the nlst and the plco trials. *Cancer Epidemiol. Biomarkers Prev.* 24, 154–161.

- Han, S.K., Madden, R., Abusara, Z., Herzog, W., 2012. In situ chondrocyte viscoelasticity. *J. Biomech.* 45, 2450–2456.
- Handorf, A.M., Zhou, Y., Halanski, M.A., Li, W.J., 2015. Tissue stiffness dictates development, homeostasis, and disease progression. *Organogenesis* 11, 1–15.
- Harada, T., Swift, J., Irianto, J., Shin, J.W., Spinler, K.R., Athirasala, A., Diegmiller, R., Dingal, P.D.P., Ivanovska, I.L., Discher, D.E., 2014. Nuclear lamin stiffness is a barrier to 3d migration, but softness can limit survival. *J. Cell Biol.* 204, 669–682.
- Hatch, E.M., Hetzer, M.W., 2016. Nuclear envelope rupture is induced by actin-based nucleus confinement. *J. Cell Biol.* 215, 27–36.
- Hayes, W., Keer, L.M., Herrmann, G., Mockros, L., 1972. A mathematical analysis for indentation tests of articular cartilage. *J. Biomech.* 5, 541–551.
- Hoffman, B.D., Massiera, G., Van Citters, K.M., Crocker, J.C., 2006. The consensus mechanics of cultured mammalian cells. *Proc. Natl. Acad. Sci. U.S.A.* 103, 10259–10264.
- Holzapfel, G.A., Gasser, T.C., Ogden, R.W., 2000. A new constitutive framework for arterial wall mechanics and a comparative study of material models. *J. Elast.* 61, 1–48.
- Howe, R.D., Peine, W.J., Kantarinis, D., Son, J.S., 1995. Remote palpation technology. *IEEE Eng. Med. Biol.* 14, 318–323.
- Huijbers, I.J., Irvani, M., Popov, S., Robertson, D., Al-Sarraj, S., Jones, C., Isacke, C.M., 2010. A role for fibrillar collagen deposition and the collagen internalization receptor Endo180 in glioma invasion. *PLoS One* 5.
- Hung, W.C., Yang, J.R., Yankaskas, C.L., Wong, B.S., Wu, P.H., Pardo-Pastor, C., Serra, S.A., Chiang, M.J., Gu, Z., Wirtz, D., et al., 2016. Confinement sensing and signal optimization via Piezo1/PKA and myosin II pathways. *Cell Rep.* 15, 1430–1441.
- Irianto, J., Xia, Y., Pfeifer, C.R., Athirasala, A., Ji, J., Alvey, C., Tewari, M., Bennett, R.R., Harding, S.M., Liu, A.J., et al., 2017. Dna damage follows repair factor depletion and portends genome variation in cancer cells after pore migration. *Curr. Biol.* 27, 210–223.

- Iyer, S., Gaikwad, R., Subba-Rao, V., Woodworth, C., Sokolov, I., 2009. Atomic force microscopy detects differences in the surface brush of normal and cancerous cells. *Nat. Nanotechnol.* 4, 389–393.
- Johnson, K.L., Kendall, K., Roberts, a., 1971. Surface energy and the contact of elastic solids. *Proc. R. Soc. A* 324, 301–313.
- Jones, L.M., Gardner, M.J., Catterall, J.B., Turner, G.A., 1995. Hyaluronic acid secreted by mesothelial cells: a natural barrier to ovarian cancer cell adhesion. *Clin. Exp. Metastasis* 13, 373–380.
- Kasza, K.E., Rowat, A.C., Liu, J., Angelini, T.E., Brangwynne, C.P., Koenderink, G.H., Weitz, D.A., 2007. The cell as a material. *Curr. Opin. Cell Biol.* 19, 101–107.
- Kaufmann, A., Heinemann, F., Radmacher, M., Stick, R., 2011. Amphibian oocyte nuclei expressing lamin a with the progeria mutation e145k exhibit an increased elastic modulus. *Nucleus* 2, 310–319.
- Kim, J., Feng, J., Jones, C.A., Mao, X., Sander, L.M., Levine, H., Sun, B., 2017. Stress-induced plasticity of dynamic collagen networks. *Nat. Commun.* 8, 842.
- Kimata, K., Honma, Y., Okayama, M., Oguri, K., Hozumi, M., Suzuki, S., 1983. Increased synthesis of hyaluronic acid by mouse mammary carcinoma cell variants with high metastatic potential. *Cancer Res.* 43, 1347–1354.
- Kirby, T.J., Lammerding, J., 2018. Emerging views of the nucleus as a cellular mechanosensor. *Nat. Cell Biol.* 20, 373–381.
- Konstantinova, J., Cotugno, G., Dasgupta, P., Althoefer, K., Nanayakkara, T., 2017. Palpation force modulation strategies to identify hard regions in soft tissue organs. *PloS One* 12.
- Konstantinova, J., Li, M., Aminzadeh, V., Althoefer, K., Dasgupta, P., et al., 2013. Evaluating manual palpation trajectory patterns in tele-manipulation for soft tissue examination, in: *Conf Proc IEEE Int Conf Syst Man Cybern, IEEE.* pp. 4190–4195.
- Krause, M., Wei Yang, F., Lindert, M.t., Isermann, P., Schepens, J., Maas, R.J., Eid, K., Venkataraman, C., Lammerding, J., Madzvamuse, A., et al., 2019. Cell migration through 3d

- confining pores: speed accelerations by deformation and recoil of the nucleus. *Philos. Trans. R. Soc. B* .
- Kumar, S., Das, A., Barai, A., Sen, S., 2018a. MMP secretion rate and inter-invadopodia spacing collectively govern cancer invasiveness. *Biophys. J.* 114, 650–662.
- Kumar, S., Das, A., Sen, S., 2018b. Multicompartment cell-based modeling of confined migration: regulation by cell intrinsic and extrinsic factors. *Mol. Biol. Cell* 29, 1599–1610.
- Kumar, S., Kapoor, A., Desai, S., Inamdar, M.M., Sen, S., 2016. Proteolytic and non-proteolytic regulation of collective cell invasion: tuning by ECM density and organization. *Sci. Rep.* 6, 19905.
- Kuo, J.C.H., Gandhi, J.G., Zia, R.N., Paszek, M.J., 2018. Physical biology of the cancer cell glycocalyx. *Nat. Phys.* 14, 658–669.
- Lammerding, J., Fong, L.G., Ji, J.Y., Reue, K., Stewart, C.L., Young, S.G., Lee, R.T., 2006. Lamins a and c but not lamin b1 regulate nuclear mechanics. *J. Biol. Chem.* 281, 25768–25780.
- Lange, J.R., Steinwachs, J., Kolb, T., Lautscham, L.A., Harder, I., Whyte, G., Fabry, B., 2015. Microconstriction arrays for high-throughput quantitative measurements of cell mechanical properties. *Biophys. J.* 109, 26–34.
- Lautscham, L.A., Kämmerer, C., Lange, J.R., Kolb, T., Mark, C., Schilling, A., Strissel, P.L., Strick, R., Gluth, C., Rowat, A.C., et al., 2015. Migration in confined 3d environments is determined by a combination of adhesiveness, nuclear volume, contractility, and cell stiffness. *Biophys. J.* 109, 900–913.
- Lavenus, S.B., Tudor, S.M., Ullo, M.F., Vosatka, K.W., Logue, J.S., 2020. A flexible network of vimentin intermediate filaments promotes the migration of amoeboid cancer cells through confined environments. *J. Biol. Chem.* , jbc-RA119.
- Le Berre, M., Aubertin, J., Piel, M., 2012. Fine control of nuclear confinement identifies a threshold deformation leading to lamina rupture and induction of specific genes. *Integr. Biol.* 4, 1406–1414.

- Lebedev, N., Ufliand, I.S., 1958. Axisymmetric contact problem for an elastic layer. *PMM J. Appl. Math. Mech.* 22, 442–450.
- Leong, H.S., Robertson, A.E., Stoletov, K., Leith, S.J., Chin, C.A., Chien, A.E., Hague, M.N., Ablack, A., Carmine-Simmen, K., McPherson, V.A., et al., 2014. Invadopodia are required for cancer cell extravasation and are a therapeutic target for metastasis. *Cell Rep.* 8, 1558–1570.
- Levental, K.R., Yu, H., Kass, L., Lakins, J.N., Egeblad, M., Erler, J.T., Fong, S.F., Csiszar, K., Giaccia, A., Wenginger, W., et al., 2009. Matrix crosslinking forces tumor progression by enhancing integrin signaling. *Cell* 139, 891–906.
- Licup, A.J., Münster, S., Sharma, A., Sheinman, M., Jawerth, L.M., Fabry, B., Weitz, D.A., MacKintosh, F.C., 2015. Stress controls the mechanics of collagen networks. *Proc. Natl. Acad. Sci. U.S.A.* 112, 9573–9578.
- Liu, D., Zhang, Z., Sun, L., 2010. Nonlinear elastic load–displacement relation for spherical indentation on rubberlike materials. *J. Mater. Res.* 25, 2197–2202.
- Liu, W.K., Liu, Y., Farrell, D., Zhang, L., Wang, X.S., Fukui, Y., Patankar, N., Zhang, Y., Bajaj, C., Lee, J., et al., 2006. Immersed finite element method and its applications to biological systems. *Comput. Methods Appl. Mech. Eng.* 195, 1722–1749.
- Liu, Y., Kerdok, A.E., Howe, R.D., 2004. A nonlinear finite element model of soft tissue indentation, in: *International Symposium on Medical Simulation*, Springer. pp. 67–76.
- Low, T.F., Pun, C.L., Yan, W., 2015. Theoretical study on nanoindentation hardness measurement of a particle embedded in a matrix. *Philos. Mag.* 95, 1573–1586.
- Lu, P., Weaver, V.M., Werb, Z., 2012. The extracellular matrix: a dynamic niche in cancer progression. *J. Cell Biol.* 196, 395–406.
- Ludwik, P., 1909. Elements of technological mechanics, in: *Elements of Technological Mechanics*. Springer, pp. 11–35.
- Maurer, M., Lammerding, J., 2019. The driving force: Nuclear mechanotransduction in cellular function, fate, and disease. *Annu. Rev. Biomed. Eng.* 21.

- McGregor, A.L., Hsia, C.R., Lammerding, J., 2016. Squish and squeeze—the nucleus as a physical barrier during migration in confined environments. *Curr. Opin. Cell Biol.* 40, 32–40.
- Mietke, A., Otto, O., Girardo, S., Rosendahl, P., Taubenberger, A., Golfier, S., Ulbricht, E., Aland, S., Guck, J., Fischer-Friedrich, E., 2015. Extracting cell stiffness from real-time deformability cytometry: theory and experiment. *Biophys. J.* 109, 2023–2036.
- Mistriotis, P., Wisniewski, E.O., Bera, K., Keys, J., Li, Y., Tuntithavornwat, S., Law, R.A., Perez-Gonzalez, N.A., Erdogmus, E., Zhang, Y., et al., 2019. Confinement hinders motility by inducing rhoa-mediated nuclear influx, volume expansion, and blebbing. *J. Cell Biol.* 218, 4093–4111.
- Moeendarbary, E., Valon, L., Fritzsche, M., Harris, A.R., Moulding, D.A., Thrasher, A.J., Stride, E., Mahadevan, L., Charras, G.T., 2013. The cytoplasm of living cells behaves as a poroelastic material. *Nat. Mater.* 12, 253.
- Moure, A., Gomez, H., 2017. Phase-field model of cellular migration: Three-dimensional simulations in fibrous networks. *Comput. Methods Appl. Mech. Eng.* 320, 162–197.
- Murphy, M.C., Jones, D.T., Jack Jr, C.R., Glaser, K.J., Senjem, M.L., Manduca, A., Felmlee, J.P., Carter, R.E., Ehman, R.L., Huston III, J., 2016. Regional brain stiffness changes across the Alzheimer’s disease spectrum. *NeuroImage Clin.* 10, 283–290.
- Navarro, A.P., Collins, M.A., Folker, E.S., 2016. The nucleus is a conserved mechanosensation and mechanoresponse organelle. *Cytoskeleton* 73, 59–67.
- Neelam, S., Chancellor, T., Li, Y., Nickerson, J.A., Roux, K.J., Dickinson, R.B., Lele, T.P., 2015. Direct force probe reveals the mechanics of nuclear homeostasis in the mammalian cell. *Proc. Natl. Acad. Sci. U.S.A.* 112, 5720–5725.
- NIH, 2018. Cancer statistics. <https://www.cancer.gov/about-cancer/understanding/statistics>.
- Pajerowski, J.D., Dahl, K.N., Zhong, F.L., Sammak, P.J., Discher, D.E., 2007. Physical plasticity of the nucleus in stem cell differentiation. *Proc. Natl. Acad. Sci. U.S.A.* 104, 15619–15624.

- Paluch, E.K., Aspalter, I.M., Sixt, M., 2016. Focal adhesion-independent cell migration. *Annu. Rev. Cell Dev. Biol.* 32, 469–490.
- Pan, Y., Zhan, Y., Ji, H., Niu, X., Zhong, Z., 2016. Can hyperelastic material parameters be uniquely determined from indentation experiments? *RSC Adv.* 6, 81958–81964.
- Pang, X.D., Tan, H.Z., Durlach, N.I., 1991. Manual discrimination of force using active finger motion. *Percept. Psychophys.* 49, 531–540.
- Paszek, M.J., DuFort, C.C., Rossier, O., Bainer, R., Mouw, J.K., Godula, K., Hudak, J.E., Lakins, J.N., Wijekoon, A.C., Cassereau, L., et al., 2014. The cancer glycocalyx mechanically primes integrin-mediated growth and survival. *Nature* 511, 319–325.
- Patteson, A.E., Vahabikashi, A., Pogoda, K., Adam, S.A., Mandal, K., Kittisopikul, M., Sivagurunathan, S., Goldman, A., Goldman, R.D., Janmey, P.A., 2019. Vimentin protects cells against nuclear rupture and dna damage during migration. *J. Cell Biol.* 218, 4079–4092.
- Paul, C.D., Mistriotis, P., Konstantopoulos, K., 2017. Cancer cell motility: lessons from migration in confined spaces. *Nat. Rev. Cancer* 17, 131.
- Peña, E., Alastrué, V., Laborda, A., Martínez, M., Doblaré, M., 2010. A constitutive formulation of vascular tissue mechanics including viscoelasticity and softening behaviour. *J. Biomech.* 43, 984–989.
- Peterson, L.J., Rajfur, Z., Maddox, A.S., Freel, C.D., Chen, Y., Edlund, M., Otey, C., Burridge, K., 2004. Simultaneous stretching and contraction of stress fibers in vivo. *Mol. Biol. Cell* 15, 3497–3508.
- Petrie, R.J., Koo, H., Yamada, K.M., 2014. Generation of compartmentalized pressure by a nuclear piston governs cell motility in a 3d matrix. *Science* 345, 1062–1065.
- Raab, M., Gentili, M., de Belly, H., Thiam, H.R., Vargas, P., Jimenez, A.J., Lautenschlaeger, F., Voituriez, R., Lennon-Duménil, A.M., Manel, N., et al., 2016. ESCRT III repairs nuclear envelope ruptures during cell migration to limit DNA damage and cell death. *Science* 352, 359–362.
- Rabodzey, A., Alcaide, P., Luscinskas, F.W., Ladoux, B., 2008. Mechanical forces induced by the transendothelial migration of human neutrophils. *Biophys. J.* 95, 1428–1438.

- Rape, A.D., Kumar, S., 2014. A composite hydrogel platform for the dissection of tumor cell migration at tissue interfaces. *Biomaterials* 35, 8846–8853.
- Renkawitz, J., Kopf, A., Stopp, J., de Vries, I., Driscoll, M.K., Merrin, J., Hauschild, R., Welf, E.S., Danuser, G., Fiolka, R., et al., 2019. Nuclear positioning facilitates amoeboid migration along the path of least resistance. *Nature* 568, 546.
- Reversat, A., Gaertner, F., Merrin, J., Stopp, J., Tasciyan, S., Aguilera, J., de Vries, I., Hauschild, R., Hons, M., Piel, M., et al., 2020. Cellular locomotion using environmental topography. *Nature* , 1–4.
- Roux, K.J., Crisp, M.L., Liu, Q., Kim, D., Kozlov, S., Stewart, C.L., Burke, B., 2009. Nesprin 4 is an outer nuclear membrane protein that can induce kinesin-mediated cell polarization. *Proc. Natl. Acad. Sci. U.S.A.* 106, 2194–2199.
- Rowat, A.C., Jaalouk, D.E., Zwerger, M., Ung, W.L., Eydelnant, I.A., Olins, D.E., Olins, A.L., Herrmann, H., Weitz, D.A., Lammerding, J., 2013. Nuclear envelope composition determines the ability of neutrophil-type cells to passage through micron-scale constrictions. *J. Biol. Chem.* 288, 8610–8618.
- Rozario, T., DeSimone, D.W., 2010. The extracellular matrix in development and morphogenesis: a dynamic view. *Dev. Biol.* 341, 126–140.
- Samani, A., Zubovits, J., Plewes, D., 2007. Elastic moduli of normal and pathological human breast tissues: an inversion-technique-based investigation of 169 samples. *Phys. Med. Biol.* 52, 1565.
- Samuel, M.S., Lopez, J.I., McGhee, E.J., Croft, D.R., Strachan, D., Timpson, P., Munro, J., Schröder, E., Zhou, J., Brunton, V.G., et al., 2011. Actomyosin-mediated cellular tension drives increased tissue stiffness and β -catenin activation to induce epidermal hyperplasia and tumor growth. *Cancer Cell* 19, 776–791.
- Sangpradit, K., Liu, H., Seneviratne, L.D., Althoefer, K., 2009. Tissue identification using inverse finite element analysis of rolling indentation, in: *IEEE Int. Conf. Robot. Autom.*, IEEE. pp. 1250–1255.

- Sanz-Moreno, V., Gadea, G., Ahn, J., Paterson, H., Marra, P., Pinner, S., Sahai, E., Marshall, C.J., 2008. Rac activation and inactivation control plasticity of tumor cell movement. *Cell* 135, 510–523.
- Sapir, L., Tzliil, S., 2017. Talking over the extracellular matrix: How do cells communicate mechanically?, in: *Semin. Cell Dev. Biol.*, Elsevier. pp. 99–105.
- Schmidt, S., Friedl, P., 2010. Interstitial cell migration: integrin-dependent and alternative adhesion mechanisms. *Cell Tissue Res.* 339, 83.
- Sen, S., Subramanian, S., Discher, D.E., 2005. Indentation and adhesive probing of a cell membrane with afm: theoretical model and experiments. *Biophys. J.* 89, 3203–3213.
- Shurer, C.R., Kuo, J.C.H., Roberts, L.M., Gandhi, J.G., Colville, M.J., Enoki, T.A., Pan, H., Su, J., Noble, J.M., Hollander, M.J., et al., 2019. Physical principles of membrane shape regulation by the glycocalyx. *Cell* .
- Skovoroda, A., Klishko, A., Gusakyan, D., Mayevskii, Y.I., Yermilova, V., Oran-skaya, G., Sarvazyan, A., 1995. Quantitative analysis of the mechanical characteristics of pathologically changed soft biological tissues. *Biophysics* 40, 1359–1364.
- Smith, L.A., Aranda-Espinoza, H., Haun, J.B., Dembo, M., Hammer, D.A., 2007. Neutrophil traction stresses are concentrated in the uropod during migration. *Biophys. J.* 92, L58–L60.
- Sneddon, I.N., 1965. The relation between load and penetration in the axisymmetric boussinesq problem for a punch of arbitrary profile. *Int. J. Eng. Sci.* 3, 47–57.
- Sokolov, I., Dokukin, M.E., Guz, N.V., 2013. Method for quantitative measurements of the elastic modulus of biological cells in afm indentation experiments. *Methods* 60, 202–213.
- Stephens, A.D., Banigan, E.J., Adam, S.A., Goldman, R.D., Marko, J.F., 2017. Chromatin and lamin a determine two different mechanical response regimes of the cell nucleus. *Mol. Biol. Cell* 28, 1984–1996.
- Stephens, A.D., Banigan, E.J., Marko, J.F., 2019. Chromatin’s physical properties shape the nucleus and its functions. *Curr. Opin. Cell Biol.* 58, 76–84.
- Stricker, J., Falzone, T., Gardel, M.L., 2010. Mechanics of the f-actin cytoskeleton. *J. Biomech.* 43, 9–14.

- Stroka, K.M., Jiang, H., Chen, S.H., Tong, Z., Wirtz, D., Sun, S.X., Konstantopoulos, K., 2014. Water permeation drives tumor cell migration in confined microenvironments. *Cell* 157, 611–623.
- Suresh, S., 2007. Biomechanics and biophysics of cancer cells. *Acta Biomater.* 3, 413–438.
- Suresh, S., Spatz, J., Mills, J.P., Micoulet, A., Dao, M., Lim, C., Beil, M., Seufferlein, T., 2005. Connections between single-cell biomechanics and human disease states: gastrointestinal cancer and malaria. *Acta Biomater.* 1, 15–30.
- Swartz, R.K., Rodriguez, E.C., King, M.C., 2014. A role for nuclear envelope–bridging complexes in homology-directed repair. *Mol. Biol. Cell* 25, 2461–2471.
- Swift, J., Ivanovska, I.L., Buxboim, A., Harada, T., Dingal, P.D.P., Pinter, J., Pajerowski, J.D., Spinler, K.R., Shin, J.W., Tewari, M., et al., 2013. Nuclear lamin-a scales with tissue stiffness and enhances matrix-directed differentiation. *Science* 341, 1240104.
- Tajik, A., Zhang, Y., Wei, F., Sun, J., Jia, Q., Zhou, W., Singh, R., Khanna, N., Belmont, A.S., Wang, N., 2016. Transcription upregulation via force-induced direct stretching of chromatin. *Nat. Mater.* 15, 1287.
- Talmadge, J.E., Fidler, I.J., 2010. AACR Centennial Series: The biology of cancer metastasis: historical perspective. *Cancer Res.* 70, 5649–5669.
- Theret, D.P., Levesque, M., Sato, M., Nerem, R., Wheeler, L., 1988. The application of a homogeneous half-space model in the analysis of endothelial cell micropipette measurements. *J. Biomech. Eng.* , 110:190–199.
- Thiam, H.R., Vargas, P., Carpi, N., Crespo, C.L., Raab, M., Terriac, E., King, M.C., Jacobelli, J., Alberts, A.S., Stradal, T., et al., 2016. Perinuclear arp2/3-driven actin polymerization enables nuclear deformation to facilitate cell migration through complex environments. *Nat. Commun.* 7, 10997.
- Timoshenko, S.P., Woinowsky-Krieger, S., 1959. *Theory of Plates and Shells*. McGraw-Hill.
- Tocco, V.J., Li, Y., Christopher, K.G., Matthews, J.H., Aggarwal, V., Paschall, L., Luesch, H., Licht, J.D., Dickinson, R.B., Lele, T.P., 2018. The nucleus is irreversibly shaped by motion of cell boundaries in cancer and non-cancer cells. *J. Cell. Physiol.* 233, 1446–1454.

- Trickey, W.R., Vail, T.P., Guilak, F., 2004. The role of the cytoskeleton in the viscoelastic properties of human articular chondrocytes. *J. Orthop. Res.* 22, 131–139.
- Turley, E.A., Wood, D.K., McCarthy, J.B., 2016. Carcinoma cell hyaluronan as a “portable” cancerized prometastatic microenvironment. *Cancer Res.* 76, 2507–2512.
- Valero, C., Navarro, B., Navajas, D., García-Aznar, J., 2016. Finite element simulation for the mechanical characterization of soft biological materials by atomic force microscopy. *J. Mech. Behav. Biomed.* 62, 222–235.
- Verstraeten, V.L., Ji, J.Y., Cummings, K.S., Lee, R.T., Lammerding, J., 2008. Increased mechanosensitivity and nuclear stiffness in hutchinson–gilford progeria cells: effects of farnesyltransferase inhibitors. *Aging Cell* 7, 383–393.
- WHO, 2018. Cancer. <https://www.who.int/news-room/fact-sheets/detail/cancer>.
- Wisdom, K.M., Adebowale, K., Chang, J., Lee, J.Y., Nam, S., Desai, R., Rossen, N.S., Rafat, M., West, R.B., Hodgson, L., et al., 2018. Matrix mechanical plasticity regulates cancer cell migration through confining microenvironments. *Nat. Commun.* 9, 4144.
- Wolf, K., Mazo, I., Leung, H., Engelke, K., Von Andrian, U.H., Deryugina, E.I., Strongin, A.Y., Bröcker, E.B., Friedl, P., 2003. Compensation mechanism in tumor cell migration: mesenchymal–amoeboid transition after blocking of pericellular proteolysis. *J. Cell Biol.* 160, 267–277.
- Wolf, K., Te Lindert, M., Krause, M., Alexander, S., Te Riet, J., Willis, A.L., Hoffman, R.M., Figdor, C.G., Weiss, S.J., Friedl, P., 2013. Physical limits of cell migration: control by ECM space and nuclear deformation and tuning by proteolysis and traction force. *J. Cell Biol.* 201, 1069–1084.
- Xia, Y., Pfeifer, C.R., Zhu, K., Irianto, J., Liu, D., Pannell, K., Chen, E.J., Dooling, L.J., Tobin, M.P., Wang, M., et al., 2019. Rescue of dna damage after constricted migration reveals a mechano-regulated threshold for cell cycle. *J. Cell Biol.* , 201811100.
- Yamada, K.M., Sixt, M., 2019. Mechanisms of 3d cell migration. *Nat. Rev. Mol. Cell Biol.* 20, 738–752.

- Yan, W., Sun, Q., Feng, X.Q., Qian, L., 2006. Determination of transformation stresses of shape memory alloy thin films: a method based on spherical indentation. *Appl. Phys. Lett.* 88, 241912.
- Yeung, T., Georges, P.C., Flanagan, L.A., Marg, B., Ortiz, M., Funaki, M., Zahir, N., Ming, W., Weaver, V., Janmey, P.A., 2005. Effects of substrate stiffness on cell morphology, cytoskeletal structure, and adhesion. *Cell Motil. Cytoskel.* 60, 24–34.
- Zemel, A., Rehfeldt, F., Brown, A., Discher, D., Safran, S., 2010. Optimal matrix rigidity for stress-fibre polarization in stem cells. *Nat. Phys.* 6, 468.
- Zhang, L., Underhill, C.B., Chen, L., 1995. Hyaluronan on the surface of tumor cells is correlated with metastatic behavior. *Cancer Res.* 55, 428–433.
- Zhang, M.G., Cao, Y.P., Li, G.Y., Feng, X.Q., 2014. Spherical indentation method for determining the constitutive parameters of hyperelastic soft materials. *Biomech. Model. Mechanobiol.* 13, 1–11.
- Zhang, Q., Tamashunas, A.C., Agrawal, A., Torbati, M., Katiyar, A., Dickinson, R.B., Lammerding, J., Lele, T.P., 2019. Local, transient tensile stress on the nuclear membrane causes membrane rupture. *Mol. Biol. Cell* 30, 899–906.
- Zhou, E., Lim, C., Quek, S., 2005. Finite element simulation of the micropipette aspiration of a living cell undergoing large viscoelastic deformation. *Mech. Adv. Mater. Struc.* 12, 501–512.
- Zhu, J., Mogilner, A., 2016. Comparison of cell migration mechanical strategies in three-dimensional matrices: a computational study. *Interface Focus* 6, 20160040.